Design and Optimization of Grid-connected Solar Powered Electric Vehicle Charging Station

(Case Study of Adama City)

Mesgana Tulu Hasseno

A Thesis Submitted to

The Department of Electrical Power and Control Engineering

School of Electrical Engineering and Computing

Presented in Partial Fulfillment of the Requirement for the Master of Science Degree in Electrical Power and Control Engineering

(Power System Engineering)

Office of Graduate Studies
Adama Science and Technology University

July, 2023

Adama, Ethiopia

Design and Optimization of Grid-connected Solar Powered Electric Vehicle Charging Station

(Case Study of Adama city)

Mesgana Tulu Hasseno

Advisor: Dr. Milkias Berhanu

A Thesis Submitted to

The Department of Electrical Power and Control Engineering

School of Electrical Engineering and Computing

Presented in Partial Fulfillment of the Requirement for the Master of Science Degree in Electrical Power and Control Engineering

(Power System Engineering)

Office of Graduate Studies

Adama Science and Technology University

July, 2023

Adama, Ethiopia

DECLARATION

I hereby declare that this Master Thesis entitled **"*Design and Optimization of Grid-connected Solar Powered Electric Vehicle Charging Station (Case Study of Adama city*)"** is my original work. That is, it has not been submitted for the award of any academic degree, diploma or certificate in any other university. All sources of materials that are used for this thesis have been duly acknowledged through citation.

Mesgana Tulu Hasseno	____________________	____________________
Name of Student	Signature	Date

RECOMMENDATION

I, the advisor of this thesis, hereby certify that I have read the revised version of the thesis entitled **“*Design and Optimization of Grid-connected Solar Powered Electric Vehicle Charging Station (Case Study of Adama city)*”** prepared under my guidance by Mesgana Tulu Hasseno submitted in partial fulfillment of the requirements for the degree of Masters of Science in Electrical Power and Control Engineering, postgraduate power system engineering. Therefore, I recommend the submission of revised version of the thesis to the department following the applicable procedures.

Dr. Milkias Berhanu	________________	________________
Advisor	Signature	Date

APPROVAL PAGE

I the advisor of thesis entitled "***Design and Optimization of Grid-connected Solar Powered Electric Vehicle Charging Station (Case Study of Adama city)***" and developed by Mesgana Tulu Hasseno, hereby certify that the recommendation and suggestions made by the board of examiners are appropriately incorporated into the final version of the thesis.

Dr. Milkias Berhanu	_______________	_____________
Advisor	Signature	Date

We, the undersigned, members of the Board of Examiners of the thesis by Mesgana Tulu Hasseno have read and evaluated the thesis entitled "***Design and Optimization of Grid-connected Solar Powered Electric Vehicle Charging Station (Case Study of Adama city)***" and examined the candidate during open defense. This is, therefore, to certify that the thesis is accepted for partial fulfillment of the requirement of the degree of Master of Science in power system engineering.

_________________	________________	_______________
Chairperson	Signature	Date
_________________	________________	_______________
Internal Examiner	Signature	Date
_________________	________________	_______________
External Examiner	Signature	Date

Final approval and acceptance of the thesis is contingent upon submission of its final copy to the Office of Postgraduate Studies (OPGS) through the Department Graduate Council (DGC) and School Graduate Committee (SGC).

_____________________________	________________	_______________
Department Head	Signature	Date
_____________________________	________________	_______________
School Dean	Signature	Date
______________________	________________	________________
Office of Postgraduate Studies, Dean	Signature	Date

ACKNOWLEDGEMENTS

First and foremost, I would like to take this opportunity to give glory to Medhanialem and to Kidanemihiret, with whom the completion of this work would have been impossible.

I express my gratitude to Dr. Milkias Berhanu, my thesis advisor. Throughout my research and writing process, Dr. Milkias Berhanu's office was always accessible whenever I encountered difficulties or had inquiries. His valuable input and insightful discussions covered a wide range of topics, and he consistently encouraged me to take ownership of this paper. Additionally, he provided guidance whenever he felt it was necessary, steering me in the right direction.

Lastly, I would like to sincerely acknowledge and appreciate my family as well as my friends (Woinshet Lera, Tenaye Areda, Tewachew Alem, and Abnet Eshetu) for their unwavering support and constant encouragement during my academic journey and the entire process of researching and writing this thesis. Their presence and assistance have been instrumental in the realization of this achievement, and I am truly grateful for their contributions. I would like to express my gratitude to Tsion Tigistu for her invaluable guidance in editing this document. Thank you deeply for everything.

DEDICATION

To my dearest mothers ***(Kbnesh Beyene and Kelemua Amare),***

You have been my biggest supporter throughout this entire journey. Your unwavering love, sacrifices, and endless encouragement have shaped me into the person I am today.

This thesis is dedicated to you, my incredible mothers. Your presence in my life has been a gift beyond measure. It is through your love and support that I have found the strength to overcome obstacles.

Thank you for being my source of inspiration. I am forever grateful for your love and guidance.

TABLE OF CONTENTS

LIST OF TABLES

LIST OF FIGURES

ACRONYMS

AC	Alternating Current
BDDC	Bidirectional DC-DC Converter
BEV	Battery Electric Vehicles
CAN	Controller Area Network
CCS/COMBO	Combined Charging System, Combo
CHAdeMO	CHArge de MOve
CO_2	Carbon dioxide
DC	Direct Current
CCM	Continuous Conduction Mode
DCFC	Direct Current Fast Charging
DCM	Discontinuous Conduction Mode
EMI	Electromagnetic Interference
ESS	Energy Storage System
ETB	Ethiopian Birr
EV	Electric Vehicles
Fr	Resonant Frequency
Fs	Switching Frequency
FCEV	Fuel Cell Electric Vehicles
FCS	Fast Charging Station
GHG	Green House Gas
HEV	Hybrid Electric Vehicles
HOMER	Hybrid Optimization Model for Electric Renewable
ICE	Internal Combustion Engine
IEC	International Electrotechnical Commission

IGBT	Insulated Gate Bipolar Transistor
Km	Kilometer
kW	Kilowatt
LCOE	Levelized Cost of Energy
Mi	Mile
MOSFET	Metal Oxide Semiconductor Field Effect Transistor
MPP	Maximum Power Point
Ms	Millisecond
N	Turn Ratio
NPC	Net Present Cost
PID	Proportional Integral Derivative
PLL	Phase Locked Loop
PWM	Pulse Width Modulation
PV	Photovoltaic
RES	Renewable Energy Sources
SAE	Society of Automotive Engineering
SAC	Standards Administration of China
SNNPR	South Nation Nationalities and People Region
SOC	State of Charge
THD	Total Harmonic Distortion
UDDBC	Unidirectional DC-DC Boost Converter
V2G	Vehicle to Grid
ZVS	Zero Voltage Switching

ABSTRACT

The rapid spread of electric vehicles (EVs) is a major step forward in addressing the ever-increasing greenhouse gas emissions around the world. Grid-connected charging of electric vehicles based on renewable energy is recognized as one of the most suitable solutions for minimizing both oil consumption and greenhouse effect. Faster recharging using a public fast charging station (FCS) provides a quick charge for a shorter trip and alleviates the range anxiety for long-distance trips. Such "on-the-go" fast charging will eventually be as easy and convenient as refueling a gasoline vehicle. However, one of the biggest challenges facing EV owners is access to convenient charging infrastructure. This thesis proposes a method to design a grid-connected solar-powered fast charging station for electric vehicles. Taking the recorded minimum sunshine hour of 4.7 h/day, the hybrid system was designed and evaluated using HOMER and MATLAB Simulink software. The optimization process determines the best power generation system for the selected location. This allows electric vehicle loads to be powered despite radiation fluctuations. The selected system includes grid system, solar power, batteries and converters, resulting in a cost of energy (COE) of $0.09839/kWh and a total net present cost (NPC) of $264,737.4. The system has a payback period of 5 years. The charging station rectification stage uses voltage-oriented regulation to correct the power factor and minimize the total harmonic distortion of the system. In this thesis, a 50kW charger is designed for charging batteries with an output voltage of 200 V to 450 V and near to unity power factor.

Key words: Electric Vehicle, Fast Charging, Grid-Connected System, Optimization, Solar

CHAPTER ONE

1 INTRODUCTION

1.1 Background

Electric vehicles (EV) have been getting popularity globally. Ethiopia is one of the countries which currently exempts electric vehicles imported or locally assembled from value added tax, surtax and excise tax. This encourages the regular citizens to buy electric vehicles with affordable price. In the future transport and logistic minster of Ethiopia development plan, the ministry directs to import 148 thousand of electric automobiles and 4,800 electric buses within 10 years (EBC, 2022).

A better and more suitable substitute for a fuel-powered vehicle is an electric one. Several research initiatives relating to the development of alternative energy in the transport and power generation sectors will be carried out in the near future in an effort to reduce oil consumption. One such amazing option that helps reduce carbon emissions while also eliminating the need for oil is the use of electric vehicles (EVs). One of the feasible solutions to problems like climate change, energy reliability, and security will be the electrification of the transportation sector (N.R., 2017).

Rapid EV adoption is significantly reducing the world's ongoing rise in GHG emissions. But along with this significant advancement also come great difficulties. As the number of EVs increases, so does the need for charging infrastructure, which will increase electricity demand significantly.

Moreover, it is anticipated that the integration of these newly introduced nonlinear loads and high-frequency switching converters, along with the connection to the grid, will lead to power quality issues. Consequently, there is a growing need for diverse EV charging stations that utilize renewable energy sources (Alkahtani, et al., 2020). Presently, the existing EV charging stations in Ethiopia rely on electric power supplied by the utility grid.

As the number of electric vehicles (EVs) on the road increases, charging these vehicles using the electric grid power becomes challenging. The growing influx of EVs being connected to the grid unavoidably leads to significant impacts on its overall functionality and control. Hence, there is a requirement for an effective charging system for electric vehicles (EVs) that makes use of renewable energy sources. While solar energy is environmentally friendly and sustainable, the unreliable energy obtained from the Photo voltaic (PV) system and the varying charging requirements of individual EVs present challenges when it comes to efficiently charging vehicles from these sources (Biya & Sindhu, 2019).

Incorporating energy storage, such as backup batteries, into the power grid proved to be the most convenient approach in mitigating the issues of intermittency, unpredictability, and power fluctuations. This integration ensures a reliable and uninterrupted supply of renewable electricity, offering stability to the grid (Alkahtani, et al., 2020).

1.2 Study Area and Demographics

The Central Oromia Region of Ethiopia is used as the study location for this thesis proposal. A 99-kilometre (62-mile) drive from Addis Abeba, the country's capital, you will find Adama in the East Shewa Zone. The Great Rift Valley is to the east, while the city is situated at the base of an escarpment to the west. Adama is a crowded transport center. The city is located alongside the highway that runs from Addis Abeba to Dire Dawa. For transportation to and from Djibouti's seaports, numerous trucks travel this same route (contributors, 2022).

Figure 1.1: Location of the site (Adama city, Ethiopia)

1.2.1 Site Selection

Specific site location is an important factor for the selection of charging station installation. A good location can increase both the demand for charging stations and customer satisfaction. Crucial points that need to be considered for the installation site would be: (Orhan & Celal, 2021).

- Stations need to be easily reachable,
- Station should be outer parts or outside the city for the aim of maximizing utilization solar energy,
- Station should be faced to the south to handle maximum solar power,
- Solar energy potential of the site should be feasible.

Based on the above four points Addis Ababa-Adama Expressway road area, located to the west direction from the town is selected for the charging station as there exist high and continuous vehicles flow also has a feasible solar potential. The site is easily reachable with a wide solar panel installation area.

Figure 1.2: Geographical location of the selected area

Demographics

Location: 08°31.6′N 39°15.5′E

Elevation: 1,712 m (5,617 ft)

1.3 Statement of the Problem

Electric vehicles (EVs) are currently popular due to their low carbon emission and reduced fuel cost. Ethiopia invests about $1.07 million annually for fuel consumption in the transport sector of Adama city. To reduce this economical expense the solution is the use of electric vehicles. Besides, the existing most vehicles in Ethiopia are fuel based, which contributes suffrage in foreign currency and climate change crisis as well. So, now the government of Ethiopia is highly encouraged to import and locally assemble electric vehicles.

Fast charging using public fast charging stations (FCS) enables fast charging for short trips in densely populated areas and reduces range concerns for long trips. Such “on-the-go” fast charging will eventually become as easy and convenient as refueling a patrol car. However, one of the biggest challenges for electric vehicle owners is accessing a suitable charging infrastructure. The result is often limited performance and slow load times. The current charging infrastructure in Adama, Ethiopia is limited, and there is a lack of accessible DCFC (direct current fast charging) infrastructure for electric vehicles. Electric vehicle on-board chargers are typically designed to fit inside a vehicle and have size and weight limitations. This is a major obstruction to the adoption of electric vehicles in Ethiopia. In addition, the existing charging infrastructure relies heavily on the power grid, which is often unreliable due to interruptions.

There is a need to develop and optimize grid-connected solar-powered off-board EV charging stations that can provide a viable EV charging infrastructure for Ethiopia. Charging stations should be designed to maximize energy efficiency, minimize costs and reduce demand on the grid by integrating renewable energy sources. Charging stations should be accessible to the general public. Solving this problem will promote clean energy use in Ethiopia, reduce its carbon footprint, and provide better electric vehicle charging infrastructure. The main aim of this study is to reduce greenhouse effect and utility bills.

1.4 Objectives

1.4.1 General Objective

The general objective of this thesis is to design and optimize Grid-connected solar powered electric vehicle charging station at Adama, Ethiopia.

1.4.2 Specific Objectives

The specific objectives of the study are as follows:

- To select the appropriate power level for the Charging Station.
- To determine the optimal solar panel and charging system size and capacity
- To model and simulate the electric vehicle charging system with an appropriate circuit using MATLAB Simulink.
- To determine the optimization and cost-effectiveness of charging Station using HOMER Software.

1.5 Scope and Limitation of the Study

This thesis mathematically designs a solar PV system component including PV modules with MPPT, and converter. Sizing of the system components is started from the estimation of energy demand of electric vehicles (EV) per hour. Solar photovoltaic (PV) energy system with grid integration is simulated.

This study is limited to the simulation of grid connected solar powered electric vehicle charging using MATLAB/Simulink and HOMER renewable energy software by showing the power flow and overall cost of the system.

1.6 Significance of the Study

For the generation of energy that is environmentally friendly, sources that naturally replenish themselves are utilized. In terms of cost savings and sustainability, using RES for electric car charging infrastructure provides an important advantage by reducing dependency on petrol. Grid-connected solar electric vehicle charging has several advantages, including supporting the electric utility's distribution system and providing rapid charge for EVs (electric vehicles) travelling through Adama City and for EV owners living in the city.

1.7 Motivation of the Study

Researching this topic is quite thrilling because EV technology is so futuristic. The technology for batteries and power electronic converters is periodically updated, which raises hopes for EV users to easily operate EV. Technology for power electronic converters and batteries is quickly gaining in prominence. PV systems produce renewable energy that can be utilized to power homes and businesses, which has the potential to result in significant electricity bill savings. In addition, using PV systems connected to the grid lessens the environmental impact of energy use because they create clean, sustainable energy with no hazardous emissions.

1.8 Thesis Outline

This thesis was structured into five chapters. Chapter one provided an introduction, including the background of the study, statement of the problem, objective, scope and limitation, significance, area of applications, and motivation. Chapter two delved into a comprehensive literature review on the background and structural overview of the electric vehicle battery charging system. Moving on to chapter three, it encompassed the analysis of data, modeling of the electric vehicle battery charging system, and the development of the proposed system. Chapter four presented the proposed results and analysis obtained from the implementation of the system. Finally, chapter five concluded the thesis by discussing the overall findings, drawing conclusions, and providing recommendations.

CHAPTER TWO

2. THEORETICAL BACKGROUND AND LITERATURE REVIEW

2.1 Theoretical Background

The world is converting to renewable energy sources because of a number of factors, including increasing carbon dioxide emissions, fluctuating oil costs, and high world energy consumption. The development of electric vehicles may improve public health while reducing climate change-causing emissions. The key challenge to developing an optimal system that can meet energy needs, improve sustainability, and reduce negative environmental effects is how to supply electric vehicles with the energy required (AlHammadi , et al., 2022) (Arif, 2021).

AC grid charging can have a negative impact on the adoption of EVs, by requiring customers to charge during off-peak demand times. Furthermore, grid-connected rapid charging can worsen power quality, create current harmonics and supra-harmonics, hinder generation demand balancing, cause voltage flickers and phase variations, and cause unexpected load peaks. The electricity system is already operating close to its operational and stability boundaries as a result of aging infrastructure. The dependability and resilience of the AC grid will be further strained by the inclusion of new FCS load centers. (Powar & Singh, 2023)

The integration of photovoltaic (PV) solar energy into electric vehicle (EV) charging systems is gaining momentum due to the rapid growth of EVs and the need to address the environmental impact of greenhouse gases (GHG). However, PV-powered charging systems come with their own set of challenges. These include inadequate PV production for efficient charging, continued dependence on the electricity grid, and a lack of a business model to accurately predict the financial profitability and economic advantages of PV charging systems (PVCS).

There are two primary operational modes for PVCSs. The first is the grid-connected mode, where EVs are charged using a combination of power from the grid and PV production. This can be achieved through a microgrid-based system that incorporates stationary storage, grid connection, and EV charging using a combination of PV power, stored energy, and grid supply.

The second operational mode is the standalone mode, also known as the island mode, where charging is entirely reliant on green energy sources. However, in this mode, PV production alone may be insufficient to achieve a full charge, even with the presence of energy storage, which is limited in capacity (Sechilariu, et al., 2021).

2.1.1 Electric Vehicles

Electric vehicles (EVs) are a type of vehicle that utilizes electrical power as its primary driving force. In comparison to traditional fuel-powered vehicles, EVs offer several advantages such as emission-free operation, reduced noise levels, and high energy efficiency. The widespread adoption of EVs can significantly decrease reliance on oil resources and facilitate the implementation of energy-saving and emission reduction measures (Yi & Jingru, 2016). It should be noted that the term "electric cars" encompasses various types of vehicles, including battery electric vehicles (BEVs), hybrid electric vehicles (HEVs), and fuel cell electric vehicles (FCEVs) within its broad definition (Dv., 2021).

Battery Electric Vehicle

A battery electric vehicle (BEV), often referred to as a fully electric vehicle, is powered solely by high-capacity rechargeable battery packs, eliminating the need for a traditional gasoline engine. These battery packs can be charged from an external source. The electric motor and internal electronics of a BEV are fueled by the chemical energy stored in these rechargeable batteries. By utilizing this technology, BEVs have the capacity to reduce both CO2 emissions from the light-duty vehicle fleet and the dependence on fossil-fuel-powered cars (Dv., 2021).

Hybrid Electric Vehicle

Hybrid Electric Vehicles (HEVs) are vehicles that incorporate both an internal combustion engine (ICE) and batteries to propel the vehicle. This dual power system allows the vehicle to operate using either the battery or the ICE as the energy source. Consequently, HEVs are commonly referred to as vehicles with two power sources. One advantage of HEVs is their ability to recharge the battery by harnessing the kinetic energy generated during regenerative braking, making them particularly well-suited for urban driving scenarios. In city driving, where frequent starts and stops are common, HEVs exhibit superior performance compared to rural or highway driving situations (Dv., 2021).

Fuel Cell Electric Vehicle (FCEV)

Similar to electric vehicles, Fuel Cell Electric Vehicles (FCEVs) also feature an electric motor. However, instead of relying on battery packs, FCEVs utilize a fuel cell tank that utilizes hydrogen as its energy source. FCEVs are categorized as either fuel cell electric vehicles or fuel cell hybrid electric vehicles, depending on their specific configuration (Dv., 2021).

2.1.2 Electric Vehicle Charging Standards

Various EV charging standards are employed worldwide to address the infrastructure needs for charging electric vehicles. For instance, the United States utilizes the IEEE and SAE standards, while Japan and Europe rely on the CHAdeMO charging standard. The Standards Administration of China (SAC) adopts GB/T standards, which are similar to the IEC standard. In the SAE standard, the power level is referred to as "Level," whereas the IEC standard uses the term "Mode" to denote the level of power (Arif, 2021).

In Ethiopia both the AC and DC chargers are available. Figure 2.1 shows a typical AC EV charger located at Green Tech Africa head office, Addis Ababa with two output ports with 32 Ampere current each.

Figure 2.1: AC EV charger (Level 2)

Charging Level 1/Mode 1 as shown in Table 2.1 is most used at homes or offices for overnight slow charging. The Level 2/Mode2 and Level 3/Mode 3 charging modes are for both the public and private charging facilities and mode 4 in IEC and SAE is used for fast charging.

Table 2.1: IEC and SAE standards: Current and Voltage level for AC and DC charging

Standards	Phase	Level/Mode	Voltage (V)	Current (A)	Source
IEC62196	Single	Mode 1	120	16	AC
	Single	Mode 2	240	32	
	Single	Mode 3	250	32-250	
	DC	Mode 4	600	400	DC
IEC61851	Single	Mode 1	120	16	AC
	Single	Mode 2	240	80	
	DC	Mode 4	200-450	80	DC
SAEJ1772	Single	Level 1	120	16	AC
	Single	Level 2	240	32-80	
	DC	Level 1	200-450	80	DC
	DC	Level 2	200-450	200	

EVs can be recharged using either AC or DC charging systems. In both approaches, the power sourced from the electrical grid is converted from AC to DC and utilized to replenish the vehicle's battery (Mouli & Ram, 2018) (Gautam , Gautham , & Pavol , 2022)

AC charging of EV

Onboard EV AC/DC power converter can be implemented to charge electric vehicle via single or three phase AC power system. There are four types of AC charging systems however, three of them are currently available around the globe as shown in figure 2.2**.**

1. Type1, single phase charger used in the USA (SAE J1772-2009)
2. Type 2 Mennekes, single and three phase chargers used in Europe (VDE-AR-E 2623-2-2)
3. Type 3, single phase and three phase chargers from the EV plug alliance
4. Tesla dual charger for single phase AC and DC used in the USA

AC charging is constrained to a maximum power level of 22 kW, primarily due to space and weight limitations in electric vehicles (EVs). Type 1 plug chargers enable single-phase charging and utilize three power pins: phase (L1), neutral (N), and earth (E) pins. In Europe, the widely adopted Type 2 charging plug incorporates five power pins: three phase pins (L1, L2, L3), neutral (N), and earth (E) pins (Gautam , Gautham , & Pavol , 2022).

(a) (b) (c)

Figure 2.2: AC charging plugs (a) US Type 1 SAE, (b) European Type 2 Mennekes, and (c) Tesla plug *(Michael Hicks, 2023)*

DC charging of EV

DC charging is employed to enable high-power and faster charging of electric vehicles (EVs) while overcoming the limitations of on-board chargers in terms of weight and size. It corresponds to Mode 4 in IEC 61851, Mode 4 in IEC62196, and Level 1 and 2 in SAE J1772, as indicated in Table 2.1. In DC charging, a dedicated off-board AC/DC converter is utilized to supply direct current (DC) power directly to the EV's battery. Unlike on-board chargers, off-board chargers are not restricted by space and weight limitations, allowing them to achieve charging power levels of up to 900 kW. Various types of DC charging systems are currently in use worldwide, and some of these systems are listed in Figure 2.3.

1. CCS/COMBO (Combined Charging System, Combo 1 and Combo 2)
2. Type 4 CHAdeMO
3. Chinese GB/T
4. The more recent ChaoJi plug coming from the joint efforts of CHAdeMO and GB/T
5. Tesla dual charger for single phase AC and DC used in USA and
6. Tesla Type 2 plug used for DC charging in Europe (recently abandoned to make use of CCS Type 2)

(a) (b) (c)

Figure 2.3: DC charging plugs (a) CCS/COMBO (b) CHAdeMO (c) Chinese GB/T *(Mikael Hicks, 2023)*

In a DC charging system, three power pins are utilized for power transfer: DC power pins DC+, DC-, and an earth pin (E). However, these pins differ in terms of the communication and control protocols employed. For instance, CHAdeMO utilizes CAN bus communication and seven pins for control and communication, while CCS utilizes Power Line Carrier communication (PLC) and two communication pins. CCS/COMBO stands out because its plug incorporates both AC and DC charging pins, with the AC charging pins located at the top and the DC charging pins at the bottom. As a result, CCS has two types of charging plugs known as CCS Type 1 and CCS Type 2, depending on whether the AC section of the connector uses the AC Type 1 or AC Type 2 connector. Tesla's charging system is unique in that it utilizes the same two power pins for both single-phase AC and DC charging, along with two communication pins. However, it's important to note that the Tesla charging connector is designed exclusively for Tesla electric vehicles (Gautam , Gautham , & Pavol , 2022).

DC charging provides a fast charging solution for electric vehicles with battery capacities ranging from 20 to 100 kWh. In the constant charging region, it allows for a charging time of 5 to 20 minutes. To accommodate the high charging currents (ranging from 100 to 600 A), liquid-cooled cables are utilized, ensuring that the cable size and weight remain manageable for human handling during vehicle connection. DC charging is particularly suitable for vehicle-to-grid (V2G) applications, which involve bidirectional charging technology that enables the connection between the EV and the supply system. Both CHAdeMO and CCS/Combo standards support V2G applications, providing the necessary infrastructure for intelligent charging and power exchange between the vehicle and the grid.

2.1.3 Challenges to be Considered in Off-board Charging System

There are issues with off-board chargers that use high power levels that must be resolved in relation to fast charging:

- Component availability: the selection of components will be more constrained and maybe more expensive at high power levels;
- Grid impact: as power and the number of fast chargers increase, the grid is subject to higher harmonic distortion, which damages delicate equipment;
- Reliability: Due to higher power, components in rapid chargers are put under additional stress. In addition, commercial off-board chargers will undergo more cycles than personal on-board chargers, which could result in a shorter lifetime.

2.1.4 On-Board and Off-Board Charger

On-board chargers and off-board chargers are the two main categories for EV battery chargers. Off-board chargers, sometimes referred to as standalone fast-charging stations, function like filling stations for vehicles that run on liquid gasoline by supplying a rapid, high-power charge. Pure-battery Electric Vehicles range can be significantly increased by off-board charging stations, which are typically situated in public spaces like shopping malls, parking lots, and highway services. The comparison between onboard and offboard charger is shown in table 2.2.

Table 2.2: Comparison of on-board and off-board chargers *(Habib, Khan, & Abbas, 2017)*

Chargers	Benefit	Challenges
On-board chargers	Problem of battery heating is not a concern	Less energy transfer (kW) and slow charging
	Charge at low-power levels	Weight on EV is added
	Recharge at any place using electrical outlet	Size and weight restriction due to EV design
Off-board chargers	Higher transfer of energy (kW) and less complex BMS system	Needs to address battery heating issue
	Fast charging	Complex with higher cost
	Weight on EV is removed	No flexibility to charge at various places

The offboard charger is a charging unit that is physically distinct from the electric car. It is usually a stand-alone machine deployed at charging stations or other specific locations. Offboard chargers can produce more power, often ranging from 50 kW to several hundred kilowatts, allowing for quicker charging rates. They are often used for Level 3 DC fast charging, also known as DCFC (DC Fast Charging), which enables quick EV charging. These chargers can be modified or changed independently of the vehicle in contrast with the onboard chargers, offboard chargers provide greater flexibility and scalability (Shahir, Gheisarnejad, Sadabadi, & Khooban, 2021). This enables to easily expand or modify charging infrastructure to match emerging technologies and standards.

2.2 Front-End AC-DC Converters

Power electronics converters play a crucial role in transforming electrical power between AC and DC forms. The conversion of electric power is essential for power control and conditioning, and it is made possible by the switching characteristics of power devices. Static power converters fulfill the task of power conversion, acting as switching matrices where switches are turned on and connected to the power source to achieve the desired output voltage or current (Rashid, 2014). In charging systems, various converter types are employed, including DC-DC, DC-AC, and AC-DC converters, which are widely utilized for their respective functionalities.

Three-phase rectifiers can be categorized as either unidirectional or bidirectional. Unidirectional rectifiers include well-known topologies such as simple diode bridge rectifiers, Vienna rectifiers, and Swiss rectifiers. These rectifiers allow current flow in a single direction. On the other hand, bidirectional rectifiers have the capability to feed electricity generated by a vehicle back into the grid when needed. While V2G (Vehicle-to-Grid) operation has proven useful in low-power chargers, its application in high-power chargers is still relatively new. In DC fast charging stations that utilize renewable energy sources and energy storage systems, Level 3 bidirectional AFE (Active Front End) rectifiers with V2G capabilities are employed. These rectifiers help balance the impact of fast chargers on the grid and offer additional grid services (Chandler , Gartner, & Jones, 2018).

Boost-type and buck-type are the two types of bidirectional rectifiers. The DC link voltage of boost-type rectifiers is higher than the AC side voltage, but the DC link voltage of buck-type rectifiers is the opposite. Less current is required to provide the same amount of power due to the greater DC link voltage, which can be advantageous, particularly for high-power systems. Only three-phase, boost-type bidirectional topology is taken into consideration in this thesis.

2.2.1 Three-Phase Two-Level Six-Switch Boost Rectifier

The three-phase, two-level boost-type rectifier is made up of a DC side filter capacitor, an AC side boost inductor, and six active switches. The circuit topology is depicted in Figure 2.4. It is the boost-type two-level rectifier with a straightforward, reliable, and well-known structure. Commercial H-bridges can be used to construct this topology. In comparison to three-level converters, the two-level six-switch rectifier design has a limited maximum switching frequency and calls for greater volume input inductors. (Zhaksylyk, et al., 2023)

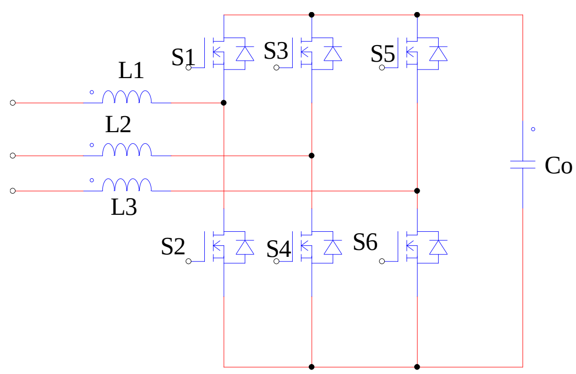

Figure 2.4: Three-phase two-level six-switch boost-type rectifier *(Zhaksylyk, et al., 2023)*

The three phase voltage equations are:

$$V_a = L\frac{di_a}{dt} + Ri_a + V_{ra} \tag{2.1}$$

$$V_b = L\frac{di_b}{dt} + Ri_b + V_{rb} \tag{2.2}$$

$$V_c = L\frac{di_c}{dt} + Ri_c + V_{rc} \tag{2.3}$$

By considering grid current and voltage vectors, the input current dynamic equation is

$$i_s = \frac{2}{3}\left(i_{sa} + ai_{sb} + a^2 i_{sc}\right) \tag{2.4}$$

$$V_{afe} = \frac{2}{3}\left(V_{an} + aV_{bn} + a^2 V_{cn}\right) \tag{2.5}$$

Considering the switching state of the converter and the DC link voltage

$$V_{afe} = S_{afe} V_{dc} \tag{2.6}$$

Where V_{dc} and S_{afe} are the DC link voltage and switching state vector of the rectifier

$$S_{afe} = \frac{2}{3}\left(S_1 + aS_2 + a^2 S_3\right) \tag{2.7}$$

Where S_1, S_2 and S_3 are the switching states

The input current dynamics equation can be rewritten in the stationary αβ frame as

$$L_s \frac{di_s}{dt} = V_s - V_{afe} - R_s i_s \tag{2.8}$$

Where i_s and v_s are the input current and line voltage vectors and V_{afe} is the voltage generated by the converter

2.3 Isolated DC-DC Converters Review

A DC converter is an electronic device used to convert a direct current (DC) input into a DC output. It operates in a manner similar to an AC transformer, but with the ability to adjust the turns ratio continuously. This flexibility enables the converter to step down or step up a DC voltage source as required. DC converters play a crucial role in the conversion of energy within the growing realm of renewable energy technology (Rashid, 2014).

Conventional non-isolated DC-DC converters, such as buck, boost, and buck-boost models, connect the input side and output to the same potential (no isolation). Non-isolated DC-DC converters have the disadvantage that any issue on the output side will affect the input side. This disadvantage can be avoided by using standalone DCDC converters. Potential isolation, safety, electromagnetic isolation, separation between the input side and the output side, and freedom to add new modules are all benefits of isolated DC-DC converters. (Kanaparthi, Singh, & Ballal, 2022)

Table 2.3: Comparison of Isolated DC-DC converters

Converter	Topology	Advantages	Limitations
Fly-back	Isolated	➢ Simple and low cost	➢ Low efficiency at high power level ➢ Limited output power ➢ Voltage regulation issues during load transients
Full-bridge Isolated PWM Buck Converter	Isolated	➢ High efficiency ➢ Low output ripple ➢ Good voltage ripple	➢ Complex control ➢ High cost ➢ Limited output power
Bidirectional dual active bridge	Isolated	➢ Bidirectional power flow capability ➢ Suitable for battery energy storage system	➢ Complex control ➢ High cost ➢ Limited output power
Full-bridge LLC Resonant	Isolated	➢ High efficiency ➢ Low output ripple ➢ Good voltage regulation ➢ High power density ➢ Smaller magnetic components	➢ Complex control ➢ High cost

2.4 Full-Bridge LLC Converter

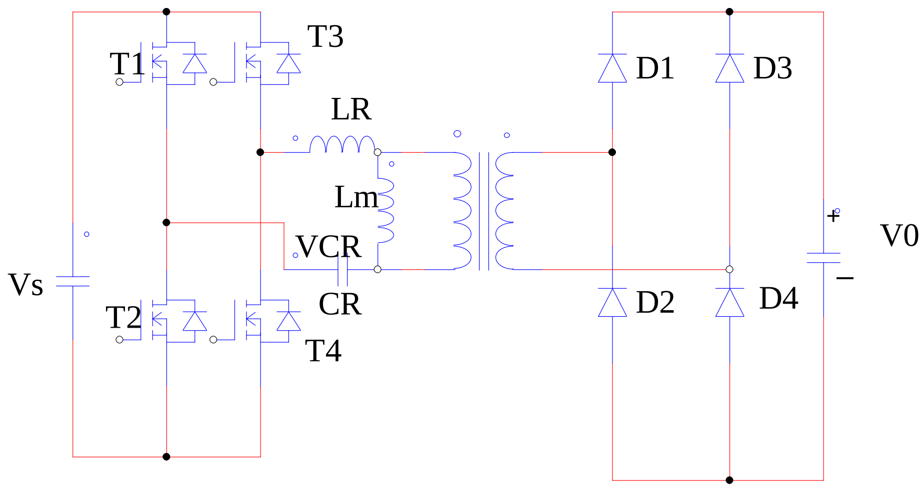

Figure 2.5: A Full-Bridge LLC converter *(Panda & Rout, 2016)*

One of the best alternatives for dc/dc conversion in situations requiring a consistent output voltage has been demonstrated to be the full bridge LLC resonant converter depicted in Figure 2.5. ZVS and ZCS, respectively, stand for the primary MOSFETs turning on and the freewheeling didoes shutting off when the input impedance is inductive. ZCS turns off secondary-side diodes when the switching frequency is less than f_r, which is the resonance frequency of L_r and C_r (Panda & Rout, 2016).

2.4.1 Converter Voltage Gain

The total gain of a power converter system can be calculated using the product of three independent gains.

Converter Gain = Switching Bridge Gain * Resonant Tank Gain * Transformer Turn Ratio (Ns/Np)

Where, the switching bridge gains for the full and half bridges are 1 and 0.5, respectively. By multiplying these three individual gains together, the overall gain of the converter can be obtained. It represents the combined effect of the switching bridge, resonant tank, and transformer on the voltage conversion process in the power converter system. The resonant tank gain can be found out by looking at the analog resonant circuit shown in Figure 2.6. The size of the transfer function is the resonant tank gain in Equation 2.7 (Abdel-Rahman, 2012).

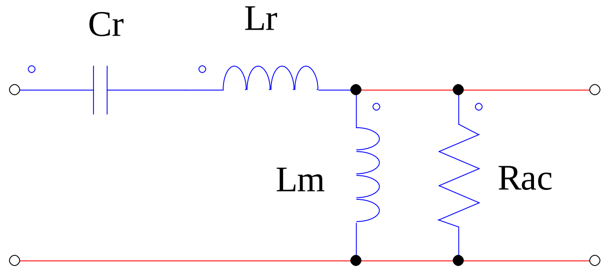

Figure 2.6: Equivalent resonant circuit

$$K(Q,m,F_x)=\frac{Fx^2(m-1)}{\sqrt{(m*Fx^2-1)^1+Fx^2*(Fx^2-1)^2*(m-1)^2*Q^2}} \qquad (2.9)$$

Where, Q is the quality factor expressed as;

$$Q=\frac{\sqrt{L_r/C_r}}{R_{ac}} \qquad (2.10)$$

L_r is resonant inductance

C_r is resonant capacitance and

R_{ac} is reflected load resistance;

$$R_{ac}=\frac{8}{\pi^2}*\frac{N_p{}^2}{N_s{}^2}*\frac{V_0{}^2}{P_{0\_max}} \qquad (2.11)$$

F_x is normalized switching frequency;

$$F_x=\frac{f_s}{f_r} \qquad (2.12)$$

$$f_r=\frac{1}{2\pi\sqrt{L_r*C_r}} \qquad (2.13)$$

f_r is resonant frequency of resonant circuit

Ratio of total primary inductance to resonant inductance m is expressed in equation 2.14

$$m=\frac{L_r+L_m}{L_r} \qquad (2.14)$$

Where, L_m is Magnetizing inductor

The resonant tank gain K can be plotted along with the normalized switching frequency for various values of the quality factor Q and any particular value of m as illustrated in Figure 2.7 Lower Q curves correspond to operations with lighter loads whereas higher Q curves indicate operations with heavier loads. Additionally, it is observed that all Q curves (load conditions) have a unity gain and cross at the resonant frequency point (at F_x =1 or $f_s = f_r$). (Abdel-Rahman, 2012)

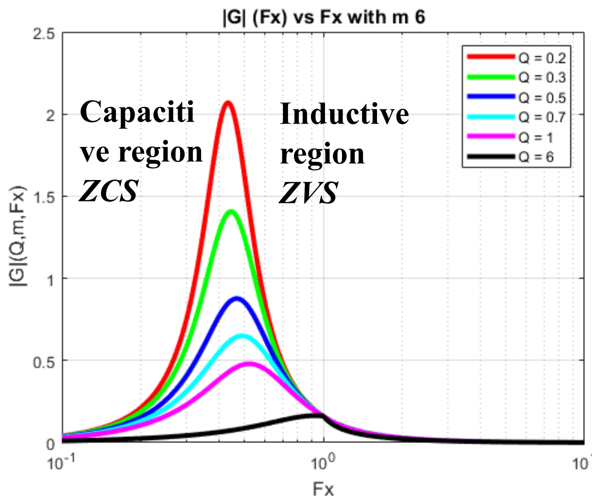

Figure 2.7: Resonant tank gain plot

Zero Voltage Switching (ZVS) is only attainable in the inductive region, and because capacitive operation causes the current to lead the voltage rather than the other way around, the MOSFET's current will reverse before it turns off. Once it does, the reverse current will flow in the MOSFET's body diode, resulting in a body diode hard commutation when the other MOSFET in the bridge turns on. This will then result in reverse recovery losses, noise and device failure.

The switching cycle of the converter only has two possible operations, and each of the modes mentioned may include one or both of these activities.

I. **Power delivery operation:** In this operation, the voltage across the magnetizing inductor corresponds to the positive/negative reflected output voltage, while the magnetizing current charges/discharges accordingly. The transformer and rectifier work together to transfer the disparity between the resonant current and the magnetizing current to the secondary side, where power is supplied to the load. This process takes place twice within the switching cycles and is repeated in two subsequent instances. Figure 2.8 displays the circuit that corresponds to this mode, wherein the resonant tank is stimulated with a positive voltage, resulting in the current resonating in the positive direction during the first half of the switching cycle.

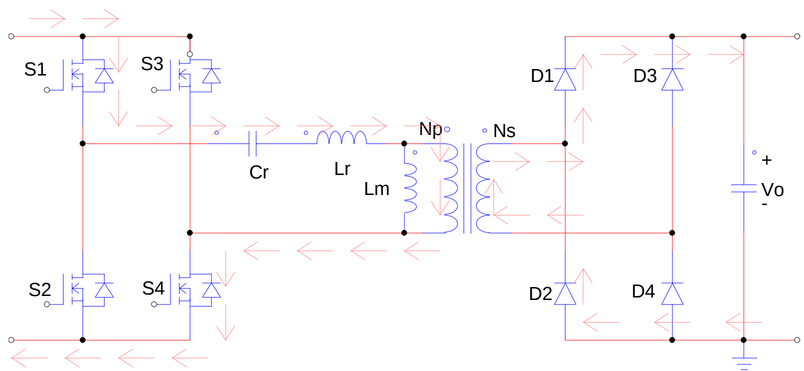

Figure 2.8: Current flow in the positive direction of full bridge LLC converter

Figure 2.9 illustrates the circuit associated with this particular mode. This mode occurs when the resonant tank is stimulated with a negative voltage, resulting in the current resonating in the opposite direction during the second half of the switching cycle.

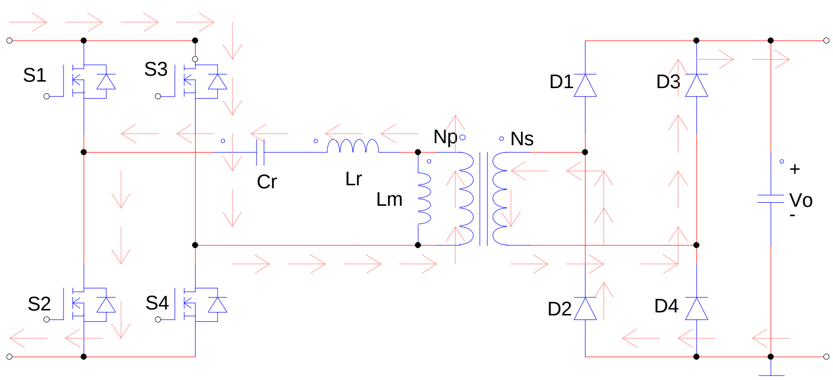

Figure 2.9: Resonant and magnetizing current flow through the transformer and rectifier

II. **Freewheeling operation:** happen after the power delivery operation if the resonant current reaches the transformer magnetizing current; this only occurs when $f_s > f_r$; as a result, the primary current during the freewheeling operation will only slightly change, and can therefore be roughly estimated to be unchanged for simplicity. In Figures 2.10,

(a) and (b), the analogous circuits of the freewheeling operation in either half of the switching cycle are depicted.

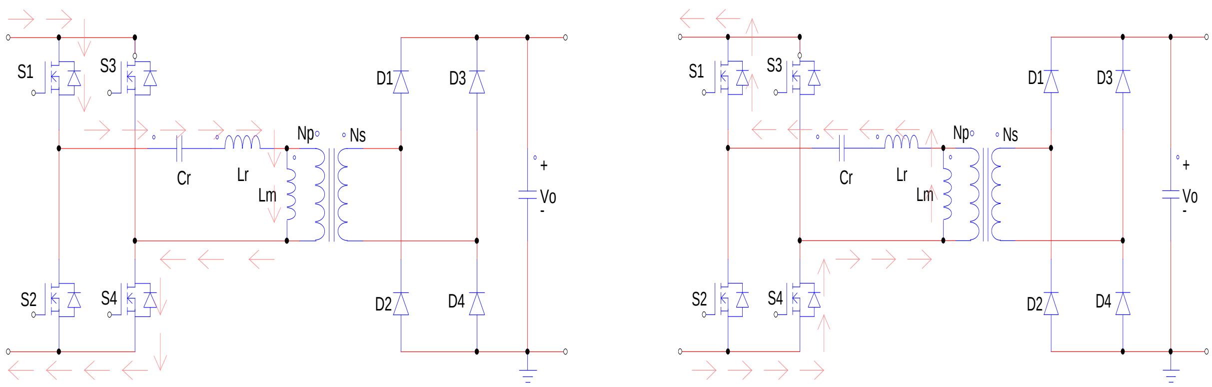

(a) (b)

Figure 2.10: Primary current flow in the freewheeling operation

2.4.2 Modes of Operation

The converter operates in three different modes based on the input voltage and load current conditions, as the gain of the LLC network is modulated by frequency (Abdel-Rahman, 2012).

I. At Resonant Frequency Operation $f_s = f_r$

Each half of the switching cycle encompasses an entire power supply operation, with the resonant half cycle concluding within the switching half cycle. At the end of the switching half cycle, the rectifier current reaches zero, while the resonant inductor current attains the magnetizing current. The transformer turns ratio is carefully chosen to ensure that the converter operates at this specific point under nominal input and output voltages. This selection allows the resonant tank to have unity gain, optimizing the operation and efficiency of the system.

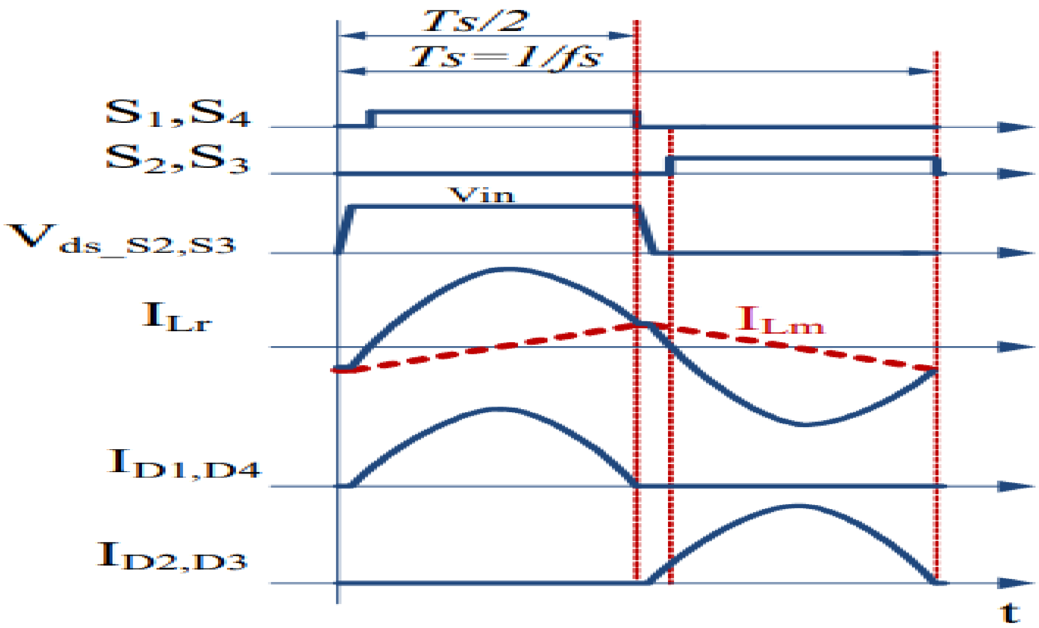

Figure 2.11: Converter operation waveform at resonant frequency

II. Above Resonant Frequency Operation $fs > fr$

In a manner akin to resonant frequency operation, each half of the switching cycle involves a partial power delivery process. However, the distinction lies in the fact that the resonant half cycle is not fully completed; it is interrupted by the start of the other half of the switching cycle.

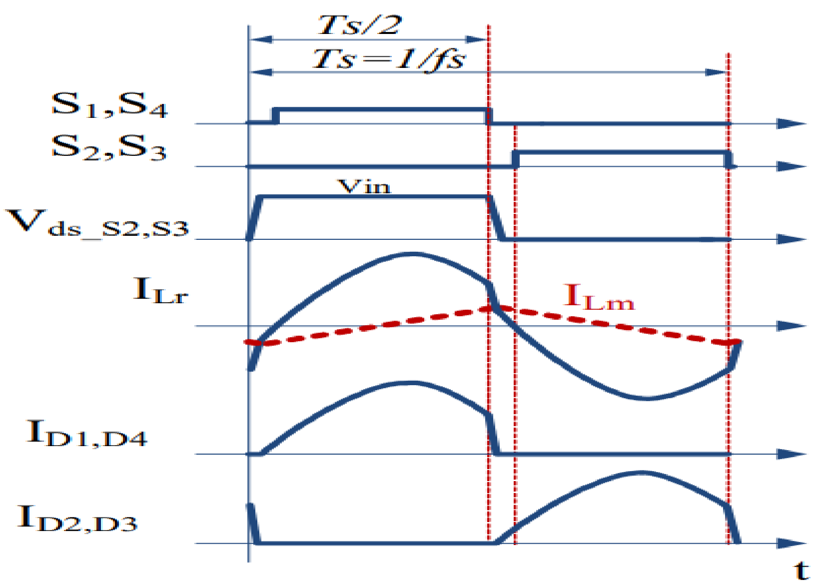

Figure 2.12: Waveform for converter operation at switching frequency greater than resonant frequency

Consequently, this interruption leads to heightened turn off losses in primary side MOSFETs and creates a scenario of hard commutation in secondary rectifier diodes. This mode of operation is employed when the input voltage is higher, necessitating a step-down gain or buck operation.

III. Below Resonant Frequency Operation $f_s < f_r$

A power delivery operation is present in each half of the switching cycle. When the resonant half cycle is completed and the magnetizing current is reached by the resonant inductor current I_{Lr}, the freewheeling operation begins and continues until the end of the switching half cycle, causing increased conduction losses on the primary side. In this mode, if a step-up gain or boost operation is necessary, the converter runs at lower input voltage.

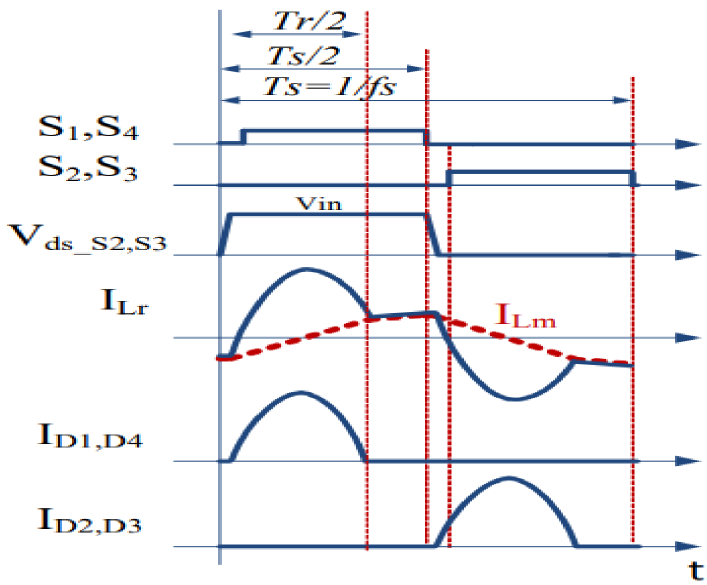

Figure 2.13: Waveform for converter operation at switching frequency less than resonant frequency

2.5 Photovoltaic (PV) Power System

Solar energy is a freely available and naturally renewable resource that offers environmental benefits by reducing greenhouse gas emissions. Ethiopia, in particular, boasts remarkable solar radiation levels. Photovoltaics, also known as solar cells, are devices that directly convert solar radiation into electrical current. These photovoltaic systems can be connected to a utility's distribution lines or other facilities, allowing excess electricity to be sold back to the grid.

Moreover, solar energy can be harnessed for electric vehicle (EV) charging infrastructure, complemented by energy storage systems (ESS) to overcome any limitations of PV panel output (T. Li et al., 2018). The use of PV power to recharge EV batteries enhances the environmental advantages of EVs, as PV-generated electricity has low greenhouse gas emissions throughout its lifecycle. Charging EVs with PV power during peak PV production periods, typically during the daytime, further reinforces the benefits of reduced emissions during vehicle operation (Sechilariu, et al., 2021).

Irradiance is the measurement of the quantity of solar radiation that hits a surface. Watts per square meter (W/m2) is the unit of measurement for irradiance. Just before the sun's radiation reaches the earth's atmosphere, the solar irradiance was estimated to be 1,366 W/m2. On a clear day, the Earth's atmosphere's dust and water vapor absorb or reflect close to 30% of the sun's radiant energy. The 1,366 W/m2 measured in space has been reduced to 1,000 W/m2 by the time solar radiation reaches a solar array. The transformation of solar energy into a form that can be used as electrical power is the main goal of photovoltaic (PV) technology. The solar cell, which directly transforms the energy of sunlight into electricity, is the fundamental component of a photovoltaic (PV) system (Radish, 2015) (Chiras, 2020).

2.5.1 PV cells –modules–strings/Arrays

Cells, modules, and arrays make up a photovoltaic system's fundamental building blocks. To increase the current, individual PV cells are joined together to create a module (referred to as a "PV module"). The modules are then connected in an array (referred to as a "PV array"). PV arrays can be connected either in series or parallel, depending on the required current or voltage. Strings of PV cells or modules are often connected in parallel to generate current, whereas PV cells or modules are typically connected in series to generate voltage. The arrangement of a typical PV cell, module, and array is shown in Figure 2.14, which illustrates the configuration of a typical PV cell, module, and array.

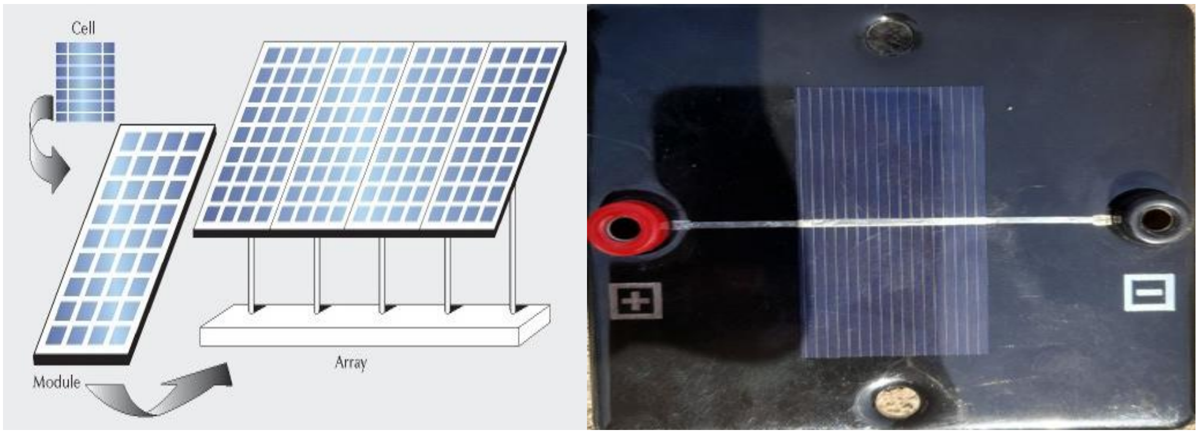

Figure 2.14: Basic structure of PV cell module and array

There are five types of solar cell technologies:

i. **Single-Crystalline Silicon:** The primary material used in its construction is monocrystalline silicon. To produce a monocrystalline silicon cell, the raw silicon material undergoes purification, melting, and crystallization processes to form ingots. These ingots are then sliced into thin wafers, which are used to create individual cells. This technique, although the oldest and most costly, is also the most efficient and widely adopted technology for converting sunlight. The cell efficiency typically ranges from 14% to 18% (Patel, 2006).

ii. **Polycrystalline or multi-crystalline silicon**: This particular photovoltaic cell is relatively large and can be conveniently shaped into a square, minimizing any unused space between cells. Although its conversion efficiency is slightly lower compared to single crystal cells, the manufacturing costs are also reduced. The cell efficiency typically ranges from 10% to 13% (Patel, 2006).

iii. **String Ribbon: String Ribbon:** This represents an enhancement in the production of polycrystalline silicon. The manufacturing process requires less effort, resulting in even lower costs. The cell efficiency typically ranges from 8% to 10% on average (Patel, 2006)**.**

iv. **Thin film solar cell: Thin film solar cell:** These solid-state cells exhibit a less organized arrangement of silicon atoms compared to crystalline cells. By incorporating multiple junctions, this type of photovoltaic cell achieves optimal efficiency, estimated to be around 13%, while reducing installation costs. The efficiency of these cells typically ranges from 6% to 10% (Patel, 2006).

v. **Amorphous:** When silicon material is vaporized and then deposited on glass or stainless steel, this sort of PV cell develops. Compared to alternative methods, the cost is lower. Cell efficiency ranges from 4% to 7% on average and decreases as the temperature rises. Compared to thin-film cells, crystalline cells are more heat-sensitive. For every degree Celsius that a crystalline cell's temperature raises, the production of the cell falls by approximately 0.5%. Due to the fact that amorphous silicon cells' output reduces by about 0.2% for every degree Celsius that the temperature raises, modules should be maintained as cold as possible in extremely hot environments (Patel, 2006).

The market provides photovoltaic modules in sizes ranging from 80W. These modules can be used for standalone systems or grid integration. According to their maximum DC power output (watts) under the Standard Test Conditions (STC), PV modules and arrays are often assessed for performance (STC) (Yehualawork, 2019).

Standard test conditions include an air mass with a 1.5 spectral distribution, an incident solar irradiant intensity of 1000 W/m2, and a module (cell) operating temperature of 25 °C (with a tolerance of 2 °C) or 77 °F. The atmosphere is where sunlight must pass in order to reach the surface of the earth. STC is the point where the most energy will be produced by determining a stable condition, thus enabling the comparison of various solar modules and cells. The STC describes all of the conditions to which the solar module is exposed after mounting. The power production of a solar panel is affected by all of these conditions listed (Pop & Avram, 2018)

- The location and time of year have an impact on irradiance.
- As the irradiation increases, the current rises.
- As the cell temperature rises, the voltage falls.
- With respect to space, time, and season, air mass has different values.

2.5.2 Equivalent Circuit of PV cell

To realize the performance of a photovoltaic cell, it is convenient to construct a model that is electrically equivalent with the existing solar cell. The ideal photovoltaic cell model consists of a current source in parallel with a diode. The function of the ideal current source is delivering current from the solar cell in the form of solar flux.

A photovoltaic one-diode model, depicted in Figure 2.15, is utilized alongside a set of circuit equations to represent the typical current-voltage (I-V) behavior of PV modules and arrays (Ikegami, Maezono, Nakanishi, Yamagata, & Ebihara, 2001). The output current of a photovoltaic system is influenced by temperature and solar radiation levels (Tilahun, 2020) The internal losses, represented by Rs, arise from current flow and are influenced by factors such as p-n junction depth, impurities, and contact resistance. On the other hand, the shunt resistance, Rsh, is inversely proportional to the leakage current towards the ground. In an ideal PV cell, Rs is zero, and Rsh is infinite. The PV conversion efficiency is highly sensitive to small changes in Rs but is not significantly affected by variations in Rsh. Even a slight increase in Rs can have a significant impact on reducing the PV output (Lera, 2020).

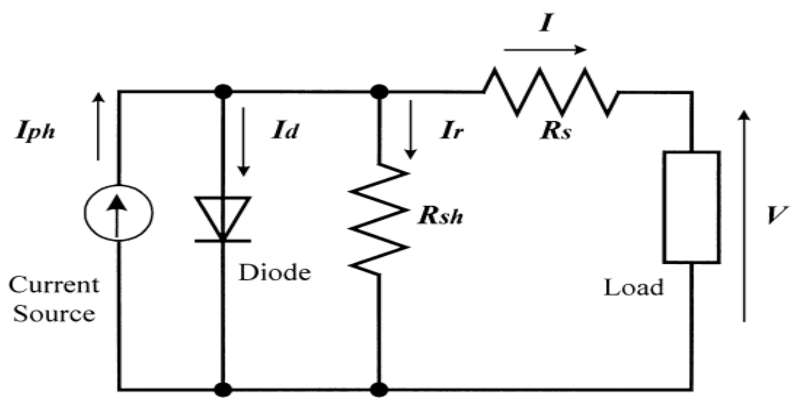

Figure 2.15: Equivalent circuit for PV arrays *(Ikegami, Maezono, Nakanishi, Yamagata, & Ebihara, 2001)*

$$I = Iph - Id - Ir \tag{2.15}$$

Open-circuit voltage V_{oc} of the cell is obtained when the terminals of the module disconnected, in which the load current is zero. It is expressed analytically in the following expression:

$$Vo = (Iph - Id)Rsh \tag{2.16}$$

When the light-generated carriers within the solar cell are restricted from exiting, the forward bias of the junction intensifies until a state is reached where the current generated by the light precisely balances the diffusion current caused by the forward bias. As a result, the net current becomes zero. The voltage observed at the terminals of the cell in this situation is referred to as the open-circuit voltage (Voc), as represented in Equation 2.17.

$$Voc = (\frac{nKT}{q})\ln(\frac{Iph}{Io}+1) \quad (2.17)$$

Where n is the ideality factor, a common value of 1.2 for silicon mono and 1.3 for silicon poly, 1.3 for gallium arsenide (GaAs), and 1.5 for cadmium telluride (CdTe), K is the Boltzmann constant (1.381 *10-23 J/K), T is the junction temperature on the absolute scale °K, q is the electron charge (1.602* 10-19 C), and Io is the saturation current of the diode (A) (Badase, 2020).

2.5.3 PV Cell Performance Characteristics

Typically, photovoltaic arrays are installed in a stationary position and angled towards the south to maximize energy production during noontime and throughout the day. The orientation of fixed panels must be selected with care to capture the highest energy yield for a particular season or the entire year. Figure 2.16 illustrates the optimal operating point of a PV array referred to as the maximum power point (MPP). To extract the maximum power from the PV panel under the given temperature and insolation conditions, a maximum power point tracker (MPPT) is used to regulate either the operating voltage or current.

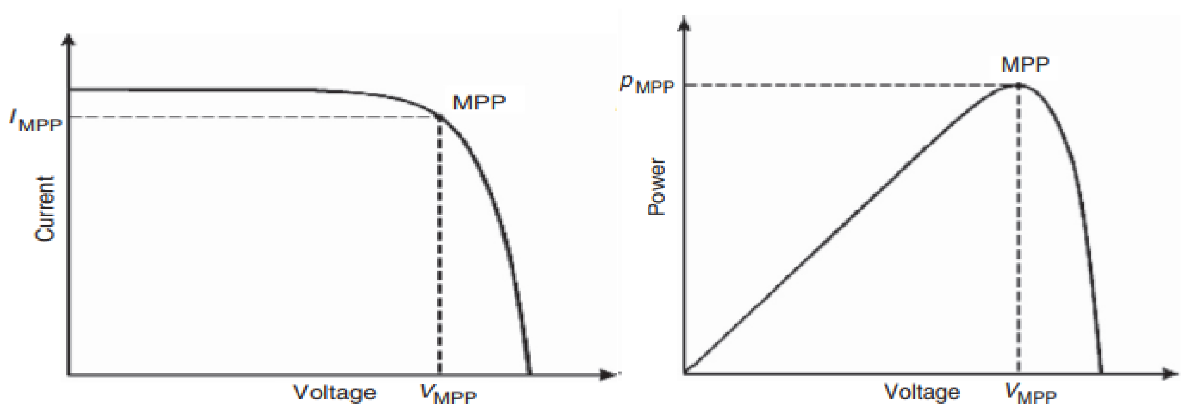

(a) (b)

Figure 2.16: I-V characteristic of a solar cell showing maximum point (MPP); (b) P-V characteristic of a solar cell showing MPP

2.6 Maximum Power Point Tracking

A photovoltaic (PV) generator exhibits a single I-V curve, determined by the irradiance and temperature conditions. Within this curve, there exists a singular point known as the "maximum power point" (MPP), where the generator operates at peak efficiency and delivers its maximum power output. The MPP varies over time due to changes in the I-V curve resulting from fluctuations in irradiance and temperature. The Maximum Power Point Tracking (MPPT) device is responsible for maintaining the generator operating at the MPP. Serving as a switch-mode power converter, the MPPT plays a crucial role in PV systems by optimizing the output power generated by the PV. In grid-connected systems, the MPPT device is typically positioned before the input of the inverter and consists of a DC/DC converter and a control system (Higueras & Fernández, 2015).

The relationship between the maximum power point (MPP) of a photovoltaic (PV) system and the irradiance and temperature are nonlinear. Additionally, the power-voltage (P-V) curve of the system can exhibit multiple local maxima, especially when there is partial shadowing present. This introduces complexity in accurately determining the precise location of the absolute MPP. Different approaches can be employed to identify this unique point, including mathematical models and search algorithms. In the latter case, the MPPT control system utilizes specific techniques or algorithms to monitor parameters such as voltage and current of the PV generator. By adjusting the settings and duty cycle of the DC/DC converter, the MPPT control system can effectively track and determine the MPP of the PV array. Below are brief explanations of some commonly used MPPT algorithms (Higueras & Fernández, 2015).

2.6.1 Perturb and Observe (P&O) method

P&O is the most often used method for obtaining the MPP since it is easy and simple to implement. This direct method is based on the system being subjected to periodic perturbations, the effects of which are used to calculate the MPP. The algorithm, which modifies the operating voltage of the PV array by a small increment, is what causes these perturbations. The array's PV output power is then compared to the one offered in the previous perturbation cycle to determine the change in output power, ΔP. If the PV array power has increased after the perturbation, that is, if the ΔP is positive, the operation point will get closer to the MPP. By doing this, the array voltage perturbation or change will have the same sign as the previous one. The operating point will have shifted away from the MPP; however, if the array's output power has decreased (the ΔP is negative). In this scenario, the array voltage's next change will have its sign reversed in order to return to the MPP. Until the MPP is identified, this procedure is repeated (Higueras & Fernández, 2015) .

2.6.2 dP/dV or dP/dI feedback control

This approach is the most straightforward method for determining the maximum power point (MPP) as it calculates the rate of change of power with respect to voltage or current (differential power to voltage or differential power to current) along the PV power curve. The MPP is attained when this rate becomes zero. However, due to the nonlinear relationship between power and voltage, there are certain drawbacks to be considered, such as increased complexity, instability, and lack of smoothness (Higueras & Fernández, 2015).

2.6.3 Incremental conductance method

This method relies on the principle that the slope of the photovoltaic (PV) array curve at the maximum power point (MPP) is zero, indicating that the PV array's conductance is equal in magnitude but opposite in sign to its incremental conductance. The incremental conductance (INC) algorithm utilizes this information to determine the direction of voltage perturbation required to reach the MPP. Unlike the perturb and observe (P&O) algorithms, the INC algorithm avoids tracking in the wrong direction during rapidly changing conditions and can accurately detect when the MPP is attained. In an ideal scenario, the algorithm will not oscillate around the MPP once reached, resulting in minimal power loss under steady-state conditions. However, the presence of noise and quantization effects associated with the microcontroller managing the algorithm diminishes this advantage (Higueras & Fernández, 2015).

2.7 Battery Energy Storage

The rechargeable electric battery is a commonly used and widely accepted device for storing electrochemical energy in power systems. It is extensively employed in energy storage systems (ESS) due to its high energy and power density, compact size, and reliable performance. Essentially, a battery consists of electrodes immersed in an electrolyte substance that facilitates the exchange of ions to enable the conduction of electricity. In recent years, there have been continuous advancements in battery technology, focusing on areas such as safety, reliability, performance, efficiency, cost, and capacity. Lead-acid and lithium-ion are the two primary battery technologies utilized in power applications (Keshan, Thornburg, & Ustun, 2016).

The lead-acid battery is an established and cost-effective energy storage device that has been widely used. However, it has limitations in various aspects, including low energy density (50-80 kWh/m3) and power density (90-700 kW/m3), a relatively short lifespan (250-1500 cycles), high maintenance requirements, and the consumption of toxic materials. In contrast, the Li-ion battery offers several advantages such as high energy density (1300-10000 kW/m3) and power density (300-750 kWh/m3), long lifespan (500-10000 cycles), quick response time, low memory effect, and recyclability. Although Li-ion batteries are more expensive compared to lead-acid batteries, they are capable of handling higher C-rates (Gautam , Gautham , & Pavol , 2022).

Nickel iron battery is the longest lasting battery on the market for about 30+ years however, it is the most expensive battery. This battery performs well in cold climates but it does require watering, it is large and heavy in size, and off gasses hydrogen. Figure 2.17 and Table 2.4 shows different battery types and their comparison. (Williams, 2020)

(a)Nickel iron battery (b) Lead-acid battery (c) Lithium-ion battery

Figure 2.17 Different battery types (a) Nickel iron battery (b) Lead-acid battery (c) Lithium-ion battery

Table 2.4: Battery type comparison

Battery Types	Nickel Iron (NiFe)	Lithium Iron ($LiFePO_4$)	Lead-Acid ($PbSO_4$)
Life cycle	11,000 cycles @ 50% DOD	5,000 cycles @ 50% DOD	1,000 cycles @ 50% DOD
	11,000 cycles @ 80% DOD	2,000 cycles @ 80% DOD	200 cycles @ 80% DOD
Application	Off-grid solar and energy preparedness. Tolerant of extremely deep discharges and variable renewable energy charge rates.	Grid-backup, remote telecom, UPS, or off-grid. Lightweight and maintenance free. Can be monitored online	Infrequent use; standby applications like emergency backup. Regular deep discharging limits usable life.
Temperature	-30 to 60 ^{0}C	-20 to 60 ^{0}C	-20 to 50 ^{0}C
Charge/Discharge rate	Prefers medium charge rates between C/2 and C/6	Can be charged and discharged up to C/1	Prefers slow rate, loses capacity linearly with higher rates
Maintenance	Requires regular cell watering. Electrolyte refresh recommended every 10 years.	Require no maintenance, no watering	Flooded type requires regular cell watering and equalization charge
Cost	$1 per usable watt-hour over 30 years life. Higher upfront cost, low total cost.	$1.5 per usable watt-hour over typical 15 years of life. No maintenance reoccurring cost.	$2-5 per usable watt-hour for 5 replacement sets over 30 years. Highest total cost.

2.8 Front-End Converter Control

The electronic management of the power conversion procedure in an AC-to-DC rectifier circuit is referred to as active front-end rectifier control. A power electronic converter called an active front-end rectifier can regulate power flow to the DC bus, providing better power quality and control than a passive rectifier circuit.

In order to maintain high power factor, minimal current distortion, and effective energy transfer, the control mechanism typically involves monitoring the AC input voltage and current waveform. Different techniques, such as digital signal processing and feedback control loops, can be used to provide this control. Effective regulation of the active front-end rectifier can extend system longevity, reduce harmonic distortion, and improve power efficiency.

There are a number of widely used and recognized control methods for front-end rectifiers. Among the well-known control strategies for front end rectifiers are voltage-oriented control (VOC), Direct Power Control (DPC), Model Predictive Control (MPC), and Hysteresis Current Control (HCC). DPC, MPC, and HCC controllers do not require modulators, which lessens the computational load but they have a drawback that they have variable switching frequencies. VOC has a defined switching frequency; therefore. it is simpler to design the filters, calculate losses, and create the cooling system. Additionally, it is a viable alternative for parallel converter systems with carrier interleaving because it uses a carrier-based PWM. Overall, the VOC has the benefit of a constant switching frequency, however a modulator is needed. Control in a synchronous reference frame may make it simpler to track the reference, but it necessitates PLL, which increases the computational load on the controller (Zhaksylyk, et al., 2023). In this thesis VOC is selected for controlling of the front-end converter. Comparison of the front-end rectifier controllers is listed in Table 2.5

Table 2.5: Comparison of Front-end converter control techniques

Parameter	VOC	DPC	OSV-MPC	HCC
PLL require	Yes	Optional	Optional	No
Modulator required	Yes	No	No	No
Switching frequency	Fixed	Variable	Variable	Variable

2.9 Review of Related Literature

In order to research and evaluate solar powered grid-connected electric vehicle charging systems, a literature review was conducted. Different researchers used different approaches to controlling standalone and grid-integrated renewable energy equipment. The paragraphs that follow show some of the papers that have been reviewed and published.

(Biya & Sindhu, 2019) A solar-powered electric vehicle charging station is described in the article "Design and Power Management of a Solar-Powered Electric Vehicle Charging Station with an Energy Storage System". The research proposes an optimal design and power management strategy for the charging station, which utilizes solar photovoltaic (PV) panels and a battery energy storage system (BESS) in conjunction with an AC grid. The study considers the variability of solar power generation and the dynamic charging requirements of electric vehicles. The power flow approach ensures that all electric vehicles connected to the charging station primarily draw power from the solar PV system. The proposed system is developed, designed, and validated using MATLAB Simulink. However, the author could enhance the proposed work by incorporating an optimization technique to reduce the initial investment and operating costs of the charging station.

(Tilahun, 2020) designed a solar power system that can be connected to the grid for the use in railway application of the Ethio-Djibouti Railway Line. The designed PV system generates enough power to run trains while also reducing CO_2 emissions during its lifetime. A boosting converter is used to increase efficiency and perturb and observe MPPT method helps optimize output voltage ranges from 1500-1600 V. The daily energy consumption for the train load obtained were estimated monthly with results showing an annual generation potential of over 10 thousand MWhs annually with payback period of around five years.

(Orhan & Celal, 2021) designed and optimized the wind solar hybrid energy powered charging station via HOMER software for Izmir, Turkey as a case study. The researcher points out Sizing methodology of a solar-wind hybrid EV charging station, and the selection of case site charging station. The investment return period is not mentioned and system synchronization of the hybrid system and energy management system is not well discussed. Additionally, the architecture of the system is not clearly identified weather it is AC based or DC based.

(AlHammadi , et al., 2022) investigated several hybrid renewable energy system configurations for charging electric vehicles in Abu Dhabi, United Arab Emirates. A thorough investigation of earlier methods for charging electric vehicles was done in order to formulate the issue. The authors concluded that, from a technological, economic, and environmental standpoint, the optimum electric vehicle charging model, which comprises solar photovoltaic, wind turbines, batteries, and a distribution grid, was preferable to the other studied configurations. Although the author discussed using a battery as a backup during periods of limited power generation, the backup battery type chosen is lead acid, which has low energy, a short life, and requires frequent maintenance. Different types of EVs are not considered, and with the EV chargers, fast charging is realized.

Table 2.6: List of literatures reviewed with contribution and limitations

References	Contributions	Limitations
Biya, T. S., & Sindhu, M.R., 2019	Solar powered charging station with battery and AC grid Power flow management designed	The investment and running cost of the system not mentioned The charging station power level not specified
Ekren O., Canbaz H., C., Guvel B. C., 2021	HOMER based design and optimization of wind, solar hybrid energy powered charging station Solar and wind sizing methodology pointed out	The system architecture is not clearly identified Investment return period not mentioned
AlHammadi A., Al-Saif N., Al-Sumaiti S A., Marzband M., Alsumaiti T., Forushani H E.,, 2022	The system comprises solar, wind, battery and grid system The energy input and load profile determined Techno-economic analysis performed using HOMER software	The different types of electric vehicles not considered The power output level of the charging station not specified

CHAPTER THREE

3. METHODOLOGY

3.1 Introduction

Data analysis, mathematical modeling, and designs of solar system components, grid integration, and charging components are all covered in this chapter. In MATLAB Simulink, several components of the grid connected solar system, active front end AC-DC converter and isolated LLC resonant DC-DC converter of offboard charger are configured. The identified topologies are subjected to analysis and finally the system is simulated using HOMER and MATLAB Simulink programs.

3.2 Materials

Softwares like MATLAB/2021a, HOMER Grid 1.9.6 Evaluation Edition, Microsoft Office 2019, and MathType 7.0 are used in this thesis. The computer program known as MATLAB includes Simulink® and technical toolboxes. Cost optimization and sensitivity analysis are performed using HOMER. Editing of the thesis documentation is done using Microsoft Office. For writing mathematical equations and formulas in Microsoft Office word processing and PowerPoint presentation software, MathType 7.0 is used.

3.3 Methods

To examine the precise goals of the suggested system, the procedure listed below is employed. The evaluation process begins with problem identification and creating a theoretical background by reviewing a closely related works. The required data is then gathered for this study. The Eastern and Central Oromia Meteorology Service Center, which uses the site's latitude and longitude for minimum and maximum temperatures, and solar sunshine hour, and the Adama City Chamber of Trade, for yearly fuel consumption analysis of Adama city, are the different organizations and agencies that directly collect the data used in the design of the solar components. The gathered data are examined in order to comprehend and create system modeling. A model for the offboard charging system and solar components is created. The system is then simulated using MATLAB/Simulink® and HOMER software. The simulation's output is then analyzed and discussed. The following flow chart of Figure 3.1 can be used to summarize the method used while conducting the thesis.

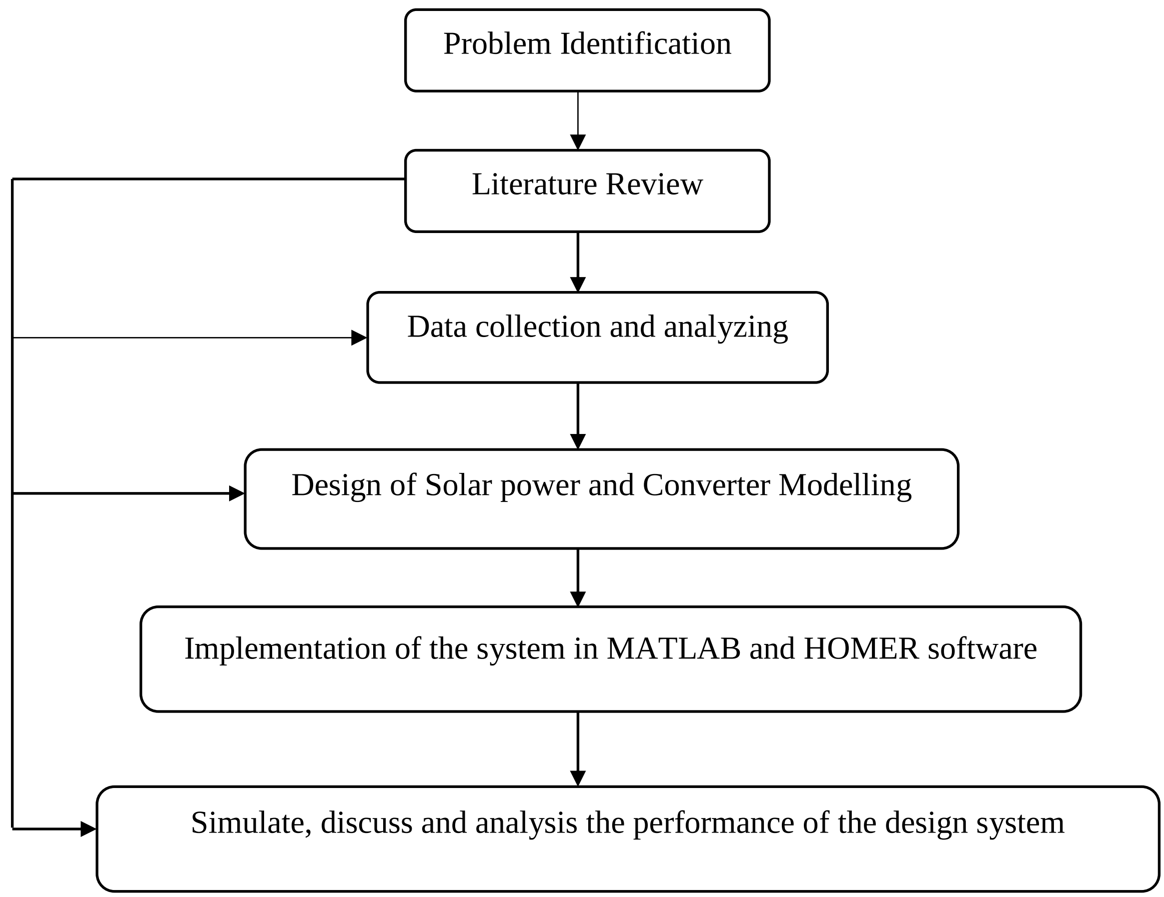

Figure 3.1: Research methodology block diagram

3.4 Block Diagram of the Proposed Charging System

A grid-connected boost converter is a popular front-end PFC with voltage-oriented control interfaces due to its simple structure, high THD reduction performance, and unity power factor operation capability (Zhaksylyk, et al., 2023). In the DC/DC isolation point, the resonant converter can operate over a wide load range with good voltage regulation performance at light loads and no diode reverse recovery loss, zero voltage switching (ZVS) operation at different load condition, and have only capacitor component as the output filter, thus suitable for high voltage and high power EV charging applications as compared with traditional LC filters (Panda & Rout, 2016).

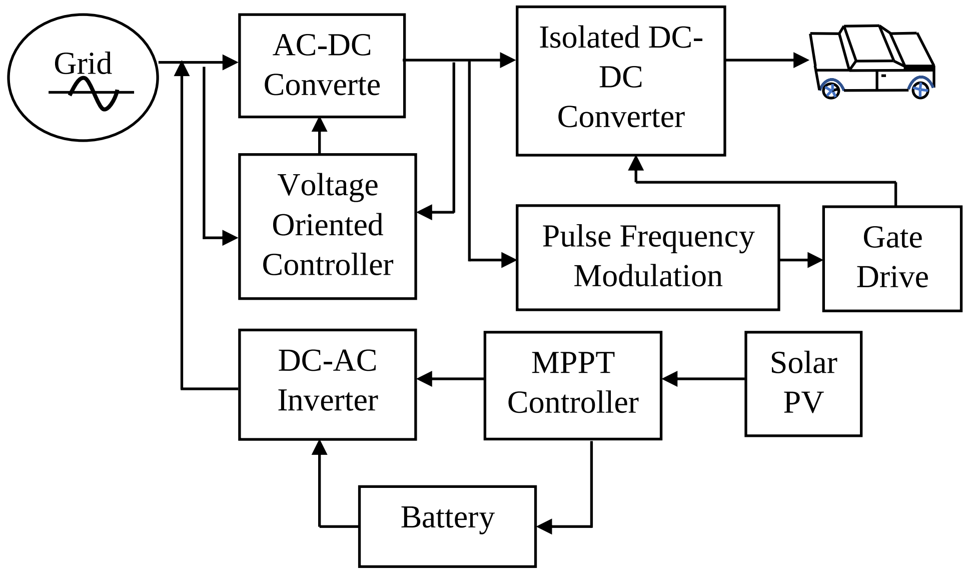

Figure 3.2: Block diagram of general system architecture

In this thesis, an off-board EV charging topology is modeled consisting of a grid-tied PV system with MPPT operation as shown in Figure 3.2. The solar system is connected with the grid through a controlled inverter circuit. The system consists of a front-end ac/dc converter used for rectification at unity power factor, and back-end dc/dc converter is responsible for providing galvanic isolation. The proposed charging design is optimized for a wide voltage range of (200V to 450V). In addition, the optimal design of the system to achieve better performance with maximum overall efficiency is well stated.

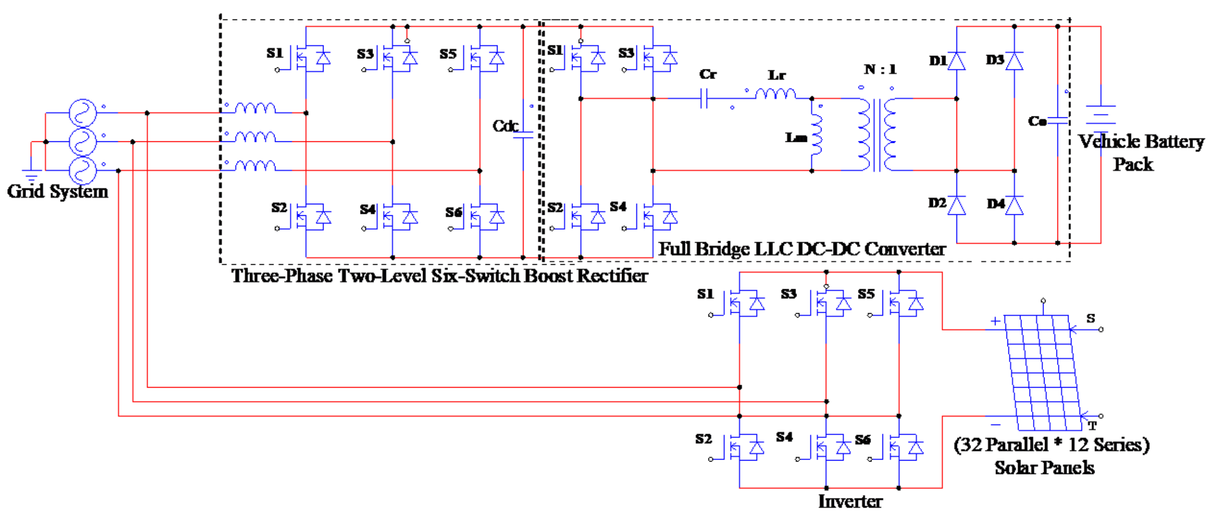

Figure 3.3: Schematic diagram of the proposed dc fast charger

3.5 Data Gathering and Analysis

The data collected from the vehicle selling company which is the energy capacity of the electric vehicles is the load to be considered during the design process. The capacity and cost of the solar system components are greatly influenced by the size of the electric loads. Properly analyzing load profile is an important initial point to design a solar power generation system. There are electric vehicles with a battery capacity available in Ethiopia is tens of kWh in the case of plugin electric vehicle that can be charged with DC fast charging. It is presented in Table 3.1

Table 3.1: Electric vehicles type with battery energy capacity and electric range

(greentecafrica, 2023) (marathoncars, 2023)

Electric Vehicle Type	Battery Energy (kWh)	Electric Range (km)	Charging power (kW)	Charging duration
Hyundai Ioniq 5	58	266	40	50min
Hyundai Kona Electric	64	258	49	63 min
Ford Mustang Mach-e	91	312	48	86 min
Kia Ev6 Wind Awd	77.4	282	50	65 min
Volkswagen ID4 Pro S	82	268	47	72 min
Volvo C40 Recharge	78	420	50	62 min
KAS-Anna 360	26.8	187.03	-	45-50 min

3.5.1 Analysis of Solar Radiation Data of Adama City

For a PV system solar radiation availability analysis is very significant at all in the design of input variables. Solar radiation data are accessible in various forms for a different purpose. The sum of beam or direct normal irradiance, diffuse horizontal irradiance and ground reflected radiation gives the total solar radiation on horizontal earth surface measured in w/m^2. The integrated value of irradiance over some period of time is known as irradiation usually stated per hour or day. Sun-hour is 1000 watts of energy shining on 1 square meter of surface for 1 hour. A 15 years solar sunshine hour measured data for Adama city is gathered from Ethiopian national metrology as shown in Table 3.2

Table 3.2: Solar sunshine hour data of Adama city

Month	Jan	Feb	Mar	Apr	May	June	July	Aug	Sep	Oct	Nov	Dec	Ave
Sunshine Hours (hour)	6.02	6.0	5.3	5.5	6.1	6.7	4.7	4.9	5.9	8.7	6.6	7.8	6.2

The lowest recorded monthly average solar radiation is on July thus, the solar photovoltaic panel is designed using month having the lowest sunshine hour. The collected 15 years recorded sunshine hour, monthly average minimum and maximum temperature data is available in Appendix A.

3.6 Electric Vehicle Load Estimation

Electric vehicles are considered as a traction load consisting of a battery called traction battery or a rechargeable battery which is used to power electric motor inside the battery electric vehicle (BEV) and hybrid electric vehicle (HEV). Therefore, the electric load considered for an EVs is its battery capacity.

Factors to be considered while determining the number of Electric Vehicles charged per day by a DC fast charging (DCFC) station are:

- The charging power rating of the DCFC station: The selected charging power rating is a 50kW DCFC considering its cost effectiveness, compatibility and grid limitation.
- Battery capacity: The average battery capacity of the Electric Vehicles is 71.3 kWh. The larger the battery capacity of the electric vehicles, the longer the charging time required, and hence, the lower the number of electric vehicles that can be charged per day.
- Charging Duration: A 12-hour operation of the charging station per day is considered for this work starting from 06:00 AM to 20:00 PM.

According to International Energy Agency (IEA) report the average total number of electric Light duty vehicles (LDV) per charging point in 2022 is about ten (IEA, 2023)

To determine the number of electric vehicles that can be charged per day by a DCFC station:

$$\text{Number of EV charged per day} = \frac{H \times P}{E_{avg}} \tag{3.1}$$

Where; H is Operating hours per day (hr), P is maximum charging power of the station (kW), E_{avg} is average energy consumption of EV (kWh)

$$\text{Number of EV charged per day} = \frac{12hr \times 50kW}{71.3kWh} = 8.41$$

Therefore, this DCFC station can charge a minimum of 8 electric vehicles per day.

The total energy consumption will be:

$$\text{Total Daily Energy Required} = 8 \times 71.3kWh = 570.4 \, {}^{kWh}\!/_{day}$$

The total energy is taken as a daily energy demand by considering the incoming electric vehicles with the average battery capacity, which is 71.3 kWh.

3.7 Sizing of solar (PV) system

System sizing is the procedure of estimating suitable voltage and current ratings for each component of the photovoltaic system to meet the electric demand of the electric vehicles. Using the available sunshine hour, the ambient temperature and PV module data, the power output of the PV system is obtained.

$$E_{Daily\ Load}(kWh) = \frac{Daily\ Energy\ \mathrm{Re}quired(Wh)}{\eta_{Inverter} \times \eta_{Disch\arg ing} \times \eta_{Ch\arg ing} \times \eta_{Solar\ Panel} \times 1000} \tag{3.2}$$

$$E_{Daily\ Load}(kWh) = 684.264\ kWh$$

The minimum average daily peak sun hour is 4.7, The total installed PV capacity is calculated in Equation 3.3.

$$Installed\ PV\ Capacity\ (kW) = \frac{E_{Daily\ Load}(kWh)}{Daily\ Peak\ Sun\ Hours\ (h)} \tag{3.3}$$

$$= \frac{684.264\ kWh}{4.7\ h} = 145.588\ kW$$

The selected solar module for the system is a 305 W monocrystalline type which has the following specifications listed in Table 3.3.

Table 3.3: Electrical specifications of PV panel

Model	LR6-60HOH-305M
Maximum power (W)	305 W
Voltage at maximum power (Vmp /V)	33.1
Current (Imp) at maximum power (Imp /A)	9.21
Open circuit voltage (Voc/V)	40.1 V
Short circuit current (Isc)	9.78A
Temperature coefficients of Voc	-0.286%/C
Temperature coefficients of Isc	0.057%C
Temperature coefficients of Pmax	-0. 370 %

Form the total Load which is covered by the solar system the number of modules required per string will be:

$$FF = \frac{Maximum\ power\ from\ solar\ \text{mod}ule}{Isc * Voc} \tag{3.4}$$

$$FF = \frac{305W}{9.78A \times 40.1V} = 0.78$$

$$PV\ array\ (kW) = fill\ factor \times Installed\ PV\ Capacity\ (kW) \tag{3.5}$$

$$PV\ array\ (kW) = 0.78 * 145.588\ kW$$

$$= 113.56\ kW$$

The required number of PV is calculated in Equation 3.6

$$N_m = \frac{PV\ array\ (kW)}{P_{mpp}} \tag{3.6}$$

$$N_m = \frac{113.56\ kW}{305W} = 372.32$$

Approximately = 373

Modules per string can be obtained using Equation 3.7

$$N_s = \frac{N_m}{V_{mpp}} \tag{3.7}$$

$$N_s = \frac{373}{33.1V} = 11.269$$

By rounding to the next whole number = 12

$$N_p = \frac{N_m}{N_s} = \frac{373}{12} = 31.08 \tag{3.8}$$

By rounding to the next whole number = 32

The total number of modules is: $N_p \times N_s = 32 * 12 = 384$

3.7.1 Inverter Sizing

The Inverter should be sized 20-30% bigger than the total watts of the appliance (Cronemberger, Martin, & Sanchez, 2012). Considering 25%, the total watt power becomes:

$$113.56\,kW + 25\% \times 113.56\,kW = 141.95\,kW$$

From the standard 150kW by 380V is selected.

3.7.2 Battery Energy Storage System (BESS) Sizing

Energy production from PV during night time is not possible due to lack of irradiance and it is less in rainy season. To overcome this lack battery energy storage system is designed for the electric vehicle charging. The Energy consumption of the station is 570.4 kWh/day. For grid connected system, the number of days of autonomy is the duration during which the system must power the load in the event of a grid outage. The number of days of autonomy in this thesis is 0.25. Inverter efficiency is 0.963 and discharging efficiency is 0.92.

EnerDel Secure plus 600V, 168Ah, Nominal capacity 101 kWh Lithium ion battery is selected for the design considering cost and efficiency. Considering depth of discharge (DOD) of lithium ion battery 0.8, the battery capacity becomes;

$$\text{Battery Size } (kWh) = \frac{\text{Days of Autonomy} \times \text{Daily Energy Required } (Wh)}{\text{DoD } (\%) \times \eta_{Inverter} \times \eta_{\text{Discharging}} \times 1000} \quad (3.9)$$

$$= 201.194\ kWh$$

The ampere-hour specification is expressed in Equation 3.10

$$Battery\ Size\ (Ah) = \frac{Battery\ Size\ (kWh) \times 1000}{Nominal\ Battery\ Voltage\ (V)} \quad (3.10)$$

$$= \frac{201.194\ kWh}{600\ V} = 335.3233\ Ah$$

The number of batteries connected in parallel (B_p) and series (B_s) will be:

$$B_p = \frac{Battery\ Size\ (Ah)}{B_c} \quad (3.11)$$

$$B_p = \frac{335.3233\ Ah}{168Ah}$$

$$B_p = 1.9959 \approx 2$$

$$B_s = \frac{600V}{600V} = 1$$

Total number of batteries $= 2 \times 1 = 2$

3.7.3 Charge Controller

Charge controllers reduces electrolyte loss, stop over discharge, and prevent overcharging. In addition, more battery life and reduced maintenance will be achieved. Modern engineering has been blended with simple modular design to produce a system that performs better and has more features than any other regulator in its class. The ability to adjust any control level can be managed by remote control (M. A. Laguado-Serrano1, 2019).

For the reasons stated above, 48V and 80A have been chosen as the system charge controller. The ISC (short circuit current) of a selected PV module times the number of modules in parallel

The total current of the charge controller is:

$$\text{Charge controller,} \left(I_{tot}\right) = I_{SC} \times N_P \times \text{oversize factor} \quad (3.12)$$

$$\text{Charge controller}, (I_{tot}) = 9.78A * 33 * 1.25$$

$$I_{tot} = 403.425A \simeq 404A$$

$$\text{Number of charge controller} = \frac{\text{Total Current}}{\text{Selected Charge Controller}} \tag{3.13}$$

$$\text{Number of charge controller} = \frac{404A}{80A} = 5.05$$

$$\approx 5$$

3.7.4 Total Area Covered by Solar Panel

Considering the solar panel width and length:

L = 1683 mm, W = 996 mm

$$A = L \times W \tag{3.14}$$

$$A = (1683mm \times 32) \times (996mm \times 12)$$

$$A = 643,686,912\ mm^2 = 643.686912\ m^2$$

The selected site has enough landscape area for the installation of the solar panels with 643.686912-meter square size.

3.8 Modelling of converter

To provide power for electric vehicles through a DC distribution system, a DC voltage level ranging from 200V to 450V is chosen according to the standards set by IEC and SAE, as well as the battery capacity of the vehicles. The output of the PV panel fluctuates continuously with changes in irradiance. The load voltage also varies depending on the traction load. During night time, when there is no sunlight and grid disruption, electric vehicles are powered by a battery energy storage system. During other times when there is excess power generated by the PV panels while meeting the load demands, the battery energy storage system is charged using solar energy.

3.8.1 Full Bridge LLC Resonant Converter Design

Based on the dc voltage and current characteristics of the LLC resonant converter, the dc-dc converter parameters can be designed. (200-450) V is the output voltage, and the input voltage ranges from (580-600) V. Lower resonance frequencies frequently increase efficiency and reduce switching losses at higher power levels. In general, reduced component sizes are achieved at higher frequencies, although switching losses may also increase. such that, 100 kHz is chosen as the resonance frequency in this thesis.

I. Calculating the transformer turn ratio, the minimum and maximum voltage gains of the resonant tank

The nominal voltage gain, $M_{nom} = 1$

$$N = \frac{N_p}{N_s} = \frac{V_{in\_nom}}{V_{out}} * M_{nom} = 1.333 \tag{3.11}$$

$$M_{\max} = \frac{V_{in\_nom}}{V_{in\_\min}} * M_{nom} = 1 \tag{3.12}$$

$$M_{\min} = \frac{V_{in\_nom}}{V_{in\_\max}} * M_{nom} = 0.967 \tag{3.13}$$

II. Selecting $Q_{\max}$ value

Depending on the load current, quality factor changes. Higher Q values are used in heavy load situations, whilst lower Q values are used for smaller loads. The $Q_{\max}$ value necessary for the maximum load point must be set. Let $Q_{\max}$ =0.3

III. Selecting m value

Reducing the values of m can result in increased boost gain and a narrower frequency modulation range, providing greater flexibility for control and regulation. This is particularly beneficial in applications with wide input voltage ranges. However, when m is low while maintaining the same quality factor and resonant frequency, it leads to a smaller magnetizing inductance. Consequently, this results in higher peak-to-peak current ripple in the magnetizing circuit, leading to increased circulating energy and conduction losses. Let $m = 10$

IV. Voltage Gain Specification

The maximum quality actor at minimum input voltage $Q_{\max@V\min}$ value must be determined in the case of the lowest input voltage because the power is derated at lower input voltages. Keep in mind that the I-V characteristics of solar panels are related to this power derating standard.

$$Q_{\max@V\min} = Q_{\max} * \frac{V_{in\_\min}}{V_{in\_\max}} = 0.29 \tag{3.14}$$

Where, $V_{in\_\min}$ is the minimum input voltage and $V_{in\_\max}$ is the maximum input voltage

The maximum gain at $Q_{\max@V\min}$ can be obtained by solving Equation 3.15 in chapter two:

$$K_{\max} = K(Q_{\max@V\min}, m, F_{x\min}) = 3.448 \tag{3.15}$$

Hence, $K_{\max}$ is greater than $M_{\max}$, there is no need to adjust the m value.

V. Minimum Switching Frequency Calculation

$$F_{s\_\min} = F_{X\min} * f_r = 50kHz \tag{3.16}$$

VI. Determining Value of Resonant Components

At maximum load, the reflected load resistance $R_{ac\_\min}$ is,

$$R_{ac\_\min} = 5.842\Omega$$

The resonant tank component values are:

$$Q_{\max} = 0.3 = \frac{\sqrt{L_r / C_r}}{5.842}, L_r = 3.0716C_r \tag{3.17}$$

$$fr = 100kHz = \frac{1}{2\pi\sqrt{3.0716C_r^{\,2}}} \tag{3.18}$$

$$m = 10 = \frac{L_r + L_m}{L_r} \tag{3.19}$$

Therefore, $C_r = 908.6e^{-9}F, L_r = 2.789e^{-6}H, L_m = 25.101e^{-6}H$

Table 3.4 shows the list of variables that were taken into consideration when designing the full-bridge LLC resonant converter.

Table 3.4: List of full-bridge LLC resonant converter components

Component	Symbol	Value
DC Link Voltage	Vdc	600V
Resonant Frequency	Fr	100 kHz
Transformer turn ratio	N	1.333
Resonant capacitor	Cr	908.6nF
Resonant inductor	L_r	2.789 µH
Magnetizing inductor	L_m	25.101 µH
Output capacitor	C_o	2.9629 nF
Rated Maximum Power	P_{max}	50kW

3.9 Grid Synchronization

Grid synchronization is vital in grid-connected applications like renewable energy systems or electric car chargers to make sure that the power generated or consumed is in sync with the grid and satisfies the necessary requirements of power quality. In order to achieve grid synchronization, a phase-locked loop (PLL) is used in this thesis.

3.9.1 Phase Locked Loop Control

The synchronously rotating reference frame (dq-frame) will be utilized as the control in this model to convert the voltage and current quantities from the natural reference frame (*abc*-frame) to the synchronously rotating reference frame (dq-frame). (Zunaib , et al., 2018)

Clarke Transformation

A two-phase orthogonal system is created from a three phase abc signal in a stationary reference frame known as the "$\alpha\beta$". The benefit of using a smaller quantity of signals compared to the original number makes this transformation popular in the analysis of electrical machines and the regulation of power electronic converters. The following matrix gives the transition from the original reference frame (abc) to the fixed reference frame ($\alpha\beta$).

$$\begin{bmatrix} i_\alpha \\ i_\beta \end{bmatrix} = \frac{2}{3}\begin{bmatrix} 1 & -\frac{1}{2} & -\frac{1}{2} \\ 0 & \frac{\sqrt{3}}{2} & -\frac{\sqrt{3}}{2} \end{bmatrix} \times \begin{bmatrix} i_a \\ i_b \\ i_c \end{bmatrix} \tag{3.20}$$

The $\alpha\beta$ components of the voltages can be calculated from line to line voltages using Equation 3.21

$$\begin{bmatrix} v_\alpha \\ v_\beta \end{bmatrix} = \frac{2}{3}\begin{bmatrix} 1 & -\frac{1}{2} & -\frac{1}{2} \\ 0 & \frac{\sqrt{3}}{2} & -\frac{\sqrt{3}}{2} \end{bmatrix} \times \begin{bmatrix} v_a \\ v_b \\ v_c \end{bmatrix} \tag{3.21}$$

Any space phasor that represents a three-phase balanced system has an amplitude that is equivalent to the amplitude of a two-phase system due to the factor 2/3 in Equation 3.20 and 3.21

Parke Transformation

By employing the Park transformation, the original reference frame is converted into the synchronous reference frame. To determine the phase of the input voltages, the q-component of the positive sequence voltage closely follows a zero-reference using a PI controller. The conversion from the initial frame to the new current and voltage frame can be mathematically expressed as follows.

$$\begin{bmatrix} i_d \\ i_q \end{bmatrix} = \frac{2}{3}\begin{bmatrix} \cos\omega t & \cos\left(\omega t - \frac{2\pi}{3}\right) & \cos\left(\omega t + \frac{2\pi}{3}\right) \\ -\sin\omega t & -\sin\left(\omega t - \frac{2\pi}{3}\right) & -\sin\left(\omega t + \frac{2\pi}{3}\right) \end{bmatrix} \times \begin{bmatrix} i_a \\ i_b \\ i_c \end{bmatrix} \tag{3.22}$$

$$\begin{bmatrix} v_d \\ v_q \end{bmatrix} = \frac{2}{3}\begin{bmatrix} \cos\omega t & \cos\left(\omega t - \frac{2\pi}{3}\right) & \cos\left(\omega t + \frac{2\pi}{3}\right) \\ -\sin\omega t & -\sin\left(\omega t - \frac{2\pi}{3}\right) & -\sin\left(\omega t + \frac{2\pi}{3}\right) \end{bmatrix} \times \begin{bmatrix} v_a \\ v_b \\ v_c \end{bmatrix} \tag{3.23}$$

3.9.2 Inverter Controller Design

Phase-Locked Loop (PLL) control is used as shown in Figure 3.4, to synchronize the inverter output voltage with the grid voltage to ensure that the inverter output is in phase with the grid.

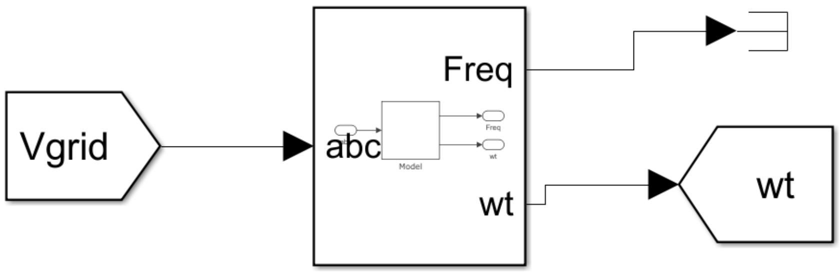

Figure 3.4: Three phase phase-locked loop controller

The proportional-integral (PI) controller, as shown in Figure 3.5, offers feedback to modify the inverter output current in accordance with the difference between the desired and actual current levels. The park transformation is used to bring the current into *dq* frame and control the current's peak value. The reference current for the MPPT output is contrasted with it. The reactive power output of inverters is controlled by the *Iq*. The PWM controller adjusts the duty cycle of the inverter's output waveform, to regulate voltage and current values. 5 KH is the switching frequency.

Table 3.5: PI setting of inverter controller

Controller type	K_p	K_i
PI	0.05	1
PI	0.01	1

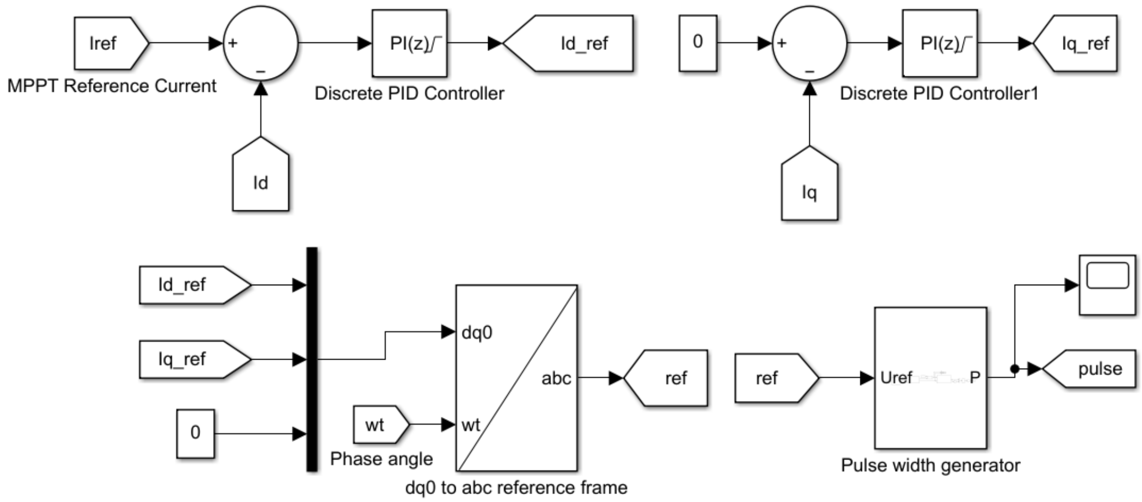

Figure 3.5: Inverter current and reactive power controller

3.9.3 Rectifier Voltage Oriented Control

Several articles select 700 V of DC link voltage (V_{DC}) for the front-end AC/DC converter (Zhaksylyk, et al., 2023) (Friedli, Hartmann, & Kolar, 2013). In this thesis a universal bridge rectifier is used with output voltage of 600V. This is due to the good power factor correction and low percentage of total harmonic distortion at V_{DC} = 600V.

In Clarke's transformation, the voltages in three-phase are transformed into the 'ab' domain. Then, apply Park's transformation from ab to dq0 using an approximated angle q. This is the PLL's Phase Detector (PD) stage (Golestan & Vasquez, 2016). After passing through the PI controller, which serves as a Loop Filter (LF), the voltage's q-axis component is used to determine the frequency. This frequency is employed by the following stage's voltage-controlled oscillator (VCO) to estimate the phase angle (Zhaksylyk, et al., 2023).

Cascaded control loops are used in the VOC of an AFE rectifier. Figure 3.6 illustrates how the proportional-integral (PI) controller is used in the outer control loop to regulate the DC link voltage. The DC current necessary to maintain the appropriate level of DC link voltage is represented by the PI's output. A power balance equation can be used to convert this DC current into the corresponding current reference for the d-axis, *id.*

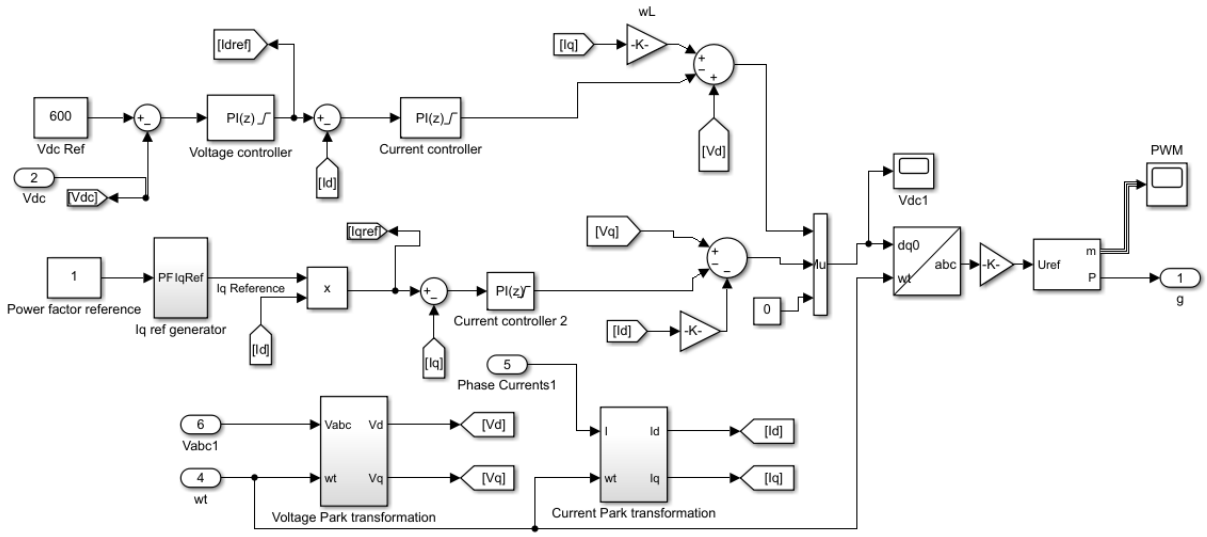

Figure 3.6: Voltage oriented control of front-end rectifier

3.10 Input data to the Homer Software

One of the most crucial components in the production of energy is the resource. The grid system is largely dependent on the production, transmission, and distribution of electric power, while the solar resource is extremely dependent on latitude and temperature. A renewable resource may also exhibit substantial seasonal and hour-to-hour variations at any given location. The activities and economics of renewable power systems are influenced by the renewable energy sources that are available. As a result, careful modeling of renewable assets is a necessary gadget modification issue.

HOMER Grid has the capability to simulate On-Demand Electric Vehicle (EV) Charging, which emulates a rapid charging station.

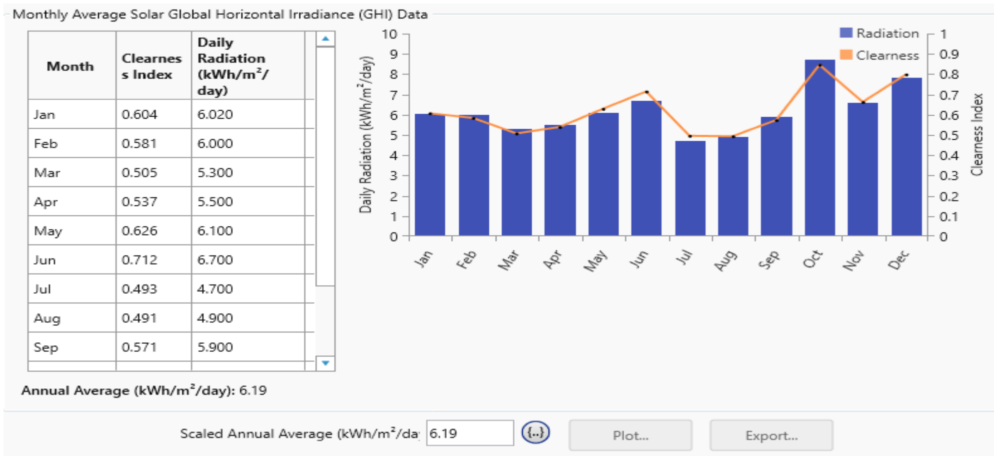

Figure 3.7: Solar data resource

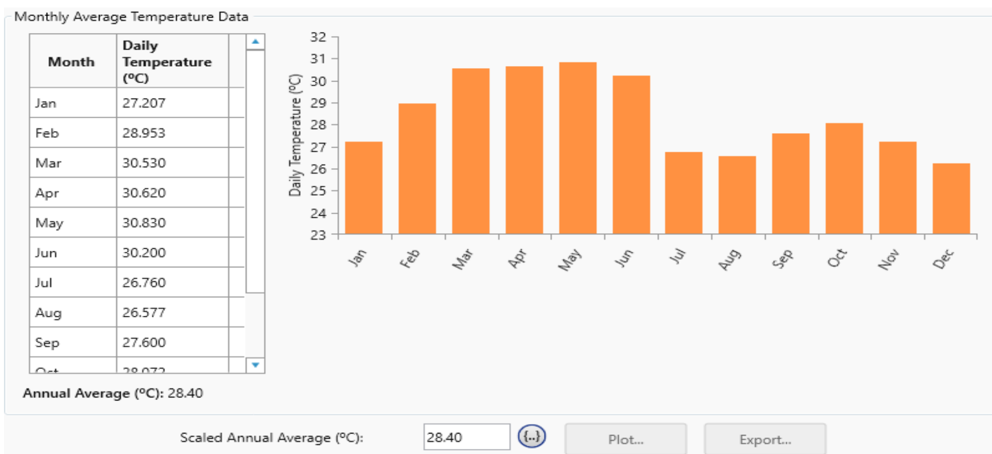

Figure 3.8: Temperature data resource

HOMER can be used to model electric vehicle loads which is an electrical demand categorized as a traction load to be served according to a given timetable. The load profile typically includes information such as charging power levels, charging durations, and the time of day when charging occurs. Users can input these parameters to represent the behavior of EVs within the system accurately. HOMER software supports the modeling and analysis of Electric Vehicles (EVs) as a load in energy systems

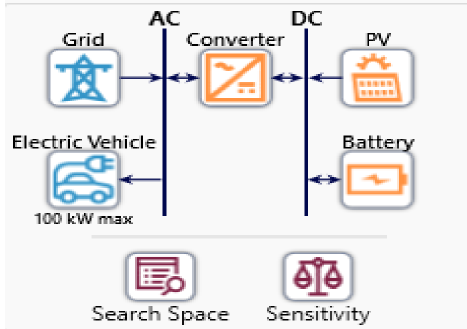

Figure 3.9: Schematic configuration of grid connected solar powered EV charging model

The system's schematic diagram includes the Solar Panel, Converter, Battery, Electric vehicle and Grid power System. The hybrid models are designed to configure a solar system, which incorporates a Grid connection to supply energy for Electric Vehicle (EV) battery.

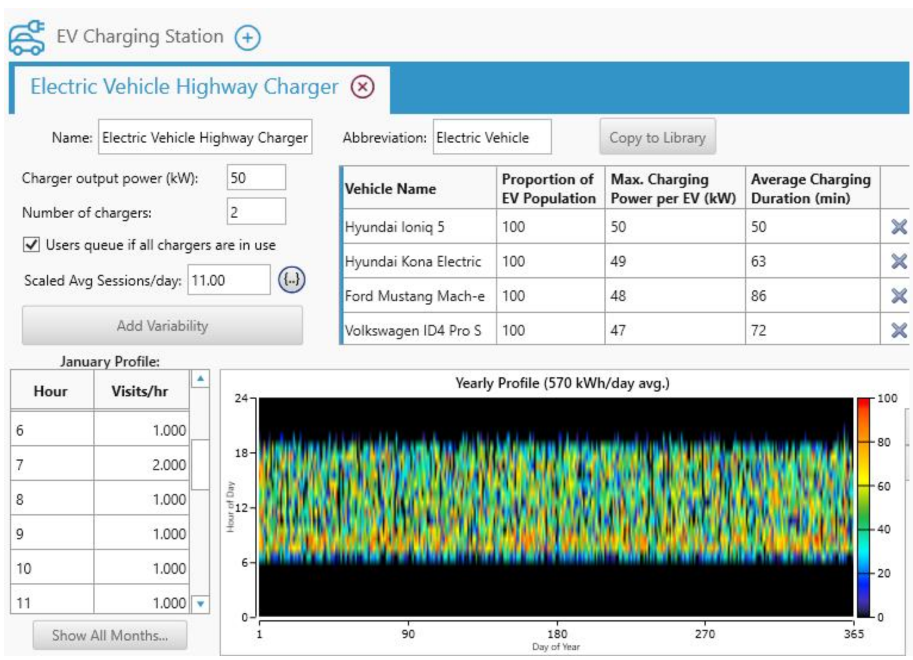

Figure 3.10: Daily EV load Profile

Figure 3.10 depicts EV load consisting of a battery called traction battery or a rechargeable battery which is found inside an Electric Vehicle. Each electric vehicle has the data of maximum charging power in kW with the average charging duration in minute. The electric vehicle charging station is a highway DCFC charger with the maximum output power of 50 kW. The average number of vehicles charging sessions per day is 11 and the number of chargers at the charging station is 2.

CHAPTER FOUR

4 RESULT ANALYSIS AND DISCCUSIONS

4.1 Result Analysis

In this chapter the proposed Solar PV system, active front end rectifier, and LLC resonant converter-based offboard electric car battery charger results and analyses are included. The simulation results presented in this chapter are equivalent to those utilized in the study in terms of value. In this study, the overall charger and cost optimization are modeled using the commercial software HOMER and the MATLAB/Simulink. The active front end converter's simulation result on the charger primarily demonstrates how the converter maintains harmonics and power factor when charging the electric vehicle's high voltage battery. Results pertaining to the charging station's cost optimization is also demonstrated. Lastly, other related simulation findings are addressed.

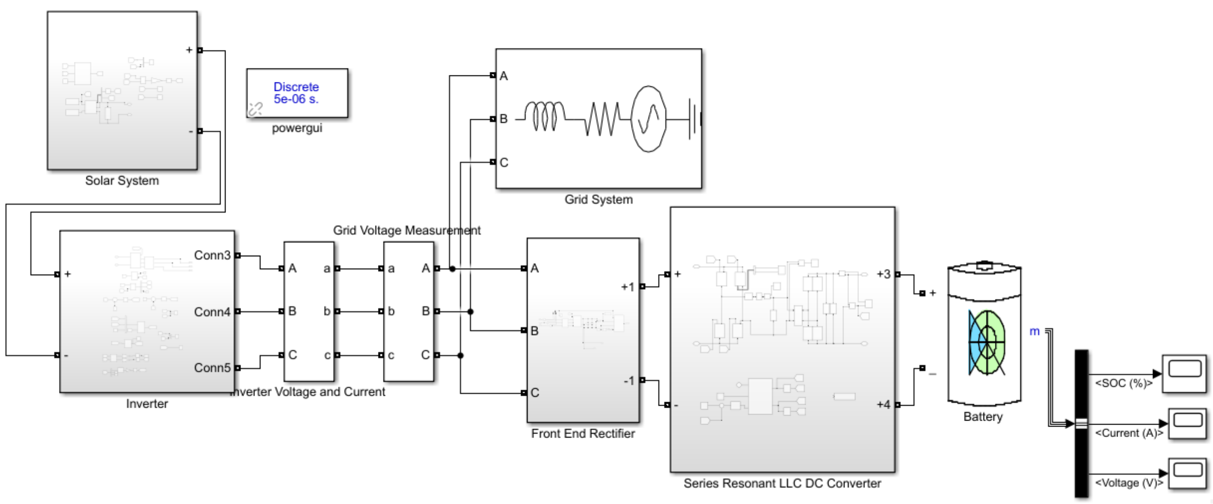

Figure 4.1: Overall hybrid system model

4.2 The Proposed Electric Vehicle Charging Station MATLAB Simulink Result

The MATLAB software provides a Simulink environment for modeling, simulating, and analyzing dynamic systems. The comprehensive system comprises a photovoltaic (PV) system with maximum power point tracking (MPPT) functionality, a grid system, and a converter. To manage these components, a PID controller is implemented. Additionally, individual controllers are employed to extract the maximum voltage output from the hybrid system.

4.2.1 Solar PV System Result

The model showing the solar configuration with MPPT tracking, inverter, and grid system with an output power level of ($113.56*10^3$W). The photovoltaic array containing a connection of 32 solar panels parallel and 12 series in grid connected system to satisfy the estimated load in charging of electric vehicle battery.

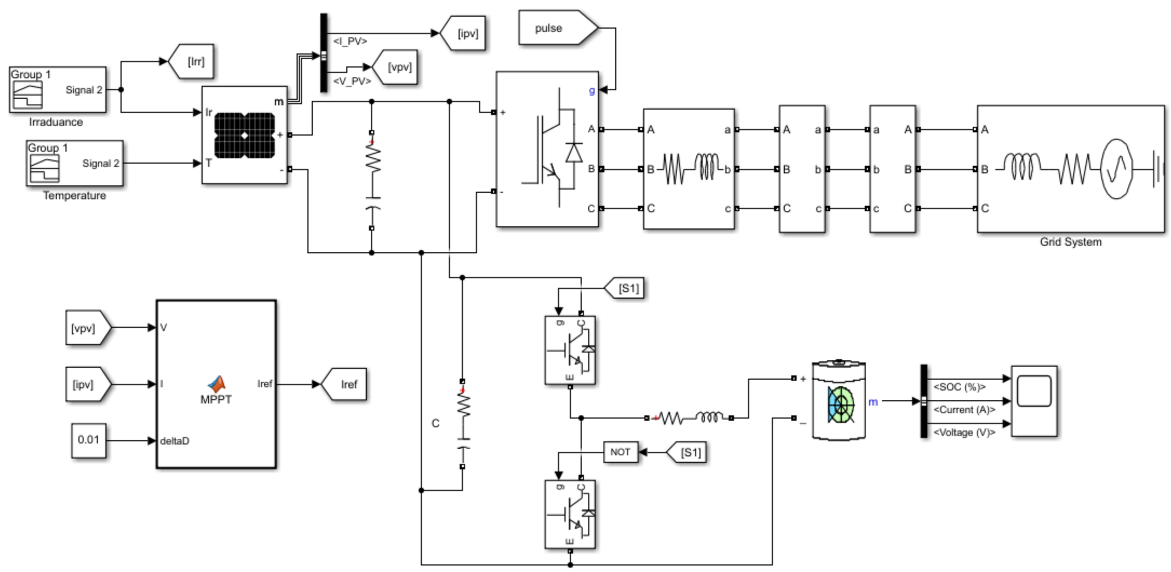

Figure 4.2: Solar system with inverter and grid network

The inverter output waveform in Figure 4.3 shows (y-axis) voltage and current. (x-axis) is plotted against time with Vmax 380.1 to -380.1 Vmin, frequency 50 Hz, time duration (period) 20 ms, rise time 5.820 ms, fall time 5.821 ms. etc. is shown at a duty cycle of 50% with positivevalues preshoot 0.505%, overshoot 0.505%, and undershoot 1.963%. It is also shown for a dutycycle of 50% with a negative preshoot of 0.505%, an overshoot of 1.964% and an undershoot of 0.505%.

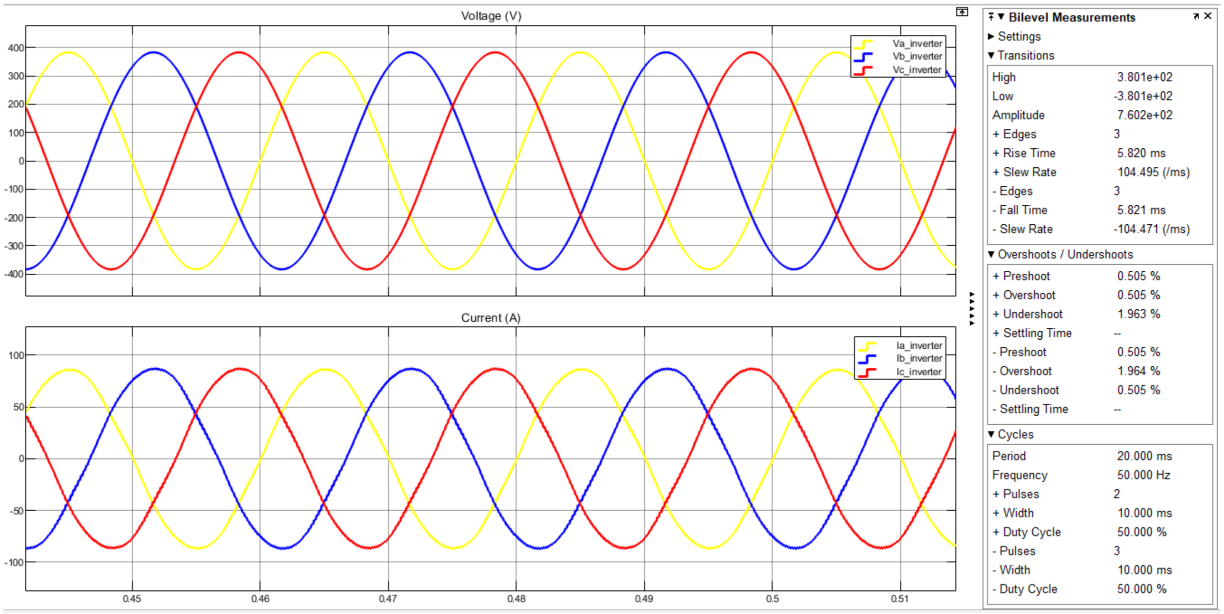

Figure 4.3: Solar system output after inverter

4.2.2 Front-End Boost Converter Result

The waveforms and outcomes derived from the initial stage active boost converter are displayed in Figures 4.4 to 4.6. Figure 4.4 exhibits the voltage and current waveforms on the input side for a single phase. This waveform emphasizes that the input current waveform aligns with the input phase voltages, leading to a power factor of unity at the input and a remarkably smooth power transmission, as illustrated in Figure 4.5.

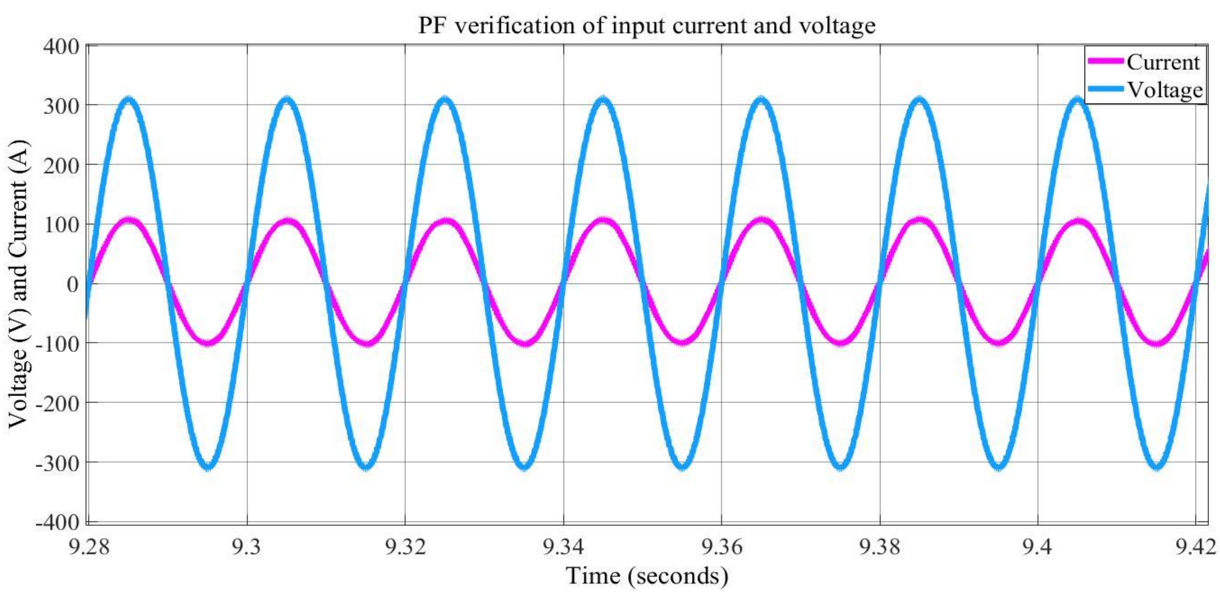

Figure 4.4: Active frontend rectifier input voltage and current

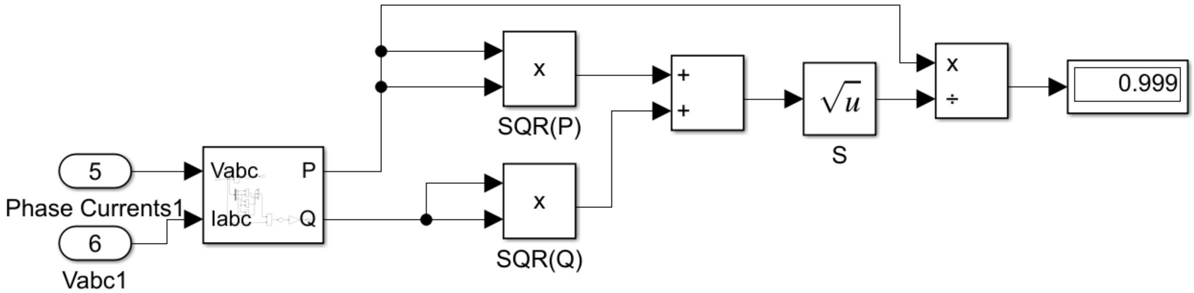

Figure 4.5: Power factor of the system

According to Figure 4.6, the output voltage of the front-end converter is maintained 600V to have better inductor current cancelation and reduced ripple current in the circuit.

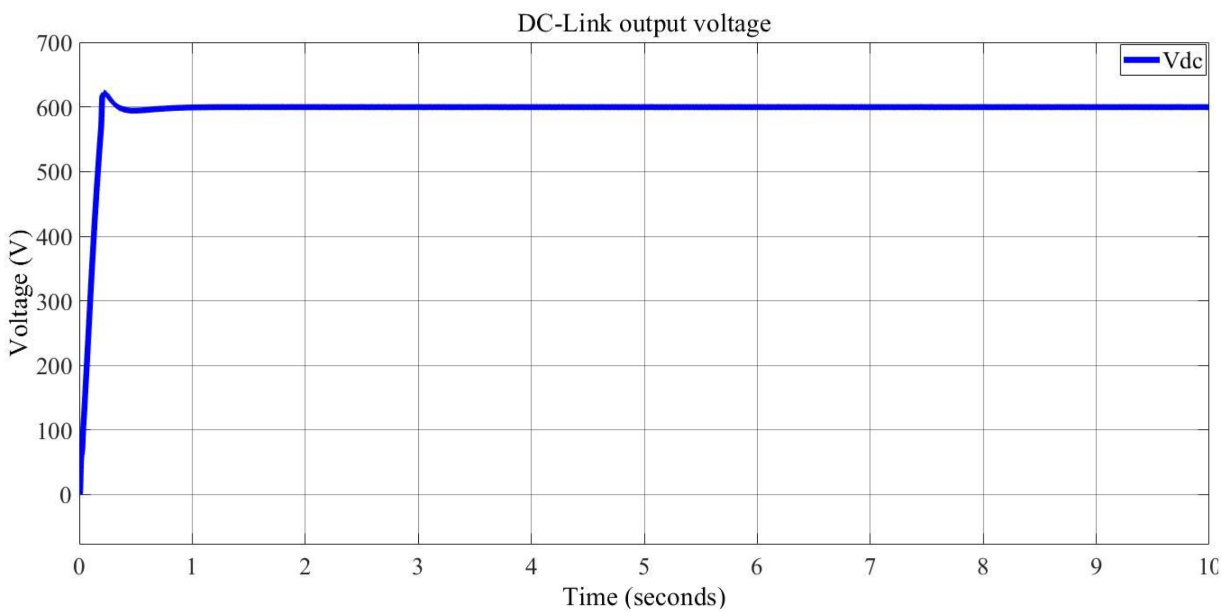

Figure 4.6: Output voltage of front-end rectifier

In the modelling of a charging system, it is important to consider the total harmonic distortion (THD), which measures the impact of noise on the fundamental input current. The IEEE std 519-2014 provides recommended values for acceptable harmonic distortion, with 5% being the recommended threshold. In the specific case of the modelled electric vehicle charger, careful consideration was given to minimize harmonics. Through the implementation of appropriate measures, a harmonics level of 2.8% was achieved, as depicted in Figure 4.7. This indicates that the modelled charging system successfully meets the recommended standards for acceptable harmonic distortion, ensuring efficient and reliable operation.

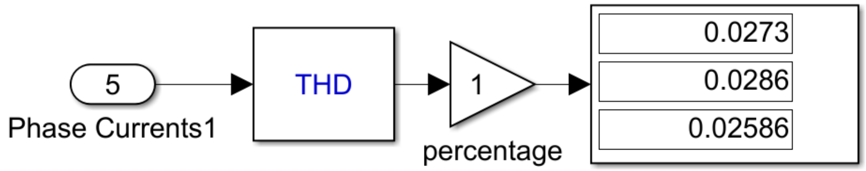

Figure 4.7: Total harmonic distortion of phase current

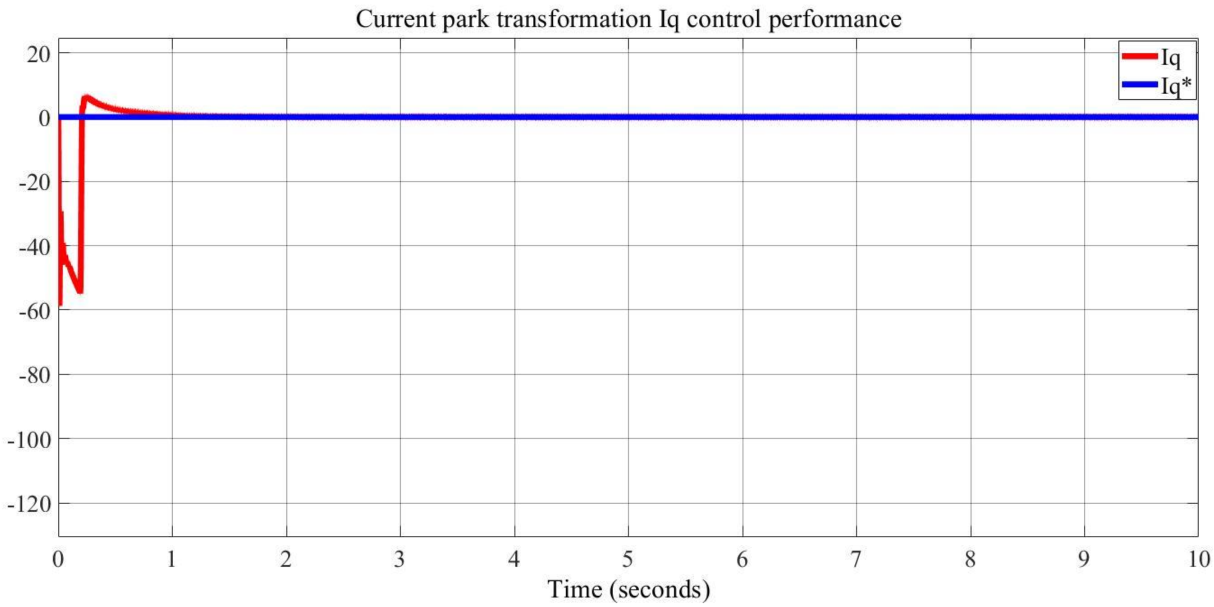

Figure 4.8: Current park transformation control performance

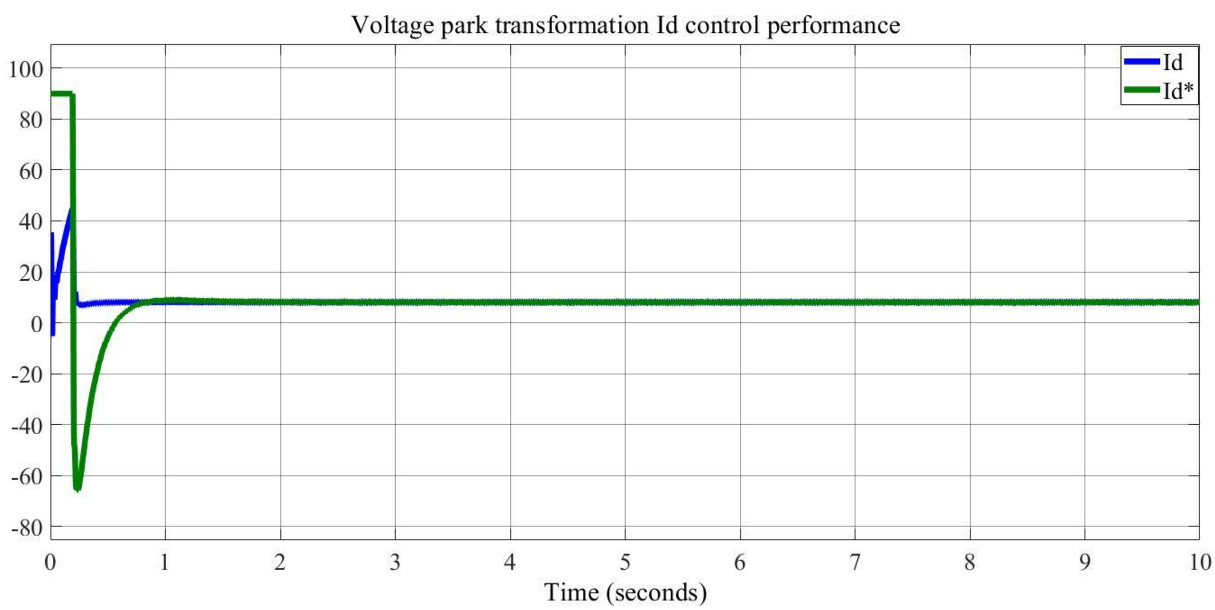

Figure 4.9: Voltage park transformation control performance

4.2.3 Second Stage LLC Resonant DC-DC Converter Result

A MATLAB simulation is conducted for an offboard electric vehicle battery charger, which operates within an output voltage range of 200-450 V and has a maximum output power of 50kW. The system's rated output voltage, obtained after the frontend rectifier, is then fed into the LLC resonant converter. Figure 4.8 illustrates the complete bridge LLC resonant circuit. Frequency modulation technique is used for the control of LLC resonant converter.

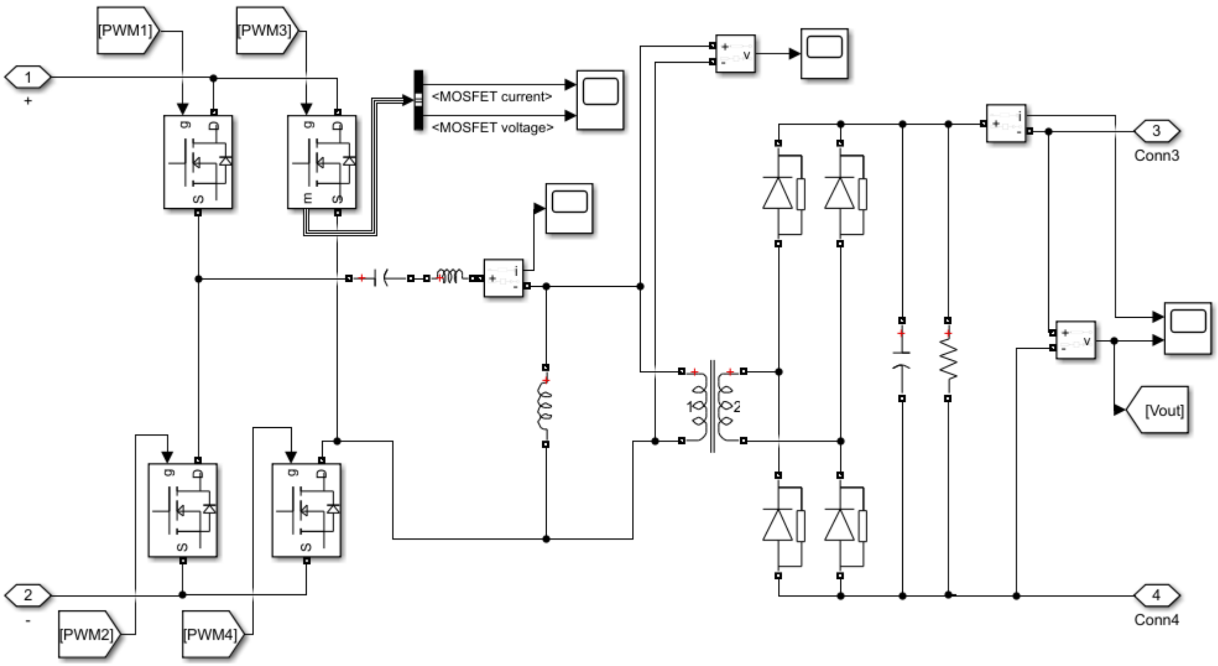

Figure 4.10: Full bridge LLC resonant model

In a full-bridge rectifier, zero current switching (ZCS) occurs when the MOSFET turns off at the exact point where the current through the MOSFET is zero at the end of the switching half cycle as shown in Figure 4.11.

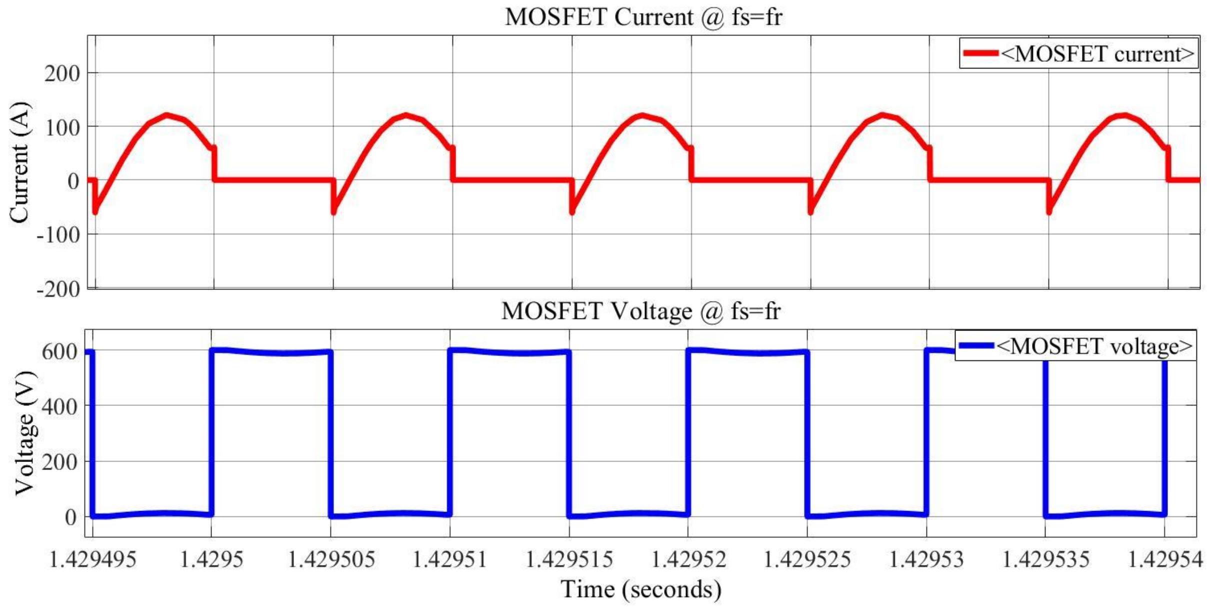

Figure 4.11: Upper waveform MOSFET current and lower waveform MOSFET voltage in switching frequency operating at resonant frequency

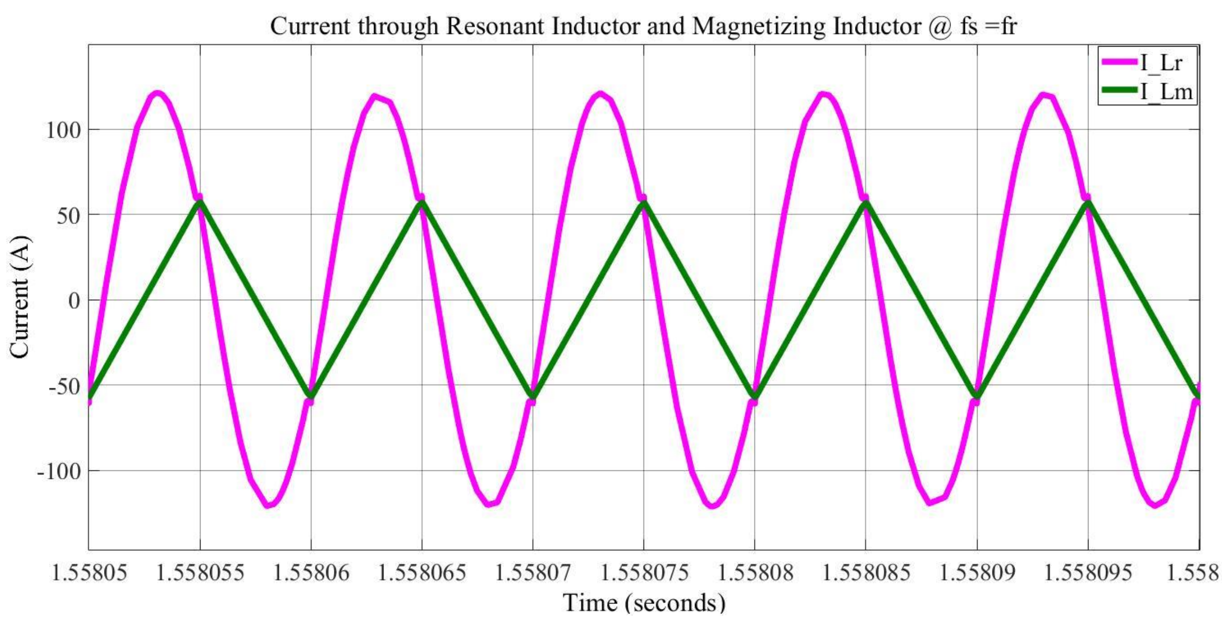

Figure 4.12: Resonant inductor and magnetizing inductance current waveform of resonant circuit for switching frequency at resonant frequency

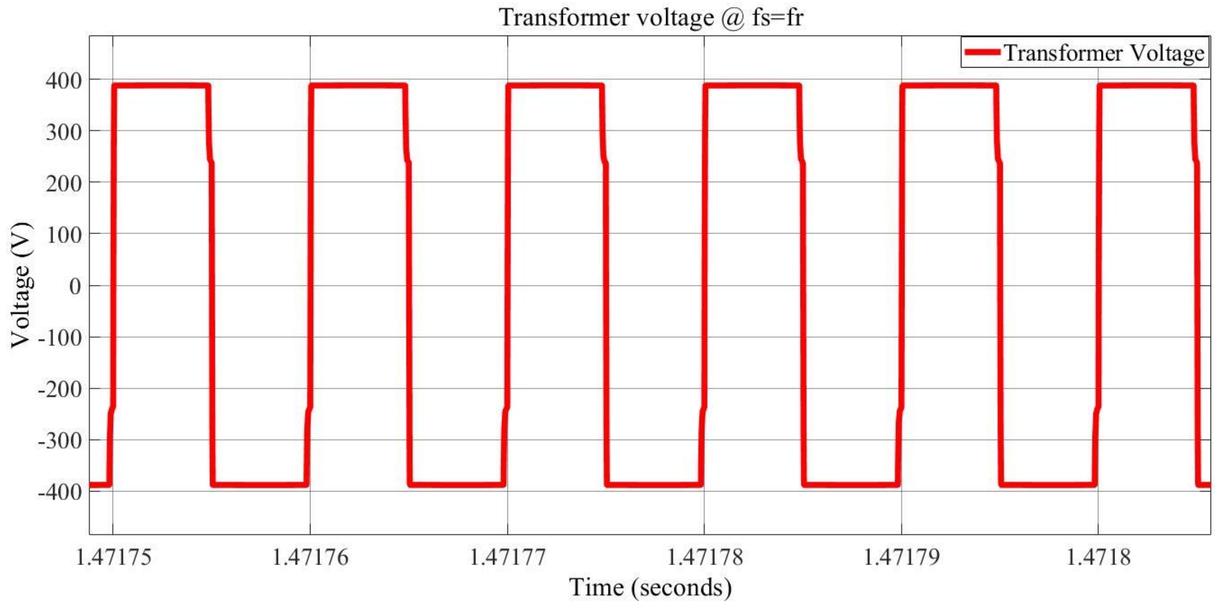

Figure 4.13: Voltage through the transformer for switching frequency at resonant frequency operation

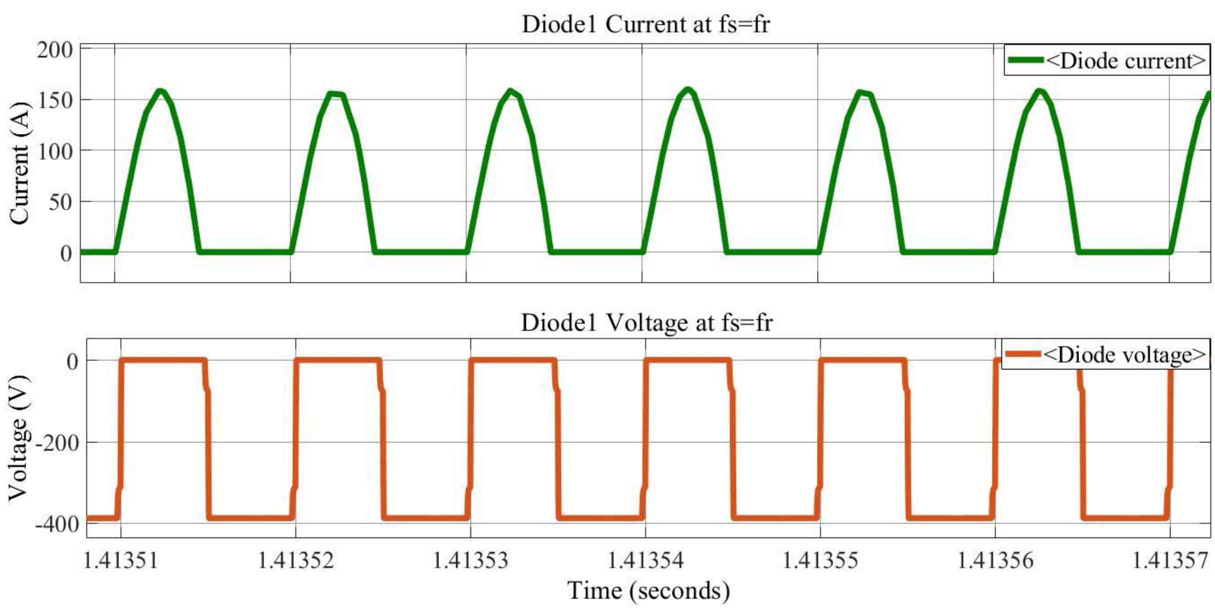

Figure 4.14: Upper diode current and lower diode voltage at 100 kHz switching frequency

Figure 4.15 shows the output voltage and current of LLC resonant converter operating at 100 kHz which is the switching frequency is at resonant frequency. The output voltage is 386.7 V and the current is 95.48 A.

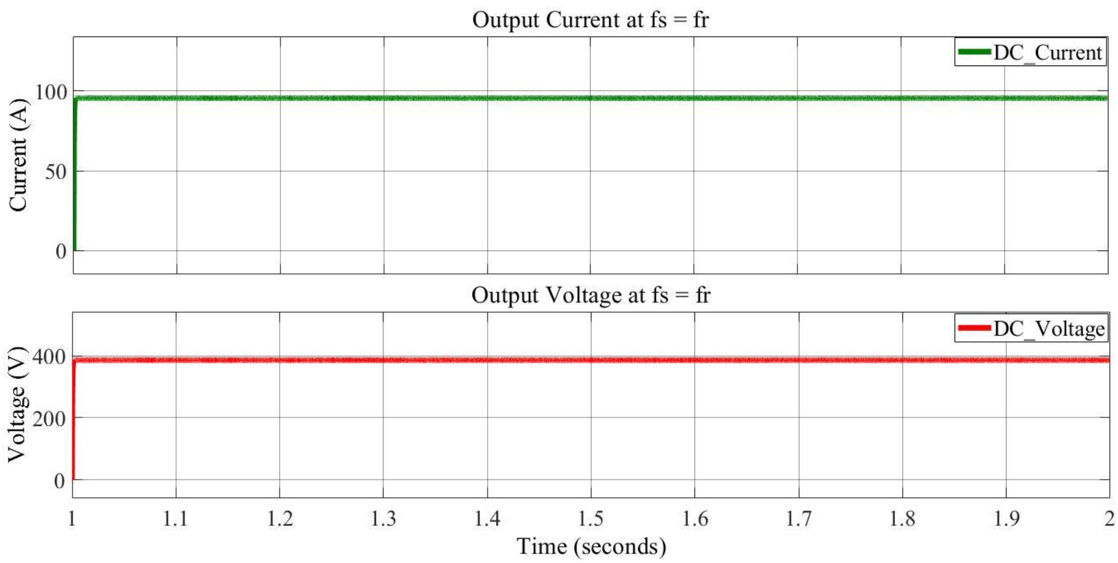

Figure 4.15: Upper output current and lower output voltage waveform in switching frequency operating at resonant frequency

When the switching frequency matches the resonant frequency of the circuit, a phenomenon called zero current switching (ZCS) can occur. In a full bridge rectifier, ZCS happens when the MOSFETs turn off precisely at the point where the current through them becomes zero, at the end of the switching half-cycle. The advantage of ZCS is that it reduces the switching losses and stress on the MOSFETs. By switching off the MOSFETs when the current is already zero, it minimizes power dissipation and improves overall efficiency.

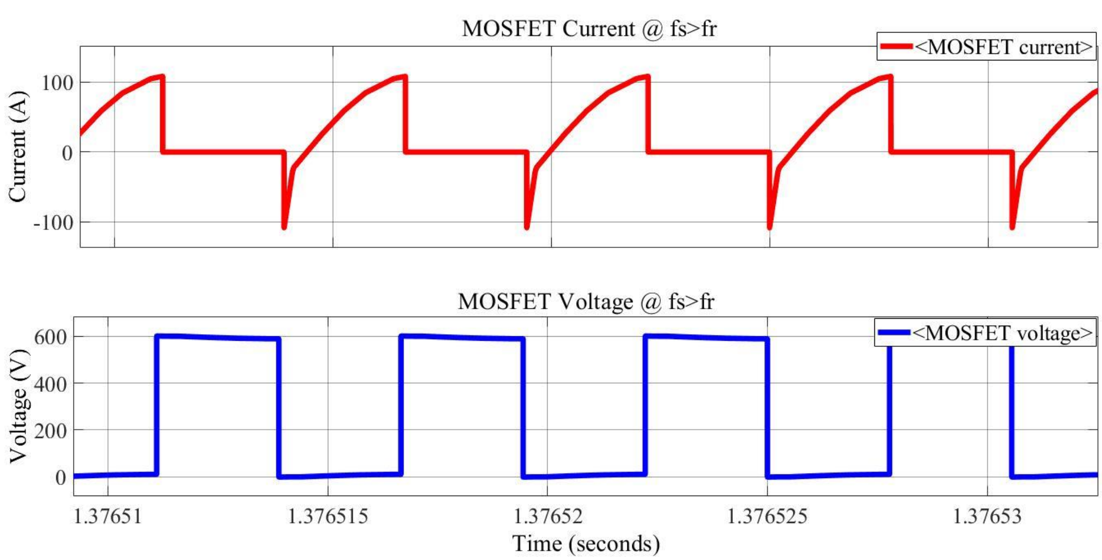

Figure 4.16: Upper MOSFET current and lower MOSFET voltage operating at switching frequency greater than resonant frequency

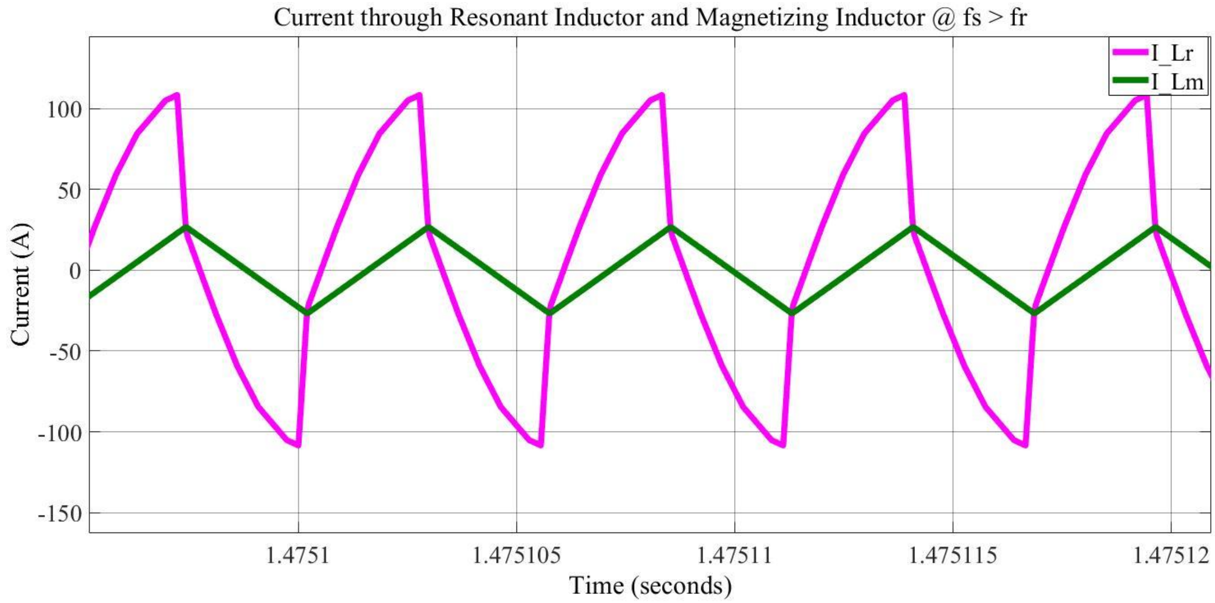

Figure 4.17: Current waveform through resonant inductor and magnetizing inductor at switching frequency greater than resonant frequency

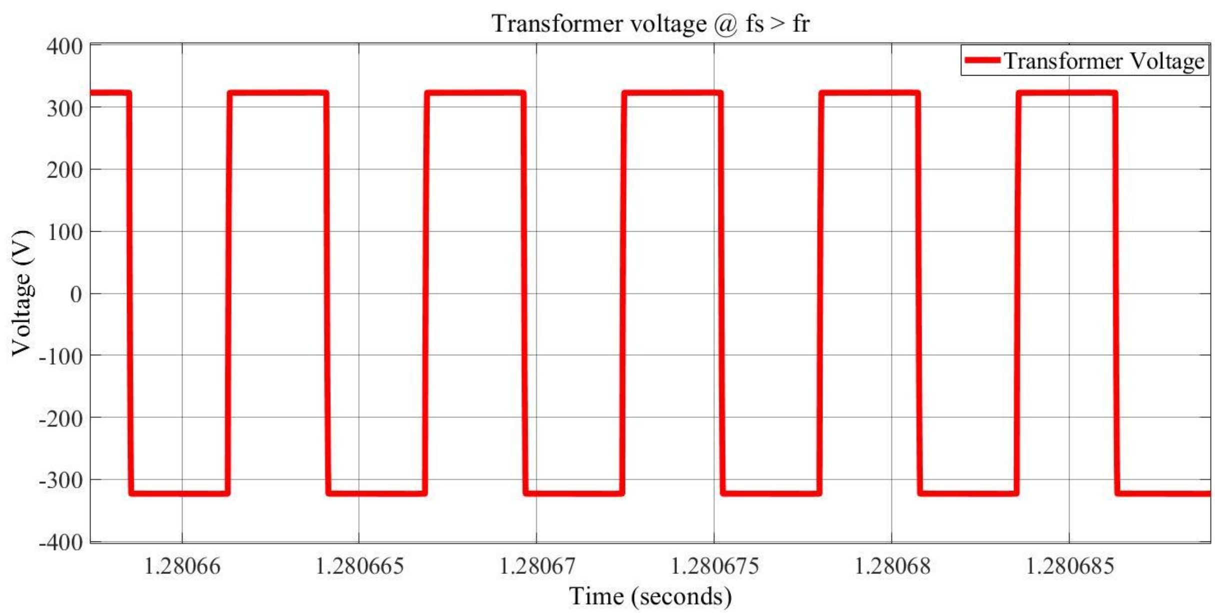

Figure 4.18: Voltage through the transformer for switching frequency greater than resonant frequency

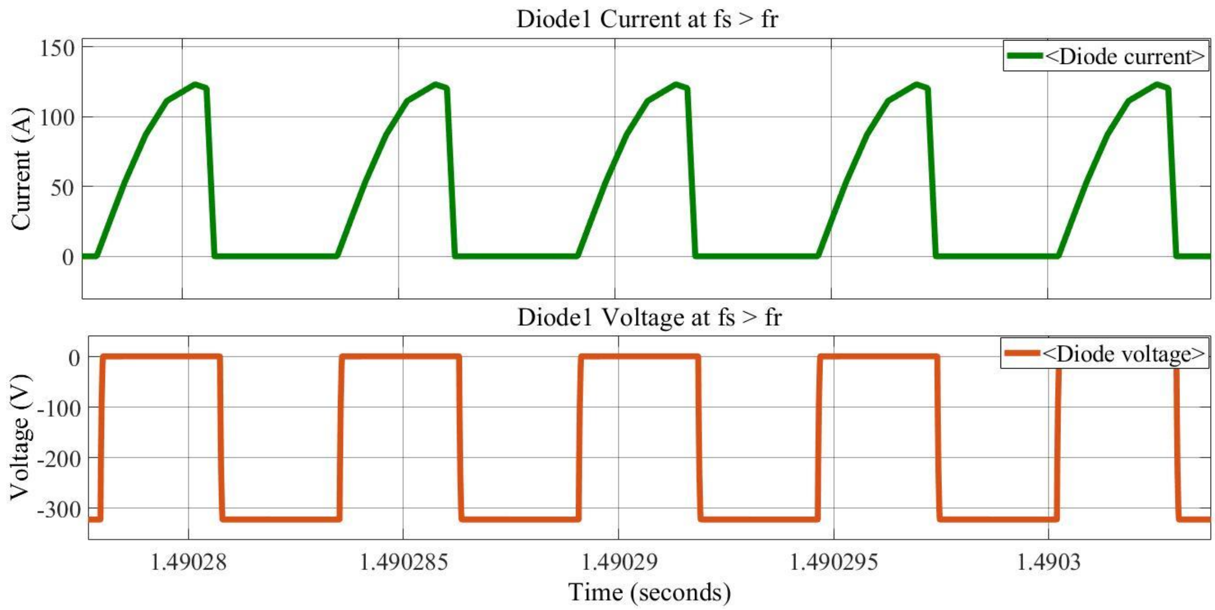

Figure 4.19: Upper diode current and lower diode voltage for switching frequency greater than resonant frequency

The output voltage and current waveform at a switching frequency greater than resonant frequency is depicted in Figure 4.20, the output shows a current value of 76.59 A and voltage of 310.2 V.

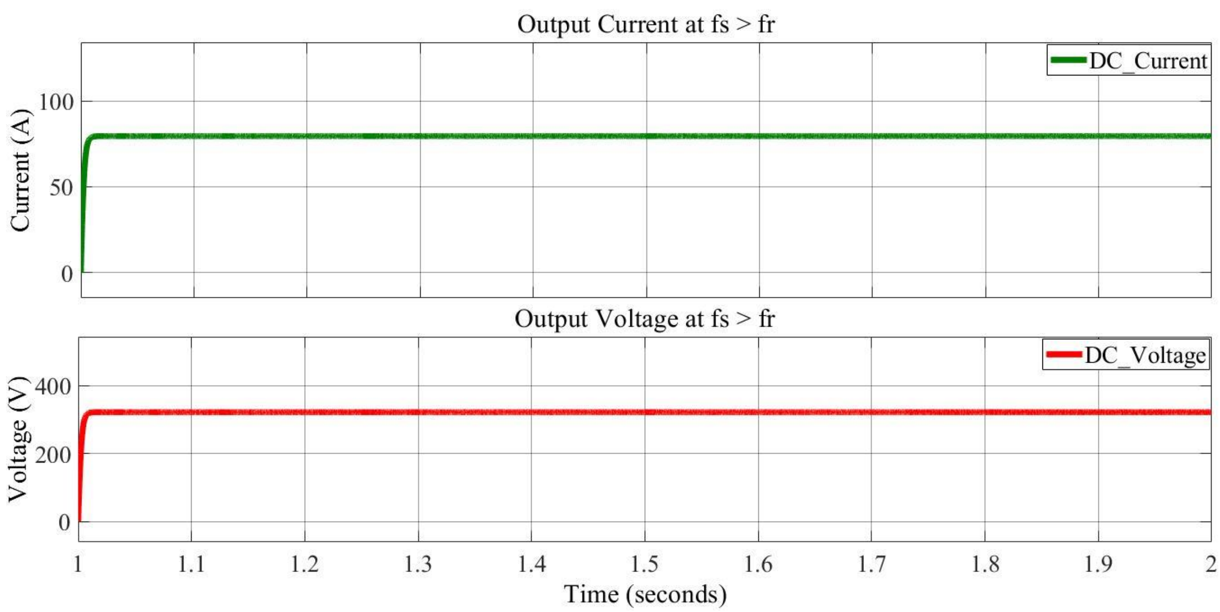

Figure 4.20: Upper output current and lower output voltage at switching frequency greater than resonant frequency

When operating above the resonant frequency, the MOSFET experiences higher turn-off losses. Turn-off losses occur because the MOSFET needs to stop conducting current, and this process generates heat and reduces efficiency. On the secondary side of the LLC resonant converter, a rectifier diode is used to convert the alternating voltage from the transformer into a direct voltage. Operating above the resonant frequency can lead to hard commutation in the diode. Hard commutation means that the diode has to suddenly stop conducting current, which can generate high voltage spikes, cause stress on the diode, and result in increased power losses. Both of these issues contribute to decreased efficiency and can impact the overall performance and reliability of the LLC resonant converter.

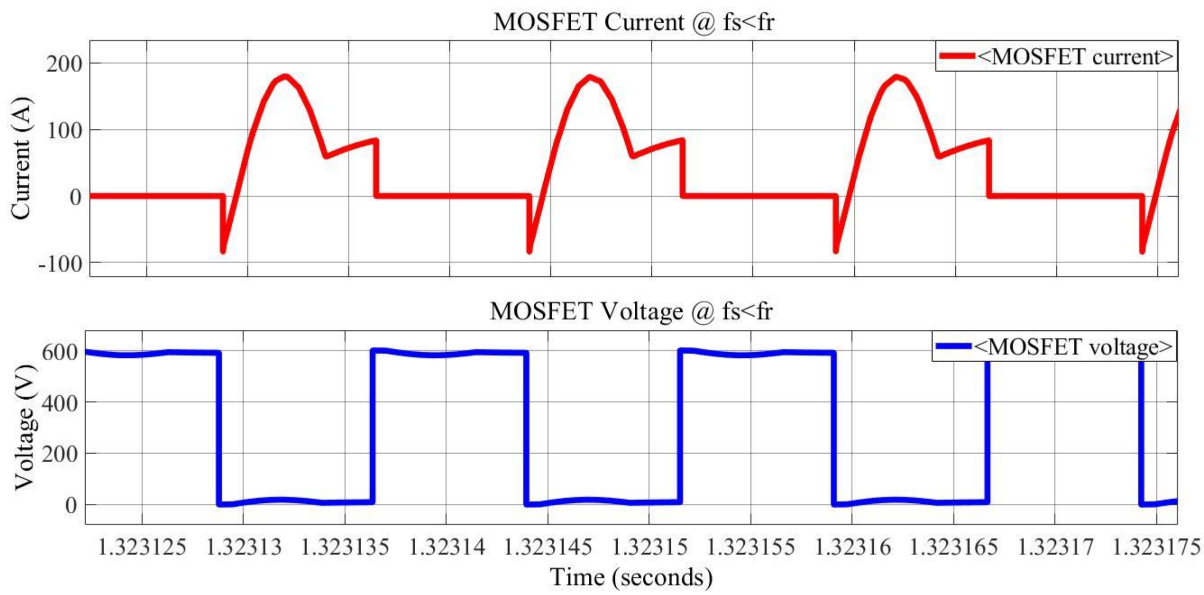

Figure 4.21: Upper MOSFET current and lower MOSFET voltage operating at switching frequency less than resonant frequency

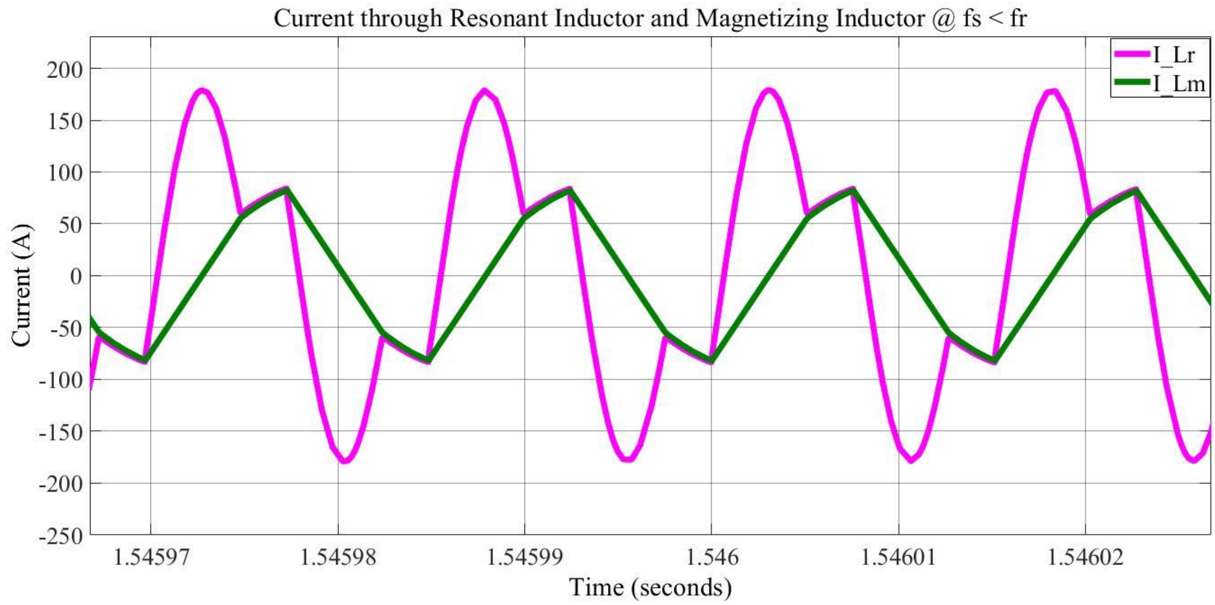

Figure 4.22: Current waveform through resonant inductor and magnetizing inductor at switching frequency less than resonant frequency

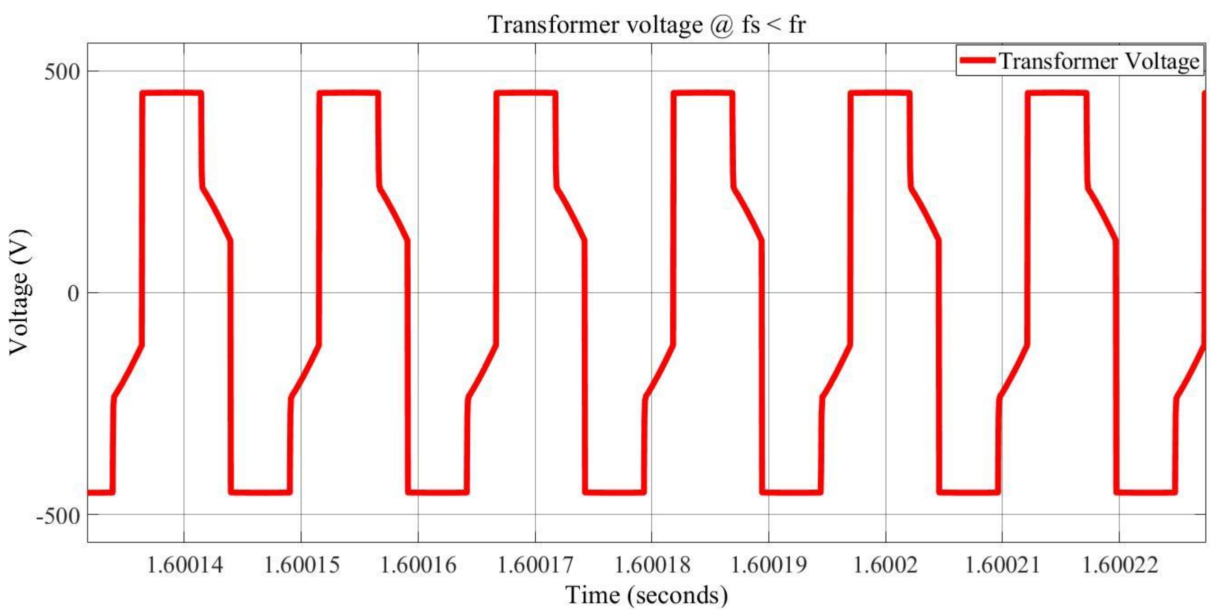

Figure 4.23: Voltage through the transformer for switching frequency less than resonant frequency operation

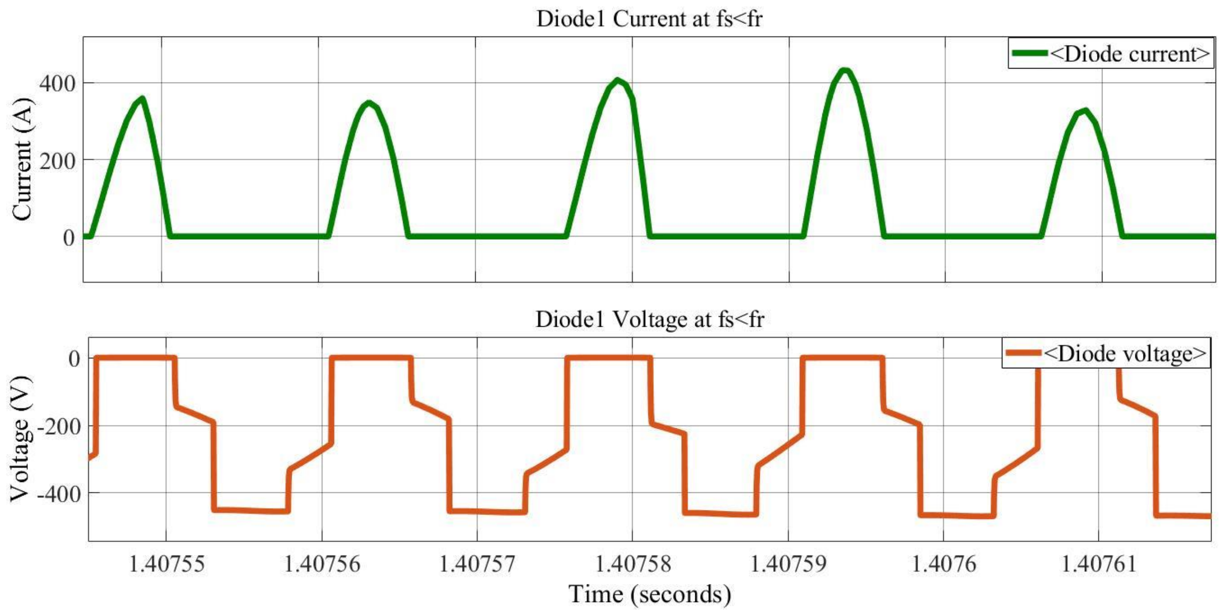

Figure 4.24: Upper diode current and lower diode voltage for switching frequency less than resonant frequency

Figure 4.25 shows the output current of 110.8 A and voltage 448.9 V while operating the LLC resonant converter at 66 kHz switching frequency which is less than resonant frequency. Higher voltage level can be achieved at lower frequency however, conduction loss increases.

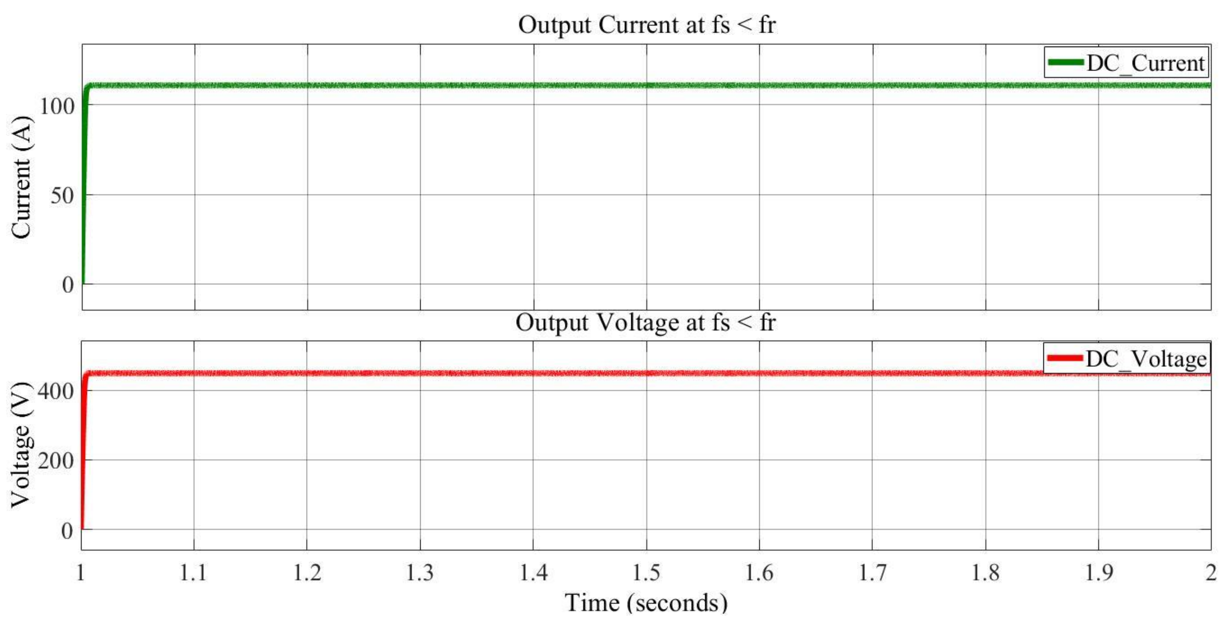

Figure 4.25: Upper output current and lower output voltage at switching frequency less than resonant frequency

When operating below the resonant frequency, the converter requires longer switching periods. This extended switching period leads to longer conduction times for the primary side components, causing an overall increase in conduction loss. In this mode, a boosting operation can still be achieved. However, it comes with the consequence of the converter running at a lower input voltage.

The expected output is achieved in between switching frequency near to resonant frequency and less. The output ripple can be managed using appropriate filter circuit.

4.3 HOMER Based Simulation Result and Discussion

HOMER allows users to customize charging strategies for EVs. In grid connected system simulation result there are three optimized options as shown in Figure 4.26.

Case I: Grid, battery and converter without solar system

Case II: Grid, battery and PV with solar system

Case III: Grid, battery and converter with 113 kW solar system

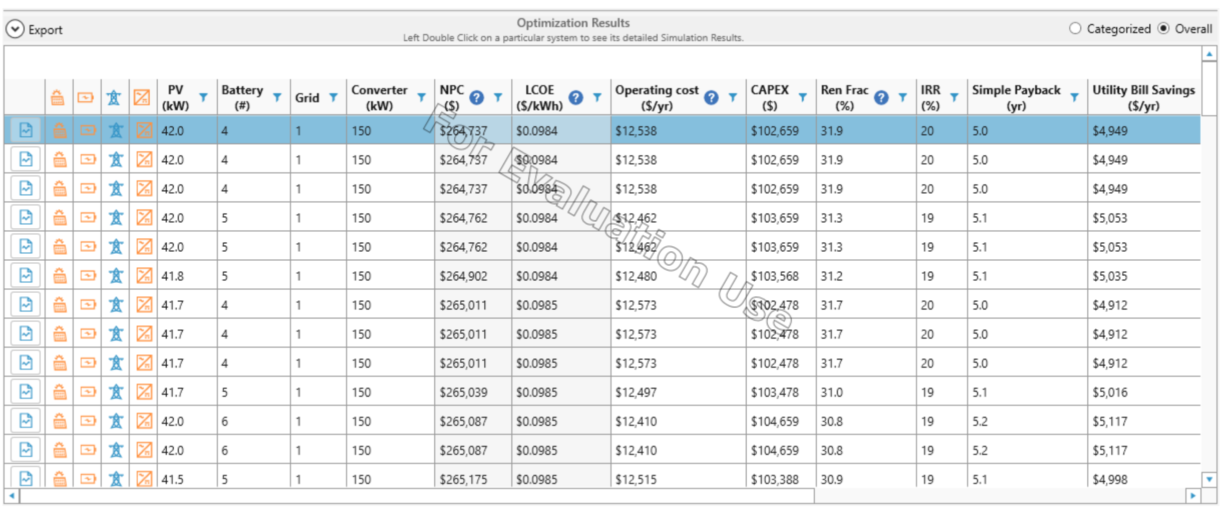

PV (kW)	Battery (#)	Grid	Converter (kW)	NPC ($)	LCOE ($/kWh)	Operating cost ($/yr)	CAPEX ($)	Ren Frac (%)	IRR (%)	Simple Payback (yr)	Utility Bill Savings ($/yr)
42.0	4	1	150	$264,737	$0.0984	$12,538	$102,659	31.9	20	5.0	$4,949
42.0	4	1	150	$264,737	$0.0984	$12,538	$102,659	31.9	20	5.0	$4,949
42.0	4	1	150	$264,737	$0.0984	$12,538	$102,659	31.9	20	5.0	$4,949
42.0	5	1	150	$264,762	$0.0984	$12,462	$103,659	31.3	19	5.1	$5,053
42.0	5	1	150	$264,762	$0.0984	$12,462	$103,659	31.3	19	5.1	$5,053
41.8	5	1	150	$264,902	$0.0984	$12,480	$103,568	31.2	19	5.1	$5,035
41.7	4	1	150	$265,011	$0.0985	$12,573	$102,478	31.7	20	5.0	$4,912
41.7	4	1	150	$265,011	$0.0985	$12,573	$102,478	31.7	20	5.0	$4,912
41.7	4	1	150	$265,011	$0.0985	$12,573	$102,478	31.7	20	5.0	$4,912
41.7	5	1	150	$265,039	$0.0985	$12,497	$103,478	31.0	19	5.1	$5,016
42.0	6	1	150	$265,087	$0.0985	$12,410	$104,659	30.8	19	5.2	$5,117
42.0	6	1	150	$265,087	$0.0985	$12,410	$104,659	30.8	19	5.2	$5,117
41.5	5	1	150	$265,175	$0.0985	$12,515	$103,388	30.9	19	5.1	$4,998

Figure 4.26: Sensitivity and optimization result of the grid connected solar system

Case I: Grid source is only available in this category. The result has a total net present cost (NPC) of $302,089, operating cost of $4,692/yr, and levelized cost of energy (LCOE) $0.112/kWh. The total installed cost of component at the beginning of the project (CAPEX) is $79,000

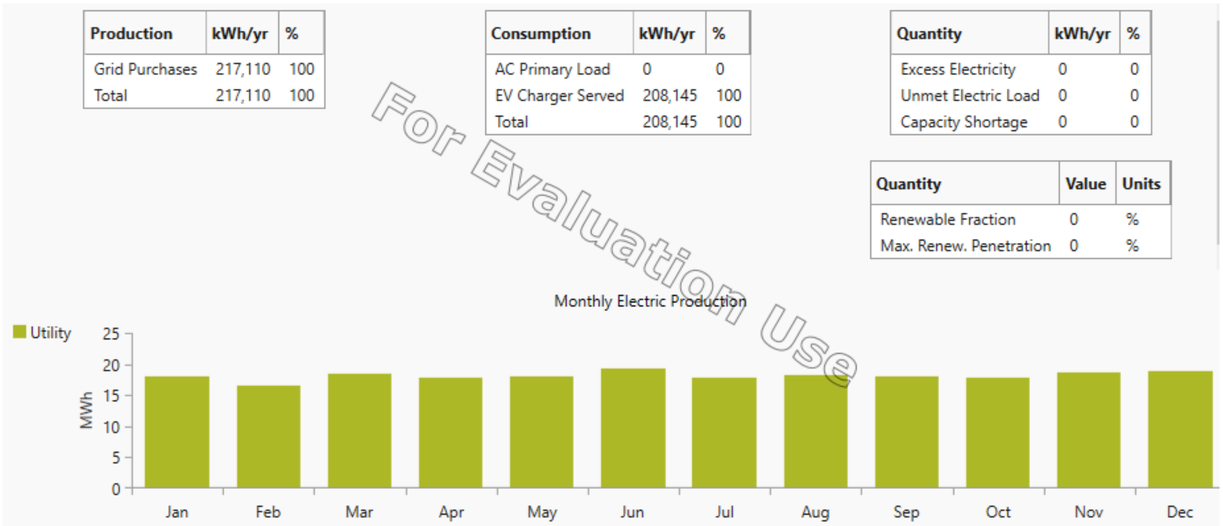

Figure 4.27: The electrical simulation result for the first case

Case II: All sources are available in this category. The optimization result has net present cost (NPC) of $264,737.4, operating cost of $12,537.5/yr, and a renewable fraction of 31.9%. The total installed cost of component at the beginning of the project (CAPEX) is $102,659 and levelized cost (LCOE) of the system is $0.09839/kWh which is relatively good compared to other options. The system has a payback period of 5 years.

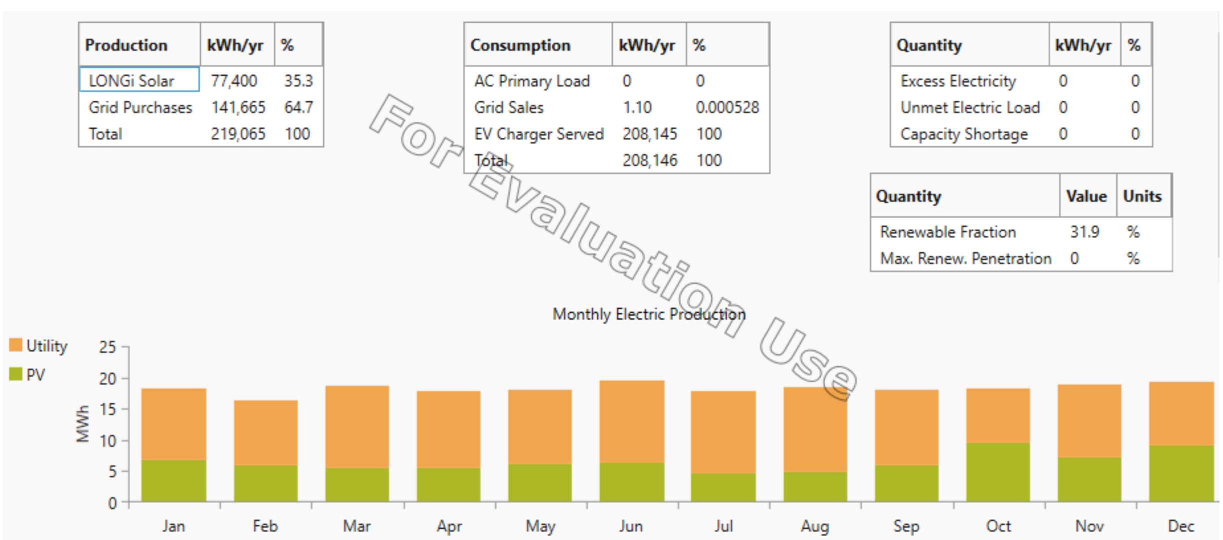

Figure 4.28: Electrical simulation result for case two

Case III: The optimization result has a net present cost (NPC) of $200,779.3, operating cost of $5,930.08/yr, and a renewable fraction of 67.8%. The levelized cost (LCOE) of the system is $0.07446/kWh. The system has a payback period of 8.4.

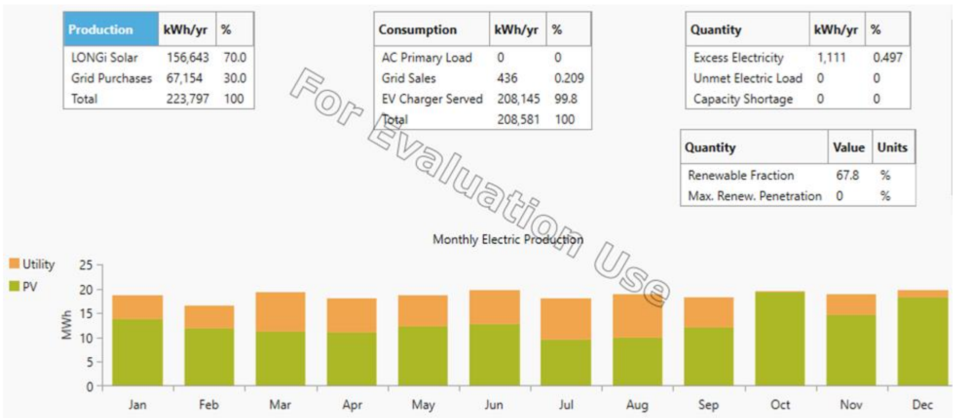

Figure 4.29: Electrical simulation result for case three

Comparing economics, the second optimization result is selected for this thesis. The system has the lowest net present cost, with operating cost is higher as compared with the first case and lower compared to case III. The system has a better levelized cost of energy and renewable fraction.

Table 4.1: Comparison of the optimized result

Comparison parameters	Case I	Case II	Case III
Net present cost (NPC)	$302,089	$264,737.4	$200,779.3
Operating cost ($/yr)	$4,692/yr	$12,537.5/yr	$5,930.08/yr
Levelized cost (LCOE)	$0.112/kWh	$0.09839/kWh	$0.07446/kWh
Renewable fraction (%)	0	31.9	67.8
Installed cost of component (CAPEX)	$79,000	$102,659	$153,653

CHAPTER FIVE

5 CONCLUSION AND RECOMMENDATION

5.1 Conclusion

This thesis focuses on the design and optimization of a grid-connected solar-powered electric vehicle charging station. To accomplish this, advanced software tools such as HOMER and MATLAB Simulink were employed. These software platforms facilitated the assessment of the proposed converter's suitability and advantages. Additionally, the thesis delves into detailed theoretical analyses to establish design guidelines for the grid-connected solar system. The aim is to provide valuable insights and recommendations for the development and implementation of efficient and effective solar-powered charging stations for electric vehicles.

- The design considerations were made for electric vehicles with an average battery capacity of 71.3 kWh per vehicle and a total energy consumption of 570.4 kWh.
- A grid-connected solar system with a capacity of 113.56 kW was designed, taking the recorded minimum daily sunshine duration of 4.7 hours with the inclusion of 2 lithium-ion batteries.
- The electric vehicle charger was designed with a maximum rated capacity of 50 kW per output port, within a voltage range of 200-450 V.

Due to this constraint, various system configurations were explored to accommodate the specific electric vehicle load. One feasible system configuration was selected to ensure the overall system could reliably supply the entire load, while accounting for variations in radiation input and cost. The chosen system setup included photovoltaic panels, grid connection, batteries, and a converter. The analysis of this sample system revealed a cost of electricity (COE) of $0.09839 per kilowatt-hour and a total net present cost (NPC) of $264,737.4 with a payback period of 5 years.

5.2 Recommendations

The following points are outlined with the purpose of providing recommendations and guiding future efforts

- The off-board charging system performance and efficiency can be further improved by using Battery management system.
- In relation to environmental concerns, it is imperative to promote the widespread adoption of hybrid systems in order to mitigate the impact of greenhouse gases and reduce reliance on the power grid.
- Ultimately, the system that has been designed is simulated using both MATLAB Simulink and HOMER software to demonstrate its cost-effectiveness. Therefore, it is recommended for both the university, the utility company and other non-governmental organizations to consider translating this documentation into practical implementation.

REFERENCES

Abdel-Rahman, S. (2012). *Resonant LLC Converter: Operation and Design.* North America: Infineon Technologies North America (IFNA) Corp.

AlHammadi , A., Al-Saif , N., Al-Sumaiti , S. A., Marzband , M., Alsumaiti , T., & Forushani , H. E. (2022). Techno-Economic Analysis of Hybrid Renewable Energy Systems Designed for Electric Vehicle Charging: A Case Study from the United Arab Emirates. *energies*. Retrieved from https://doi.org/10.3390/

Alkahtani, A. A., Noman, F., Agelidis, V., Tiong, K. S., Alkawsi, G., & Ekanayake, J. (2020). Wind-Energy-Powered Electric Vehicle Charging Station: Resource Availability Data Analysis. *Applied Sciences, 10*(16), 13. doi:10.3390/app10165654

Arif, S. M. (2021). Review of Electric Vehicle Technologies, Charging Methods, Standards and Optimization Techniques. *Electronics 2021*.

Astrom, K. J. (2002). Controller System Design. Santa Barbara.

Badase, K. A. (2020, January). Fuzzy and PLL Based MPPT System Design for Energy Efficiency of PV System: With A Case Study in Samara University.

Bhattacharya, T., Giri, V. S., Mathew, K., & Umanand, L. (2009). Multiphase Bidirectional Flyback Converter Topology for Hybrid Electric Vehicles. *IEEE TRANSACTIONS ON INDUSTRIAL ELECTRONICS*, 78-84.

Biya, S. T., & Sindhu, R. M. (2019). Design and Power Management of Solar Powered Electric Vehicle Charging Station with Energy Storage System. *2019 3rd International conference on Electronics, Communication and Aerospace Technology (ICECA)* (p. 5). Coimbatore, India: IEEE. doi:https://doi.org/10.1109/ICECA.2019.8821896

Bradbury, K. (2010). *Energy storage technology review.* ResearchGate.

Chandler , S., Gartner, J., & Jones, D. (2018). Integrating Electric Vehicles with Energy Storage and Grids: New Technology and Specific Capabilities Spur Numerous Applications. *IEEE Electrification Magazine*, 38-43.

Chiras, D. (2020). *Solar Electricity Basics.* canada: new society publishers.

contributors, W. (2022, November 18). *Adama*. Retrieved from Wikipedia, The Free Encyclopedia: https://en.wikipedia.org/w/index.php?title=Adama&oldid=1121724821

Cronemberger, J., Martin, E. C., & Sanchez, S. V. (2012). Assessing the solar irradiation potential for solar photovoltaic applications in buildings at low latitudes-Making the case for Brazil. *ELSEVIER*.

Dv., L. G. (2021). Electric and hybrid electric vehicles. *International Journal of Research and Analytical Reviews , 8*(4), 8.

EBC. (2022, july 13). newsdaily. Retrieved from https://www.youtube.com/watch?v=RQyKuoVBErw

Friedli, T., Hartmann, M., & Kolar, J. W. (2013). The Essence of Three-Phase PFC Rectifier Systems Part II. *IEEE*, 7-8.

Gautam , R., Gautham , R. M., & Pavol , B. (2022). A Comprehensive Review on Off-Grid and Hybrid Charging Systems for Electric Vehicles. (P. F. Baronti, Ed.) *IEEE Open Journal of the Industrial Electronics Society*, *3*, 203-222. doi:10.1109/OJIES.2022.3167948

Golestan, S., & Vasquez, J. C. (2016). Three-Phase PLLs: A Review of Recent Advances. *IEEE TRANSACTIONS ON POWER ELECTRONICS*, 14.

greentecafrica. (2023). Retrieved from greentecafrica: https://greentecafrica.com

Habib, S., Khan, M. M., & Abbas, F. (2017). Assessment of electric vehicles concerning impacts, charging infrastructure with unidirectional and bidirectional chargers, and power flow comparisons. *International Journal of Energy Research*, 27.

Hadero, M., & Khan, B. (2022). Development of DC Microgrid Integrated Electric Vehicle Charging Station With Fuzzy Logic Controller. 1-18. doi: 10.3389/fenrg.2022.922384

Hart, D. W. (2011). *Power Electronics.* New York: McGraw-Hill.

Higueras, P. P., & Fernández, E. F. (2015). *High Concentrator Photovoltaics Fundamentals, Engineering and Power Plants.* Switzerland: Springer International Publishing.

Ho, A. K. (2020). *https://pdhonline.com.* Retrieved from PDH Online: https://pdhonline.com/courses/e331/e331content.pdf

Homer Energy. (2023). *https://www.homerenergy.com/products/grid/index.html*. Retrieved from Homer Energy: https://www.homerenergy.com/products/grid/index.html

IEA. (2023). Global EV Outlook 2023. *8th Annual Global Conference on Energy Efficiency* (pp. 43-55). Paris: International Energy Agency. Retrieved from https://www.iea.org/reports/global-ev-outlook-2023

Ikegami, T., Maezono, T., Nakanishi, F., Yamagata, Y., & Ebihara, K. (2001). Estimation of equivalent circuit parameters of PV module and its application to optimal operation of PV system. *Solar Energy Materials & Solar Cells*, 389-395.

Kanaparthi, R. K., Singh, J. P., & Ballal, M. S. (2022). A Review on Multi-Port Bidirectional Isolated and Non-Isolated DC-DC Converters for Renewable Applications. *Power Electronics, Drives and Energy Systems (PEDES).* IEEE.

Keshan, H., Thornburg, J., & Ustun, T. S. (2016). Comparison of lead-Acid and Lithium Ion batteries for stationary storage in off-grid energy systems . *IEEE*.

Krasselt, P., Boßle, J., Suriyah, M. R., & Leibfried, T. (2015). DC-Electric Vehicle Supply Equipment Operation Strategies for Enhanced Utility Grid Voltage Stability. *World Electric Vehicle Journa*, 10.

Lera, W. (2020, July). Feasibility Study and Design of Standalone Hybrid Power Generation System for Rural Area In Ethiopia: Case Study Of Minjar-Shenkora Woreda. Ethiopia.

M. A. Laguado-Serrano1, E. A.-P.-M.-M. (2019). Performance comparison between PWM and MPPT charge controllers . *https://www.researchgate.net, 24*. Retrieved 2020

marathoncars. (2023). Retrieved from https://marathoncars.com

Michael Hicks. (2023, January 29). *AC charging*. Retrieved from Wikipedia, Tesla: https://en.wikipedia.org/wiki/AC charging

Mikael Hicks. (2023, January 29). *DC charging*. Retrieved from Wikipedia, Tesla: https://en.wikipedia.org/wiki/

Mouli, C., & Ram, G. (2018). Charging electric vehicles from solar energy: Power converter, charging algorithm and system design. 45-46. doi:10.4233/uuid:dec62be4-d7cb-4345-a8ae-65152c78b80f

N.R., B. (2017). *Smart Grid Systems: Moodeling and Control* (1st ed ed.). Apple Academic Press. Retrieved from https://doi.org/10.1201/9781315111124

Nam, N. N., & Kim, S. H. (2022). Robust Tracking Control of Dual-Active-Bridge DC–DC Converters with Parameter Uncertainties and Input Saturation. *MDPI*, 1-19.

Neha, D., Shakila, N., Seema, J., & Vaibhav, B. (2018). Bidirectional DC-DC converter in Solar PV System for Battery Charging Application. *International Conference on Smart City and Emerging Technology (ICSCET).* Mumbai: IEEE. doi:10.1109/ICSCET.2018.8537391

Orhan, E., & Celal, H. C. (2021). Sizing of a solar-wind hybrid electric vehicle charging station by using HOMER software. (C. M. Almeida, Ed.) *Journal of Cleaner Production, 279*, 1-13. Retrieved from https://doi.org/10.1016/j.jclepro.2020.123615

Panda, K. P., & Rout, S. (2016). A Cost-Effective Design and Analysis of Full Bridge LLC Resonant Converter. *World Academy of Science, Engineering and Technology International Journal of Energy and Power Engineering*, 8.

Patel, M. (2006). *Wind and Solar Power Systems* (Second Edition ed.). (Taylor & Francis, Ed.)

Pop, L., & Avram, D. (2018). *Off Grid And Mobile Solar Power For Everyone.* Digital Publishing Ltd.

Powar, V., & Singh, R. (2023). End-to-End Direct-Current-Based Extreme Fast Electric Vehicle Charging Infrastructure Using Lithium-Ion Battery Storage. *Batteries*, 30. Retrieved from https://doi.org/10.3390/batteries9030169

Radish, M. H. (2015). *Alternative Energy in Power Electronics.* USA: ELSEVIER.

Rashid, M. H. (2014). *Power Electronics Devices, Circuits, and Applications* (Fourth Edition ed.). Pearson Education Limited.

Sechilariu, M., Reinders, A., Krim, Y., Cheikh-Mohamad, S., Sierra, A., Seiler, G., & Ben-Slimane, K. (2021). *PVPS, PV-Powered Electric Vehicle Charging Stations Preliminary Requirements and Feasibility Conditions.* International Energy Agency.

Shahir, F. M., Gheisarnejad, M., Sadabadi, M. S., & Khooban, M. H. (2021). A new Off-board Electrical Vehicle Battery Charger: Topology, Analysis and Design. *MDPI designs*, 15.

Shatnawi, M., Qaydi, N. A., Aljaberi, N., & Aljaberi, m. (2018). Hydrogen-Based Energy Storage Systems: A Review. *2018 7th International conference on renewable energy research and applications.*

Singh, A., & VS, J. (2021). *Voltage Fed Full Bridge DC-DC and DC-AC Converter for High-Frequency Inverter Using C2000.* Texas Instruments Incorporated.

T. Li et al. (2018). An Optimal Design and Analysis of a Hybrid Power Charging Station for Electric Vehicles Considering Uncertainties. *44th Annual Conference of the IEEE Industrial Electronics Society, 2018* (pp. 5147-5152). Washington, DC, USA: IEEE. doi:10.1109/IECON.2018.8592855

TDK-Lambda. (2020). *DC-DC converter switching frequencies*. Retrieved from TDK-Lambda-Corporation: https://www.us.lambda.tdk.com/resources/blogs/20220425.html

Tilahun, M. (2020, October). Study on Technical Feasibility and Design of Grid Connected Solar PV Based Power Supply System for the Ethio-Djibouti Railway Line.

Wang, D., Locment, F., & Sechilariu, M. (2020). Modelling, Simulation, and Management Strategy of an Electric Vehicle Charging Station Based on a DC Microgrid. *Applied Sciences*, 1-21. doi:10.3390/app10062053

Williams, B. (2020, December). Retrieved from Ironedison: https://ironedison.com/battery/

Yehualawork, F. (2019, July). Study and Design of Solar and Micro-Hydro Hybrid System for Rural Area of Debre Berhan, Ethiopia. Ethiopia. Retrieved from http://etd.aau.edu.et/handle/123456789/19540

Yi, S., & Jingru, L. (2016). Study on the Typical Mode of EV Charging and Battery Swap Infrastructure Interconnecting to Power Grid. *China International Conference on Electricity Distribution.* china.

Zhaksylyk, A., Rasool, H., Abramushkina, E., Chakraborty, S., Geury, T., El Baghdadi , M., & Hegazy, O. (2023). Review of Active Front-End Rectifiers in EV DC. *batteries*.

Zunaib , A., Nicholas , C., Lenos , H., Elias , K., Yongheng , Y., & Frede , B. (2018). Three-Phase Phase-Locked Loop Synchronization Algorithms for Grid-Connected Renewable Energy Systems: A Review. *Renewable and Sustainable Energy Reviews*.

APPENDIXES

Appendix A

Solar module specification

Electrical Characteristics — Test uncertainty for Pmax: ±3%

Model Number	LR6-60HPH-305M		LR6-60HPH-310M		LR6-60HPH-315M		LR6-60HPH-320M		LR6-60HPH-325M	
Testing Condition	STC	NOCT	STC	NOCT	STC	NOCT	STC	NOCT	STC	NOCT
Maximum Power (Pmax/W)	305	225.9	310	229.6	315	233.4	320	237.1	325	240.8
Open Circuit Voltage (Voc/V)	40.1	37.4	40.3	37.7	40.6	37.9	40.9	38.2	41.1	38.4
Short Circuit Current (Isc/A)	9.78	7.88	9.86	7.94	9.94	8.01	10.02	8.08	10.12	8.16
Voltage at Maximum Power (Vmp/V)	33.1	30.6	33.3	30.8	33.7	31.1	33.9	31.3	34.1	31.5
Current at Maximum Power (Imp/A)	9.21	7.38	9.30	7.46	9.36	7.50	9.43	7.56	9.52	7.64
Module Efficiency(%)	18.2		18.5		18.8		19.1		19.4	

STC (Standard Testing Conditions): Irradiance 1000W/m², Cell Temperature 25℃, Spectra at AM1.5

NOCT (Nominal Operating Cell Temperature): Irradiance 800W/m², Ambient Temperature 20℃, Spectra at AM1.5, Wind at 1m/S

Temperature Ratings (STC)		Mechanical Loading	
Temperature Coefficient of Isc	+0.057%/℃	**Front Side Maximum Static Loading**	5400Pa
Temperature Coefficient of Voc	-0.286%/℃	**Rear Side Maximum Static Loading**	2400Pa
Temperature Coefficient of Pmax	-0.370%/℃	**Hailstone Test**	25mm Hailstone at the speed of 23m/s

Adama City Sunshine Hour 15 Years Recorded Data from Eastern and Central Oromia Meteorology Service Center

STN_Name	EG_GH_ID	EG_EL	YEAR	January	February	March	April	May	June	July	August	September	October	November	December
Nazereth	SHNAZE11	SUNHRS	2008	9.7	9.8	10.4	Na	8.5	7.2	6.9	7.9	8.6	8.8	10.3	9.9
Nazereth	SHNAZE11	SUNHRS	2009	8.4	9.5	9.2	7.5	7.6	8.2	8.8	9.8	7.1	9.4	6.6	8.0
Nazereth	SHNAZE11	SUNHRS	2010	7.7	7.0	8.1	6.0	6.1	7.5	10.2	9.5	9.1	9.8	9.5	8.5
Nazereth	SHNAZE11	SUNHRS	2011	8.8	7.6	6.9	6.3	6.8	10.3	8.7	10.5	9.9	10.0	9.4	7.8
Nazereth	SHNAZE11	SUNHRS	2012	8.8	6.8	6.1	5.5	7.2	9.2	10.1	9.7	8.9	10.1	8.5	8.1
Nazereth	SHNAZE11	SUNHRS	2013	8.4	7.9	5.3	6.9	8.4	8.3	8.8	10.1	9.5	8.7	8.6	9.0
Nazereth	SHNAZE11	SUNHRS	2014	8.7	8.7	6.4	6.9	6.6	8.8	9.4	9.7	9.8	10.1	9.7	8.1
Nazereth	SHNAZE11	SUNHRS	2015	8.0	7.8	9.1	8.2	8.7	8.3	8.1	9.1	8.7	Na	7.4	7.9
Nazereth	SHNAZE11	SUNHRS	2016	6.5	6.8	7.2	9.9	9.1	9.8	10.3	9.0	9.3	9.6	7.9	8.0
Nazereth	SHNAZE11	SUNHRS	2017	6.2	6.0	6.8	8.7	7.9	8.0	6.2	6.0	6.8	8.7	10.0	9.4
Nazereth	SHNAZE11	SUNHRS	2018	9.5	9.1	8.3	6.2	7.4	6.7	7.0	6.6	8.3	9.1	8.9	9.9
Nazereth	SHNAZE11	SUNHRS	2019	10.4	9.6	9.4	8.6	9.0	7.1	6.0	6.4	5.9	8.7	8.2	9.0
Nazereth	SHNAZE11	SUNHRS	2020	8.0	8.6	8.3	8.0	8.8	7.9	5.2	4.9	6.9	9.8	9.7	9.4
Nazereth	SHNAZE11	SUNHRS	2021	9.7	8.2	10.5	8.5	8.6	8.9	4.7	7.9	7.4	8.8	10.1	10.1
Nazereth	SHNAZE11	SUNHRS	2022	9.4	9.9	8.9	9.2	10.1	8.0	4.7	6.7	7.2	8.9	10.4	

Minimum Temperature Data (15 years)

STN_Name	EG_GH_ID	EG_EL	YEAR	January	February	March	April	May	June	July	August	September	October	November	December
Nazareth	SHNAZE11	TMPMIN	2007	14.0	15.8	16.1	16.5	17.9	17.6	16.7	15.6	16.5	13.1	14.1	11.6
Nazareth	SHNAZE11	TMPMIN	2008	13.9	13.7	14.0	16.8	17.3	16.8	15.5	15.4	15.9	14.6	12.8	12.1
Nazareth	SHNAZE11	TMPMIN	2009	13.5	15.2	16.8	17.1	17.5	18.4	16.8	16.7	16.3	14.3	13.3	15.0
Nazareth	SHNAZE11	TMPMIN	2010	14.1	15.4	15.3	16.2	17.4	17.8	16.5	16.9	15.2	14.5	13.9	11.6
Nazareth	SHNAZE11	TMPMIN	2011	13.1	14.2	14.9	16.6	16.3	16.8	16.6	16.7	15.6	14.2	14.9	12.8
Nazareth	SHNAZE11	TMPMIN	2012	14.1	14.1	16.4	16.9	17.0	18.0	15.9	16.0	15.9	13.7	13.9	14.4
Nazareth	SHNAZE11	TMPMIN	2013	14.3	15.1	17.3	17.4	18.3	18.2	15.6	16.7	15.9	14.8	14.7	11.9
Nazareth	SHNAZE11	TMPMIN	2014	13.9	16.4	16.7	17.4	17.3	18.1	17.1	16.5	16.0	14.7	15.0	13.3
Nazareth	SHNAZE11	TMPMIN	2015	12.6	15.8	17.1	16.4	17.2	18.1	17.4	16.6	16.3	17.1	0.0	0.0
Nazareth	SHNAZE11	TMPMIN	2016	15.7	15.4	19.0	17.7	17.3	17.5	16.6	17.0	16.1	15.5	14.8	12.7
Nazareth	SHNAZE11	TMPMIN	2017	12.0	15.6	16.9	17.5	17.0	18.6	16.4	16.7	15.8	15.2	13.7	0.0
Nazareth	SHNAZE11	TMPMIN	2018	12.5	15.2	16.1	16.0	17.0	17.5	16.2	16.4	15.5	15.7	15.3	14.4
Nazareth	SHNAZE11	TMPMIN	2019	13.2	16.6	17.8	17.7	17.4	17.6	16.0	16.7	16.2	14.6	15.1	14.0
Nazareth	SHNAZE11	TMPMIN	2020	13.7	16.1	17.1	17.2	17.2	17.6	16.1	16.3	16.6	15.6	15.2	13.8
Nazareth	SHNAZE11	TMPMIN	2021	13.5	15.0	16.5	17.7	17.0	18.3	16.3	16.6	16.3	14.8	13.9	14.1
Nazareth	SHNAZE11	TMPMIN	2022	15.5	15.2	16.9	17.7	24.1	18.1	16.4	16.5	15.8	15.3	14.8	

Maximum Temperature Data (15 years)

STN_Name	EG_GH_ID	EG_EL	YEAR	January	February	March	April	May	June	July	August	September	October	November	December
Nazareth	SHNAZE11	TMPMAX	2007	26.2	28.4	29.8	28.7	30.9	28.2	25.7	25.4	26.4	27.0	26.1	25.4
Nazareth	SHNAZE11	TMPMAX	2008	26.8	27.1	30.4	29.7	30.1	28.5	25.4	25.2	26.9	27.3	24.7	25.1
Nazareth	SHNAZE11	TMPMAX	2009	25.8	28.0	30.2	29.8	30.9	31.5	26.8	26.2	28.7	27.1	27.2	26.0
Nazareth	SHNAZE11	TMPMAX	2010	26.6	27.3	27.0	29.9	30.2	29.8	25.8	26.0	26.7	28.2	27.2	26.1
Nazareth	SHNAZE11	TMPMAX	2011	27.3	29.4	29.4	31.7	30.8	30.0	27.4	26.2	26.7	27.9	26.9	25.8
Nazareth	SHNAZE11	TMPMAX	2012	27.4	29.0	31.0	30.3	31.7	30.7	25.8	25.9	27.0	27.9	28.0	27.2
Nazareth	SHNAZE11	TMPMAX	2013	27.3	29.4	31.0	31.2	31.1	30.4	26.1	26.3	28.0	28.1	27.5	26.3
Nazareth	SHNAZE11	TMPMAX	2014	28.1	29.5	29.8	30.7	31.1	31.6	28.3	26.7	27.3	26.9	27.5	26.2
Nazareth	SHNAZE11	TMPMAX	2015	27.0	30.5	31.3	31.5	30.7	30.5	29.5	27.9	28.9	29.9		
Nazareth	SHNAZE11	TMPMAX	2016	28.1	29.4	32.8	30.3	29.7	29.6	27.0	27.1	28.3	29.4	27.9	26.6
Nazareth	SHNAZE11	TMPMAX	2017	27.9	28.8	31.5	31.3	29.8	31.6	27.5	26.8	27.7	28.6	27.4	26.0
Nazareth	SHNAZE11	TMPMAX	2018	26.8	29.6	30.0	29.8	29.9	28.8	27.2	27.2	28.8	29.3	28.1	27.3
Nazareth	SHNAZE11	TMPMAX	2019	28.6	30.6	31.8	31.2	31.5	29.9	27.4	26.9	27.2	26.9	27.3	25.3
Nazareth	SHNAZE11	TMPMAX	2020	26.5	28.8	31.5	30.6	31.1	29.3	26.3	26.7	27.9	28.9	27.6	26.8
Nazareth	SHNAZE11	TMPMAX	2021	27.2	28.3	30.7	31.4	30.1	31.7	26.0	27.7	27.7	28.1	27.2	27.1
Nazareth	SHNAZE11	TMPMAX	2022	27.6	29.0	30.2	31.9	33.6	31.2	26.0	27.1	27.3	27.7	27.4	

MPPT Code Based on Incremental Conductance Algorithm with its Flow Chart

```
function Iref = MPPT(V, I, deltaD)

Iref_init = 0.1;
Imin = 0;
I_max = 300; % maximum inverter current

persistent Vold Pold Iref_old;

if isempty(Vold)
    Vold=0;
    Pold=0;
    Iref_old = Iref_init;
end
P= V*I;
dV= V-Vold;
dP= P-Pold;
Iref = Iref_old;

if dP~= 0 && V>400
    if dP < 0
        if dV < 0
            Iref = Iref_old - deltaD;
        else
            Iref = Iref_old + deltaD;
        end
    else
        if dV < 0
            Iref = Iref_old + deltaD;
        else
            Iref = Iref_old - deltaD;
        end
    end
end
% to limit the current in between minimum and maximum
if Iref >=I_max
    Iref = I_max;
end
if Iref < Imin
    Iref = Imin;
end

Iref_old = Iref;
Vold = V;
Pold = P;
```

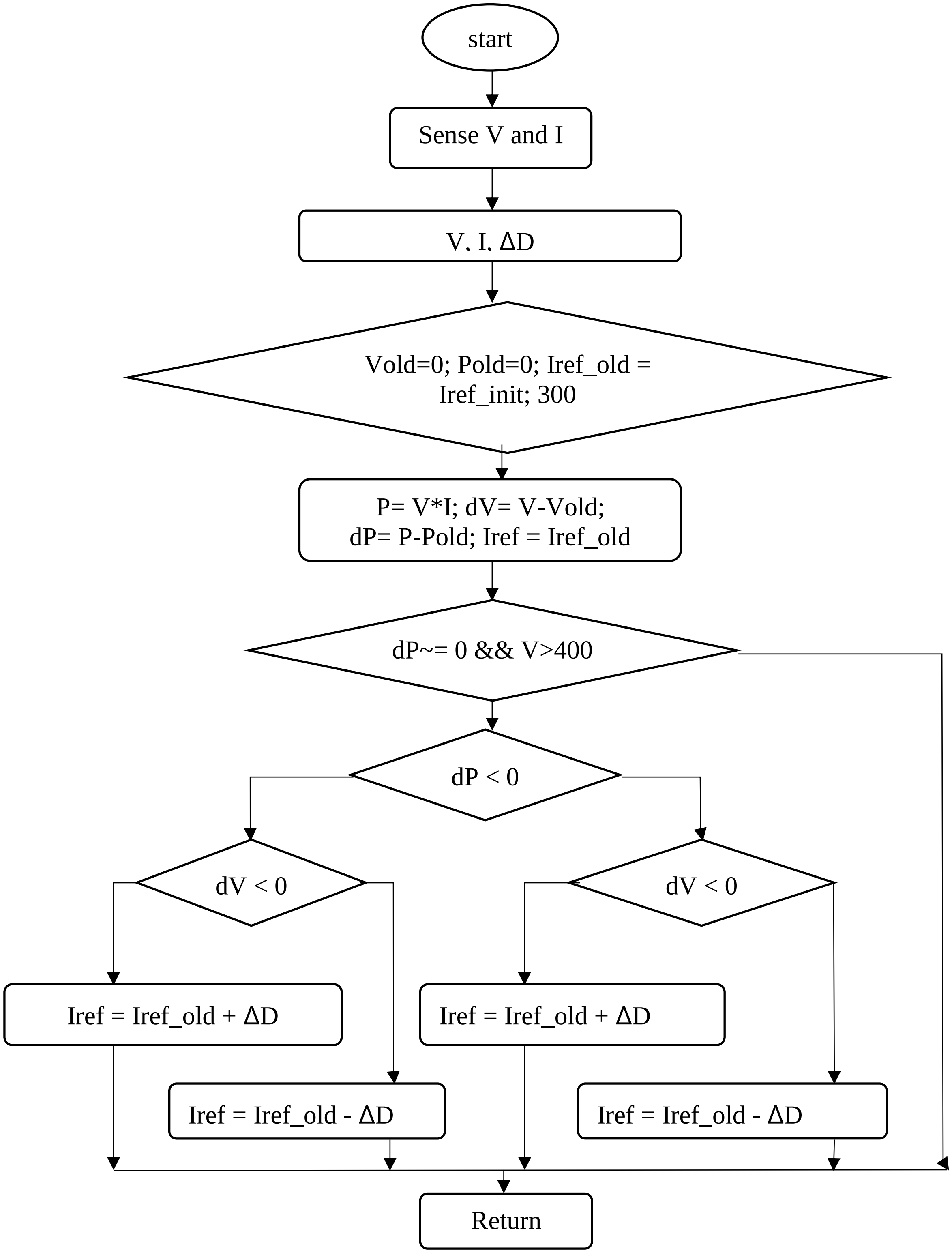
start
Sense V and I
V. I. ΔD
Vold=0; Pold=0; Iref_old = Iref_init; 300
P= V*I; dV= V-Vold;
dP= P-Pold; Iref = Iref_old
dP~= 0 && V>400
dP < 0
dV < 0
dV < 0
Iref = Iref_old + ΔD
Iref = Iref_old + ΔD
Iref = Iref_old - ΔD
Iref = Iref_old - ΔD
Return